Université de Montréal

From coordination complexes to coordination polymers

par

Viviane A. Richter

Département de chimie
Faculté des arts et des sciences

Mémoire présenté à la Faculté des études supérieures
en vue de l'obtention du grade de M. Sc. en chimie

Avril, 2008

Université de Montréal
Faculté des études supérieures

Ce mémoire intitulé

From coordination complexes to coordination polymers

présenté par :

Viviane A. Richter

a été évalué par un jury composé des personnes suivantes :

Prof. Dr. André L. Beauchamp
président-rapporteur

Prof. Dr. Frank Schaper
directeur de recherche

Prof. Dr. Garry S. Hanan
codirecteur

Prof. Dr. Davit Zargarian
membre du jury

RÉSUMÉ

Dans le premier chapitre de ce travail la synthèse d'un nouveau ligand carbene et de ses complexes homoléptique et heteroléptique est examinée. Les composés ont été caractérisé par RMN ^{1}H- et ^{13}C, spectroscopie de masse et l'analyse élémentaire. Le ligand et les deux complexes ont été analysés par électrochimie et photophysique, et leurs propriétés sont discutées. De plus, les structures cristallines du ligand, d'un dimère formé par celui-ci et du complexe homoleptique ont été obtenues et discutées.

Le deuxième chapitre porte sur les propriétés magnétiques des complexes de coordination de Fe(II) et ils sont comparées avec les polymères de Fe(II) correspondant. On a vérifié que les complexes mono-métalliques correspondants montrent les mêmes propriétés magnétiques et structurelles que le polymère de Fe(II). Plus précisément, les complexes mono-métalliques présentent la même structure et ceci explique la transition de spin observée pour le polymère et les complexes mono-métalliques correspondants.

Le dernier chapitre traite de la synthèse d'un nouveau ligand *N*-oxyde soluble dans l'eau, formé à partir du ligand tpy-ph-tpy. On a analysé ce ligand par RMN ^{1}H, spectroscopie de masse ainsi que par analyse élémentaire. En plus du

nouveau ligand *N*-oxyde, un nouveau complexe platine polypyridine a été synthétisé et analysé. Le point important ici est lque par fort échauffement, le complexe change de couleur en passant du jaune brillant à rouge profond.

MOTS CLES

Complexes des métaux de transition, propriétés photophysiques, structure cristaline, magnétisme moléculaire, analyse structurale, polymères de coordination

ABSTRACT

In the first chapter of this work the synthesis of a new ligand, containing a six-membered heterocyclic carbene ring, and its homoleptic and heteroleptic Ru(II) complexes are examined. The compounds have been analyzed by ^{1}H and ^{13}C NMR, mass spectrometry and elemental analysis. The ligand and the two complexes have been analyzed electrochemically and photophysically and their properties are discussed. In addition to that, crystal structures of the ligand, a dimer formed by it and the homoleptic complex have been obtained and are discussed.

The second chapter deals with the magnetic properties of a Fe(II) coordination polymer and its corresponding mono-metallic complexes. It is examined if they show the same magnetic and structural properties as the already known Fe(II) coordination polymer. In effect, the mono-metallic complexes do show similar structural behavior and it could be figured that this is the reason for the spin-transition observed for the Fe(II) coordination polymer and the corresponding mono-metallic complexes.

The last chapter deals with the synthesis of a new water soluble *N*-oxide ligand formed from the tpy-ph-tpy ligand. It has been analyzed by ^{1}H NMR, mass

spectrometry and elemental analysis.

In addition to the new *N*-oxide ligand, a new platinum polypyridine complex was synthesized. It also was analyzed by ^{1}H NMR, mass spectrometry and elemental analysis. Interesting here is, that this complex changes its color from bright yellow to deep red upon heating.

KEYWORDS

Transition metal complexes, photophysical properties, crystal structures, molecular magnetism, structural analysis, coordination polymers

Table of Contents

Index of Tables

Index of Figures

Index of Schemes

Abbreviations

^{1}LMCT	Singlet ligand-to-metal charge transfer state
^{1}MLCT / ^{3}MLCT	Singlet metal-to-ligand charge transfer / triplet metal-to-ligand charge transfer state
^{3}MC	Triplet metal centered state
AUC	Analytical ultra centrifuge
BESSY	Berliner Elektronenspeicherring-Gesellschaft für Synchrotronstrahlung
Br-ph-tpy	4'-(4-Bromophenyl)-2,2':6'2"-terpyridine
CP	Coordination polymer
CT	Charge transfer
DCP	Dynamic coordination polymer
DHP	Dihexadecyl phosphate
DMSO	Dimethyl sulfoxide
DSC	Differential scanning calorimetry
EDR	Energy dispersive reflectometer
ELSA	Electrostatic layer-by-layer self-assembly
Et_3N	Triethylamine
FWHM	Full width at half maximum
GS	Ground state
HS	High spin
ISC	Inter system crossing
LS	Low spin
m-cpba	3-chloroperoxybenzoic acid
MAC	Mononuclear amphiphile complex

MEPE	Metallo-supramolecular polyelectrolyte
PAC	Polyelectrolyte amphiphile complex
ph-tpy	4'-phenyl-2,2':6', 2"-terpyridine
py-tpy	4'-pyridyl-2,2':6'2"-terpyridine
r.t.	Room temperature
SAXS	Small angle X-ray scattering
Squid	Superconducting quantum interference device
SFM	Tapping-mode scanning force microscopy
$t_{2g}e_g$	d-orbitals of a transition metal ion in octahedral coordination
TGA	Thermo Gravimetric Analysis
tpy	2,2':6'2"-terpyridine
tpy-opropo-tpy	1,3-Bis[4'-oxa (2,2':6',2"-terpyridinyl)]propane
tpy-ph-tpy	1,4-bis(2,2":6',2"-terpyridine-4'-yl)benzene

To my children,

Felix, Lucas & Casimir

and my husband,

Stephan.

Acknowledgments

I thank Garry S. Hanan and Frank Hein Schaper for the possibility to carry out my M.Sc. thesis in their groups. I also want to thank Hein for his support, especially during writing up, and all the helpful discussions we had.

I also want to thank Dirk G. Kurth for the opportunity to pursue the second half of my thesis in his group at the MPIKG at Potsdam.

Prof. Dr. Moehwald from the MPIKG was always there to discuss my results and he helped me to get a deeper insight into sciences.

I also want to thank Francine Bélanger, from the Université de Montréal, for helping me with my crystal structures and all her moral support.

Guntram, my officemate, who helped me with the structural analysis and the magnetic measurements, was a big help either; he was always there with a good advice.

And first of all, I would like to thank my family, my husband Stephan and my children Felix, Lucas and Casimir, for all their patience. They made this work possible.

1 Introduction

"Logic is the cement of our civilization with which we ascend from chaos using reason as our guide."

T'Plana-Hath

The miniaturization of electrical and optical circuits is currently pursued by the top-down approach, which is mainly the domain of engineers and physicists. However, using this approach to obtain components that are progressively smaller and smaller in size is limited by physical parameters and, on the other hand, the production costs. So the idea of the molecular machine was born, in other words, the bottom-up approach, which consists of the use of single molecules to build-up nanosized components. But even though the idea of the molecular machine is a very tempting one, such systems are far too complex to be obtained by means of well-established synthetic methods. This might be one of the reasons why the concept of self-assembly has become of enormous interest over the last decades. It also means that the intelligent design of the different components that self-assemble by weak interactions to form a desired system is the most promising way leading to molecular machines. Self-assembly is generally agreed to be the aggregation of molecules driven by non-

covalent interactions. There are several different inter- and intramolecular interactions covering forces ranging from 1-120 kJ/mol with van der Waals forces at the weak end and coordinative bonds at the strong end of the scale. Comparing the strengths of the different interactions, the dative bond can be considered to lie in the middle between weak non-covalent interactions and covalent bonding. But in addition to being the strongest one of the non-covalent interactions, the coordinative bond possesses another particularity: it is highly directional. This kind of directionality is a component, which is needed for the assembly of hierarchical structures. This entire process evolves through multi-step self-assembly with interactions at several levels and length scales including metal ion coordination, electrostatics, and van der Waals forces. In addition to that, the incorporation of metal ions into a polymeric system is a way to exploit the metal ions' rich properties, such as their magnetic [1, 2], electric [3, 4] and optical [5-7] properties.

The possibility to modify those polymer properties – as well as its morphology – willingly by the choice of the involved metal ions and the manipulation of, for example, its redox properties opens pathways to a completely new class of functional materials [8].

As most of the knowledge concerning the properties that are exploited by metal ion coordination polymers are based on experiences from the broad field of coordination chemistry, a chapter dealing with some of the rich properties of self-assembling coordination complexes in view of their influence on the chemistry of coordination polymers will be part of this chapter. We will then discuss to what extent the knowledge gained about coordination complexes can be carried forward to coordination polymers.

1.1 Coordination Complexes – The Precursors of Coordination Polymers

All the interesting optical, electric and magnetic properties of coordination complexes can be incorporated into coordination polymers as well. One straightforward strategy for designing coordination polymers with specific properties is therefore the study of the appropriate monomeric coordination complex and – if it shows the desired properties – its incorporation into a coordination polymer. Once incorporated, these coordination complexes can be part of the polymers backbone or also pending to it (Figure 1).

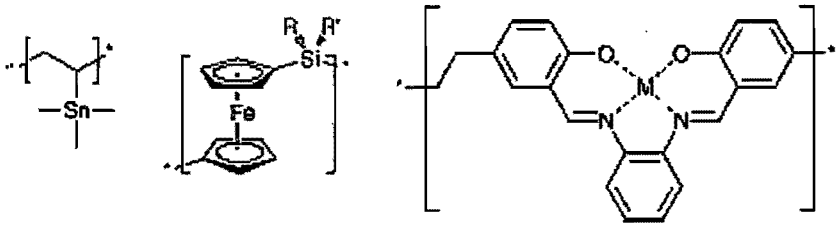

Figure 1. Metals can be pendant to (left) or they can be present (center) in the polymer backbone or the metal is embedded in a polymeric chelate (right). In the coordination polymer (center) the coordinative bond is an integral part of the polymer backbone [8].

Of course, the different positions of the coordination complex in the polymer will result in different outcomes. Incorporation into the polymer backbone with sufficiently short spacer units in between the metal centers will for example allow for an electronic coupling of the metal centers resulting in a vast variety of interesting new properties while a coordination complex pending to the polymer backbone will have a much milder influence on the properties of the whole polymeric system as, for example, simply changing the color of the compound, and therefore its wavelength of absorption, while leaving its other properties, such as its mechanical properties unchanged. In general, we will consider only those coordination polymers in which the coordination complex is an integral part of the polymer backbone. This means however, that the

choice of the metal will have an enormous impact on the new coordination polymers' properties. Therefore, it is important to have a pool of information available for the compound in question and this is the huge advantage of using coordination complexes: the enormous amount of information gathered about them during the last century. There are binding constants available for all sorts of different metal ions and ligands that can be used for calculating equilibrium positions of dynamic polymeric systems [9]; the optical properties of polypyridyl coordination compounds are already intensely studied and could now be used to obtain CP's suitable for light harvesting, which is an important issue nowadays due to the depletion of fossil fuel sources. On the other hand, coordination polymers can be used as a sort of carrier package, meaning that a coordination polymer can be deliberately switched from its polymeric to its monomeric state by an external stimulus, the monomeric state having specific properties as, e.g., significant catalytic properties.

1.2 Transfer of Properties from Coordination Complexes to Coordination Polymers

1.2.1 Photophysical Properties

The very appealing photophysical properties of polypyridyl coordination complexes are an illustrative example of how to incorporate a coordination complex's properties into a polymer. Polypyridyl coordination complexes usually absorb in the UV-vis region of the electromagnetic spectrum by means of their singlet metal to ligand (or ligand to metal) charge transfer (^{1}MLCT / ^{1}LMCT) state. They can then undergo an intersystem crossing (ISC) into their relatively long-lived triplet CT state from which the major deactivation pathways are either emission to the ground state (GS) or thermal access to the triplet metal centered state (^{3}MC) which deactivates primarily via non-radiative decay (Figure 2) [10].

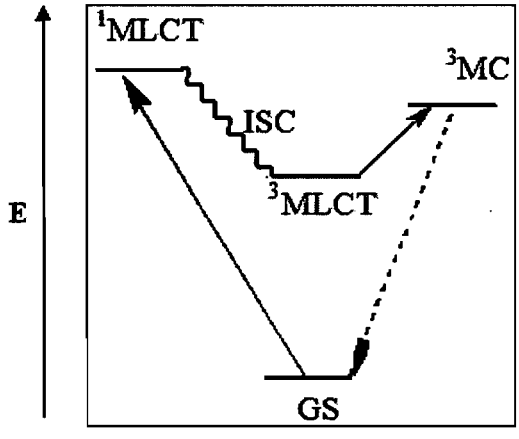

Figure 2. Simplified state level diagram of a Ru(II)terpyridine complex.

The energy of these states can be tuned by varying the polypyridyl ligands by means of electrondonating or -withdrawing substituents. With the help of a suitable polytopic ligand, a complex so obtained can be incorporated into a coordination polymer. An exemplary case is the Fe(II) coordination polymer used by our group (Figure 3). The $[Fe(tpy)_2]^{2+}$ complex is a well studied compound: values like terpyridine binding constants with this metal ion as well as electrochemical and photophysical properties are easily accessible from literature sources. As suitable polytopic ligand, the tpy-ph-tpy ligand shown by Figure 3 was used in this case.

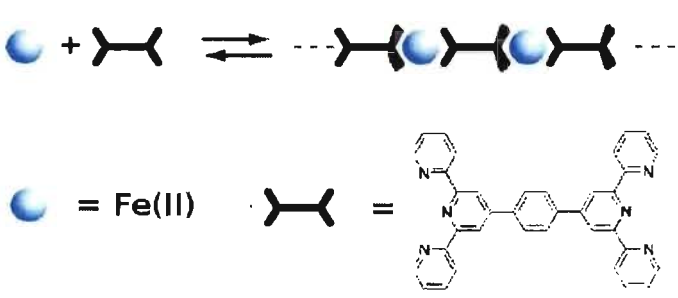

Figure 3. Self-assembly of a coordination polymer from a polytopic ligand and Fe(II) metal-ions.

The UV-Vis spectra in Figure 4 show how the photophysical properties of the parent compound and the final coordination polymer are related [11].

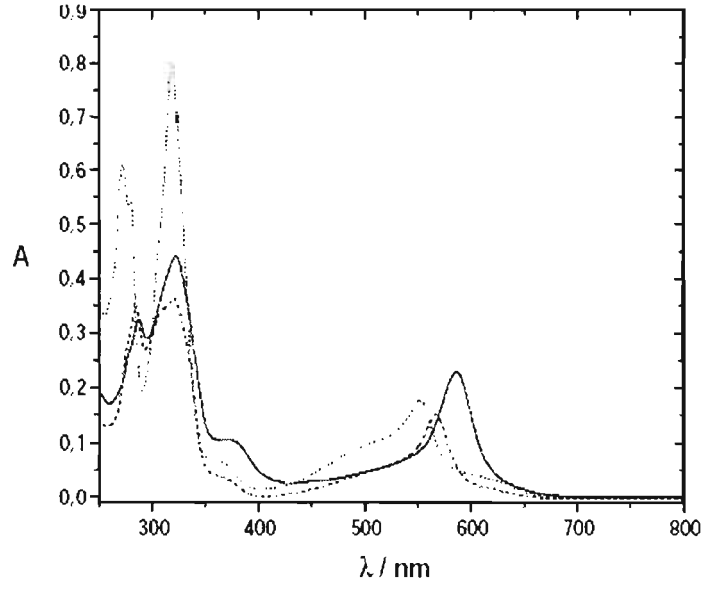

Figure 4. UV/VIS-Absorption spectra of Fe(II)-terpyridine complexes in methanol. Line: CP-Fe tpy-ph-tpy, Dashes: $[Fe(me\text{-}ph\text{-}tpy)_2]^{2+}$, Dots: $[Fe(tpy)_2]^{2+}$. Reproduced from Ref.[11].

The absorption maxima for the ligand centered absorptions in the UV part stay in the same range for all three compounds, while a slight redshift is observed from $[Fe(tpy)_2]^{2+}$ to $[Fe(me\text{-}ph\text{-}tpy)_2]^{2+}$ and the Fe(II) coordination polymer CP-Fe tpy-ph-tpy. This is as expected and is due to the progressively more extended π-system that leads to the lower energies of the absorbing states.

1.2.2 Magnetic Properties

The presence of semi-occupied d-orbitals in transition metal complexes gives rise to several interesting phenomena including strong absorption, high quantum yields, suitable excited state lifetimes luminescence, tunable redox states and last but not least, spin cross-over [12]. The spin crossover phenomenon is typically observed for transition metal compounds having a $3d^n$ ($4 \leq n \geq 7$) electron configuration, with iron(II) being the most widely studied metal ion [13]. Iron(II)complexes in an octahedral ligand field can thus adopt the low spin $1A_{1g}$ conformation as well as the high spin $^5T_{2g}$ conformation. The low spin compounds can undergo a thermal spin crossover from low spin to high spin (Figure 5), resulting in a number of possible applications like, e.g., as contrast agents for biomedical imaging, temperature threshold indicators or as

optical elements in spin display devices.

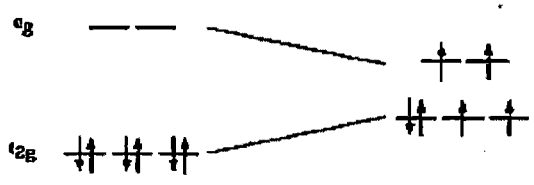

Figure 5. Low spin (left) and high spin (right) arrangement in the iron (II) metal ion.

There are several approaches to control the spin state of coordinated metal ions, one of which is the manipulation of the steric bulk or strain of the ligand system. It is known that the 2,2':6',2" terpyridine induces a strong ligand field and as a result, $[Fe(II)(tpy)_2]\ X_2$ complexes are generally low spin [14]. However, it has recently been suggested that bulky substituents in the 6- and 6"-position of the tpy-ligand influence the spin state by distorting the octahedral coordination sphere and, therefore resulting in a change of the field splitting [12].

Since for any metal ion in an octahedral field there is a 'cross-over' point at which the change from low spin to high spin occurs, careful control of the ligand-field splitting parameter Δ would allow the choice of a ligand with a ligand field strength close to this cross-over point to obtain an equilibrium

between the two spin states. If now the energy separation Δ between the t_{2g} and e_g orbital sets is of the order of kT, there will be a pronounced effect of the temperature on the position of this equilibrium.

The Fe(II) systems are of particular interest, since the low spin state is diamagnetic and the change in the number of unpaired electrons when going to high spin is four. This also means, that the change in the magnetic moment of the complex will be a relatively pronounced one, thus allowing easy detection of the cross-over point and the determination of the field splitting parameter Δ.

A remarkable example for this kind of system is the spin cross-over induced by an amphiphilic phase transition introduced by Kurth and co-workers in 2005 [12]. Here the concepts used in the design of Fe(II) coordination complexes featuring a spin transition are carried forward to a coordination polymer. However, in this case the steric strain is not induced by bulky substituents as they would hinder the formation of high molecular weight chains by their steric demands. Instead of introducing bulky substituents onto the ligands, the systems counter ions have been replaced by charged amphiphiles which can then induce a spin cross-over by an amphiphilic phase transition once the system has been applied onto a solid substrate in form of a Langmuir-Blodgett multilayer [12].

The first chapter of this thesis will deal with the manipulation of the properties of carbene-transition metal complexes in order to improve their photophysical properties, while the second one is occupied with the reasons for the spin transition of the aforementioned Fe(II)-coordination polymer and the effects of the phase transition of the amphiphiles on the appropriate mono-metallic complexes. Finally, the last chapter will deal with ongoing work on the synthesis of a new Pt-containing species and the possibility to form Pt-polymers with it.

2 Synthesis and Characterization of a Novel Six-membered *N*-heterocyclic Carbene Ligand and its Homoleptic and Heteroleptic Ru(II) Complexes

"As I turned, and my eyes beheld you, *I displayed emotion... I ask forgiveness."*

Surak

2.1 Introduction

During the last four decades, interest in molecules showing unusual binding modes has increased in synthetic inorganic chemistry [15]. Carbenes are neutral compounds with a divalent carbon atom having a free electron pair. As strong σ-donors, they form stable carbon-metal bonds with transition metals [16]. Of special interest are electron-rich carbenes incorporating additional Lewis bases, as they are considered to have Lewis basicity towards metal centers with a strength comparable to phosphines [15]. *N*-heterocyclic carbenes have received increasing attention during the last years, due to the interesting catalytic properties of their transition metal complexes [15]. They have been used in cross-coupling reactions and in polymerization chemistry, a recent paper reporting on *N*-heterocyclic palladium carbene complex as catalyst for Suzuki

coupling reactions at ambient temperature [17, 18].

More recently, attention was drawn onto Ru(II) complexes incorporating carbene-based polypyridine ligands due to their improved photophysical properties as compared to the well-known and extensively studied $[Ru(tpy)_2]^{2+}$ motive [19]. These improved photophysical properties result from the destabilization of the metal centered molecular orbitals by the strong σ-donating ability of the carbenes, which raises the metal-centered states in energy relative to the ^{3}MLCT state of the complex and finally leads to an increase in the excited state lifetime of the metal complex [20, 21].

Another rather recent development is the interest in dynamic polymers based on carbene dimerization equilibria. Due to the dynamic nature of the bond, it is possible by altering the ambient conditions to change the systems properties, such as its chain length. Most important here is the reversibility of the interactions, leading to dynamic systems whose properties depend on the extent of the reversibility. This reversibility could than be a means to control / manipulate features like chain length and geometry, thus allowing for subsequent rearrangement at the molecular level or self-healing abilities [9].

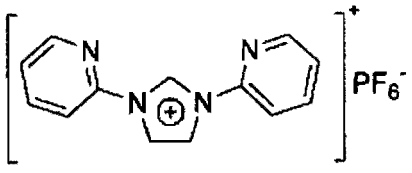

Figure 6. The pyridylcarbene precusor as synthesized by Chen and co-workers (Adapted from Ref. [22]).

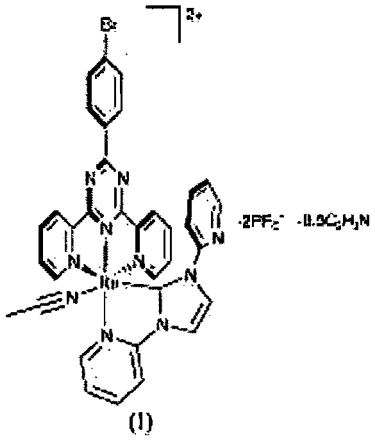

Figure 7. A hybrid bidentate and tridentate ruthenium(II) complex incorporating triazine and polypyridine carbene ligands [23].

The aim here was to synthesize a tridentate carbene ligand as a structural analogue to the well-known terpyridine ligand for complexation to Ru(II). This was meant to improve the photophysical properties of the resulting complexes by the destabilization of the metal-centered ^{3}MC states, and this due to the strong σ-donating abilities of the carbene ligand. As it is already known, this destabilization, e.g. raise in energy, of the metal-centered states should cut of one of the major deactivation pathways, namely the thermal access to the ^{3}MC state from the ^{3}MLCT, which deactivates via non-radiative decay and, therefore, should lead to a long-lived ^{3}MLCT excited state [24]. There are already some examples of heterocyclic carbenes forming complexes with ruthenium and other

transition metals, some of them showing very promising photophysical properties [19, 22].

The 1,3-bis(2-pyridyl)imidazol-2-ylidene (pyimypy) ligand (Figure 6), synthesized by Chen and co-workers [22], was used by members of our group in order to synthesize a carbene containing ruthenium(II) complex. Unfortunately, this ligand does not coordinate in a tridentate fashion to Ru(II): one pyridine ring flips off; a solvent molecule is coordinated instead as sixth ligand. This is due to the ring strain in the five-membered carbene ring and the resulting unsuitable bite angle for tridentate terpyridine-like coordination (Figure 7) [23].

To obtain a tridentate carbene analogue of the well-known terpyridine ligand, a six-membered carbene-precursor with two pyridine substituents has been synthesized. In the following, the synthesis of the homoleptic as well as a heteroleptic Ru(II) complex of the corresponding carbene-ligand was envisioned.

2.2 *Results and Discussion*

The carbene-precursor **1** was obtained by refluxing 1,4,5,6-tetrahydro-pyrimidine in an excess 1-bromopyridine for 48 h. It was then isolated by filtration after precipitation as its PF_6-salt from a saturated methanolic NH_4PF_6 solution (Scheme 1).

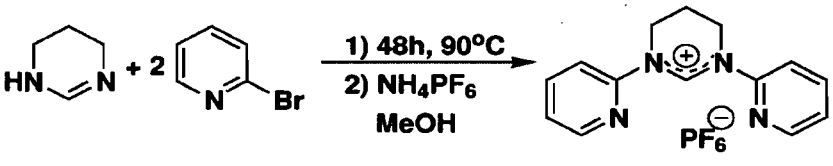

Scheme 1. Preparation of the protonated carbene precursor ($[\mathbf{1H^+}][\mathbf{PF_6}]$).

The ligand is probably formed by an aromatic nucleophilic reaction mechanism, involving an intermediate Meisenheimer-complex (Scheme 2) [25].

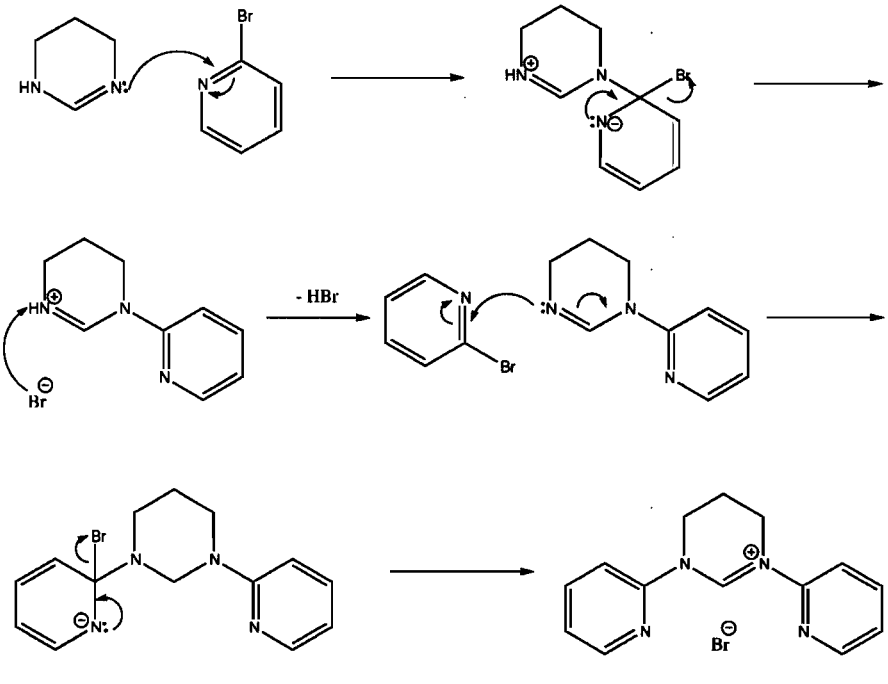

Scheme 2. Proposed reaction mechanism for the formation of $[\mathbf{1H^+}][\mathbf{PF_6}]$.

The ^{13}C NMR spectrum of the product does not show the peak for the carbene-precursor center carbon at a standard relaxation delay of one or two seconds. However, after several attempts with successively longer relaxation delays, the peak could finally be observed using a relaxation delay of 8 seconds, and this at a chemical shift of 152 ppm which is in the same range as other examples reported in literature [26, 27].

The crystal structure in Figure 8 shows how the two pyridine rings together with the carbene precursors N2 – C14 – N3 are essentially co-planar, showing the partial aromaticity of this part of the molecule, while the C6-C7-C8 part of the central non-aromatic ring is bent by 129°.

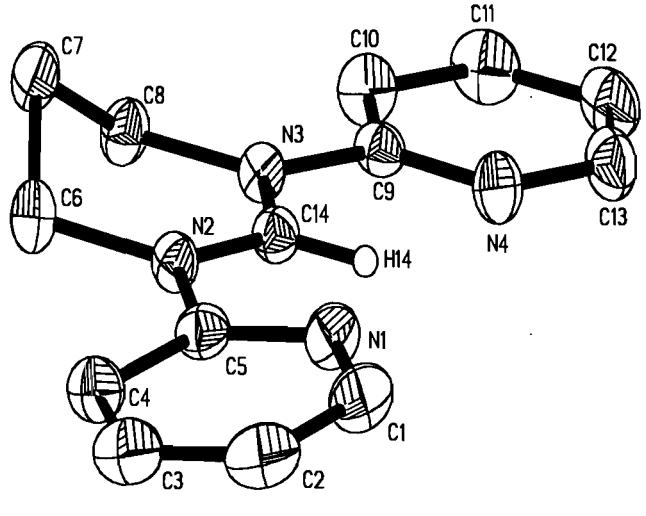

Figure 8. Crystal structure of the protonated ligand precursor **[1H$^+$][PF$_6^-$]**. Thermal ellipsoids are drawn at the 50% probability level. Hydrogen atoms, with the exception of H14, and the anion were omitted for clarity. N3-C14 1.3193(2) Å, N2-C14 1.3172(2) Å.

Extensive hydrogen bonding between H14 and the anion PF_6^- is observed, probably due to the acidic nature of this proton.

For the synthesis of homo- and heteroleptic Ru(II) complexes with our carbene ligand, we aimed for the generation of the free carbene to facilitate the ligand's complexation to the metal. Unfortunately, attempts to obtain the free carbene by deprotonation failed. Even though several different bases under various conditions were used, the free carbene could not be isolated.

Mass spectra of the reaction mixtures obtained in deprotonation attempts frequently contained species of a molecular weight higher than the postulated carbene, which might indicate coordination of the formed carbene ligand to the alkali metal cation of the base employed. Similar coordination of carbenes to alkali cations have been described by Alder et al. [28]. ^{1}H NMR data of an isolated sample seemed to support this theory, as the peaks in the aliphatic region, which should be most affected by a complexation of the carbene center, were largely broadened as would be expected for an equilibrium between the complexed species and the free carbene (Figure 9).

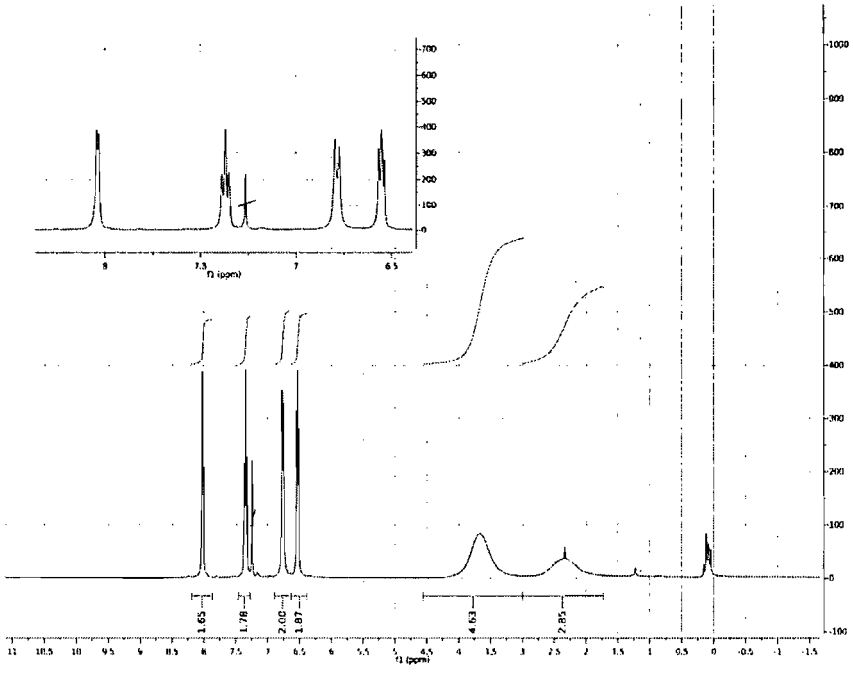

Figure 9. ^{1}H NMR spectrum of the possible equilibrium between the carbene and either its dimer or its potassium complex.

A single crystal obtained from the reaction mixtures of the deprotonation experiments, however, showed the formation of a dimerized carbene ligand $\mathbf{1}_2$ (Figure 10 and Scheme 3) despite the steric hinderance of the four pyridine rings at the N atoms next to the carbene center. The C-C double bond of $\mathbf{1}_2$ of 1.350(3) Å is comparable to those of other tetraamino ethenes (1.31-1.46 Å, based on 12 structures in the Cambridge Structural Database) and does not indicate any effect of the four pyridine substituents on the strength of the double

bond.

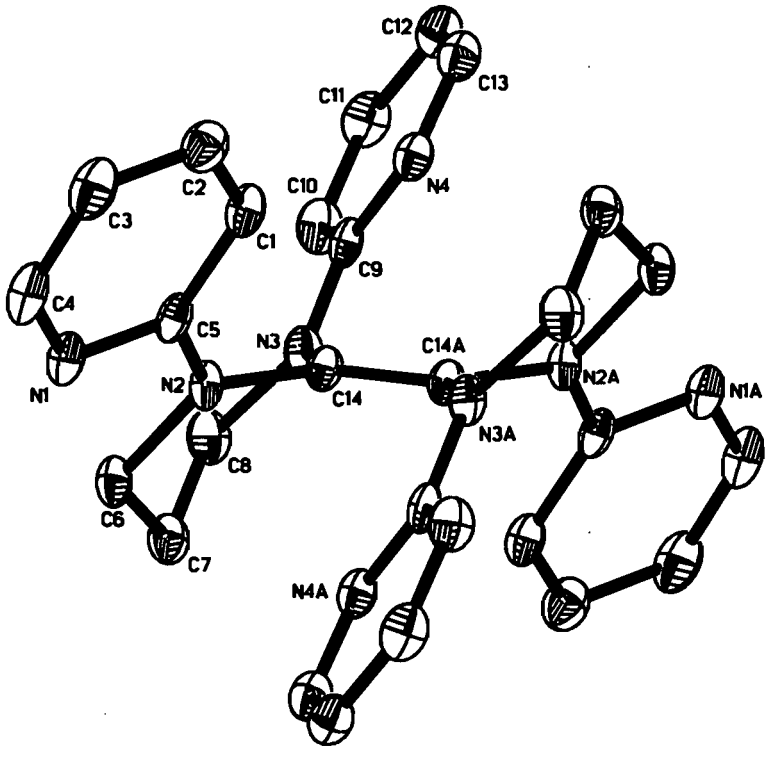

Figure 10. Crystal Structure of the dimerized carbene ligand $\mathbf{1}_2$. Thermal ellipsoids are drawn at the 50% probability level. Hydrogen atoms were omitted for clarity. C14-C14A 1.350(3) Å, N3-C14 1.421(2) Å, N2-C14 1.414(2) Å.

The obtained crystal structure of the dimer $\mathbf{1}_2$ also explains the broadening of the aliphatic peaks in the NMR spectrum (Figure 9). While ring inversion is fast in the protonated precursor, it is significantly slower for the dimerized species yielding broadened peaks. This can be rationalized with the positioning of the

pyridine rings. The protonated precursor **[1H$^+$][PF$_6$]** has an envelope conformation with the pyridine rings located in the N-C14-N plane. They thus do not change their position during a ring inversion of the aliphatic backbone (see Figure 8). The dimeric species **1$_2$**, however, shows a boat conformation of the six-membered ring. Ring inversion requires moving the pyridine substituents from above the N-C14-N plane to below the plane. Due to the steric interactions of the pyridine rings on each side of the double bond, ring inversion has thus to occur simultaneously in both six-membered rings of **1$_2$**.

To investigate the dimerization reaction in slightly more detail, **[1H$^+$][PF$_6$]** was deprotonated with NaH in C_6D_6 (Scheme 3) and the supernatant solution investigated by NMR. The ^{1}H spectra contained several new peaks.

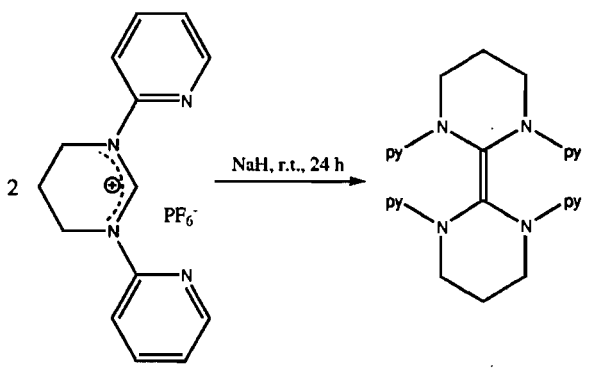

Scheme 3. Attempt to prepare the free carbene, leading to the formation of its dimer (**1$_2$**).

The absence of the signal of the C_{NHC}-H proton (observed at 9.07 ppm) and the higher signal intensities ($[\mathbf{1H^+}][\mathbf{PF_6}]$ is barely soluble in C_6D_6) excluded the presence of the carbene precursor in solution. The presence of impurities and solvents preclude an unambiguous assignment of the peaks in the aliphatic backbone, but broadened peaks as observed for $\mathbf{1}_2$ were absent. I thus propose, that the species prepared *in situ* in C_6D_6 is indeed the free carbene, which seems to dimerize during the concentration of the solution upon isolation. If the free carbene could be obtained *in situ* in low concentrations, then direct complexation to ruthenium during the deprotonation might prevent the dimerization reaction. Indeed, when $RuCl_3$ was refluxed with $[\mathbf{1H^+}][\mathbf{PF_6}]$ in the presence of Et_3N, the homoleptic ruthenium bis-carbene complex **2** was obtained as its PF_6^- salt (Scheme 4).

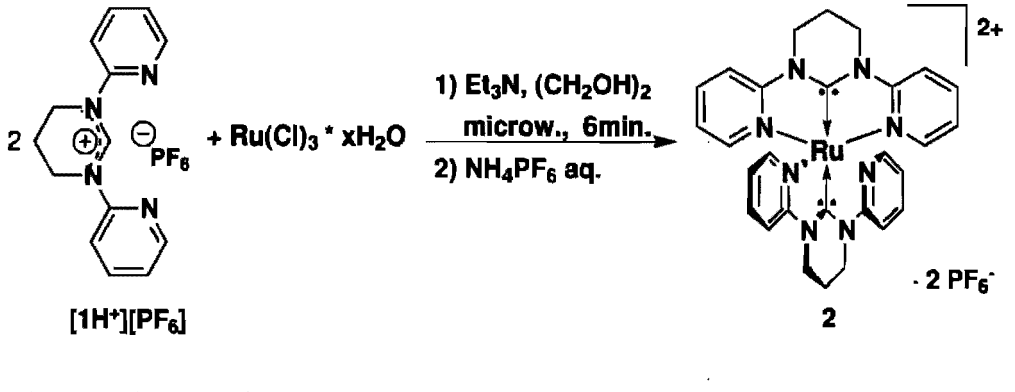

Scheme 4. Preparation of the homoleptic carbene complex **2**.

The synthesis was carried out in the microwave and the Ru(carbene)$_2$ complex **2** obtained by refluxing 0.5 eq. $RuCl_3$ with 0.9 eq. Et_3N and 1 eq. of **[1H$^+$][PF$_6$]** in ethylene glycol (Scheme 4). Complex **2** was then precipitated as its PF_6^- salt from an aqueous NH_4PF_6 solution. Figure 11 shows the crystal structure of the homoleptic carbene complex **2**.

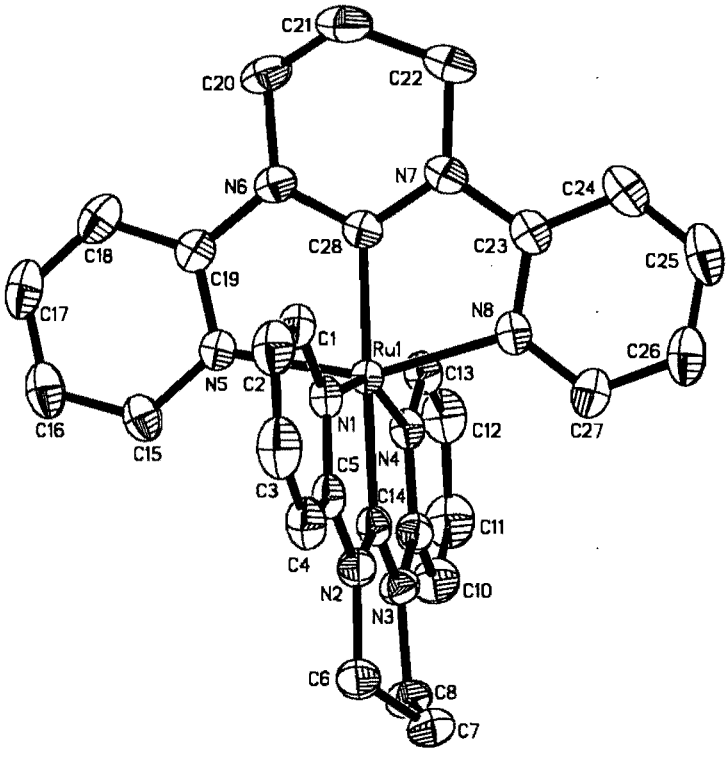

Figure 11. Crystal structure of the homoleptic complex **2**. Hydrogen atoms and PF_6^- anions were omitted for clarity. Thermal ellipsoids are drawn at the 50% probability level. Ru1 – N1 2.0841(2) Å, Ru1 – C14 1.972(3) Å, Ru1 – N4 2.0927(2) Å, Ru1 – N5 2.0913(2) Å, Ru1 – C28 1.969(2) Å and Ru1 – N8 2.0876(2) Å.

The bite angle of the ligand and the Ru-ligand bonds in complex **2** are in the same range as for the already known tpy-complexes [10, 29]. This means that the octahedral coordination environment for the ruthenium stayed approximately the same as in the known tpy-complexes, while still introducing the electronic properties of a strong σ-donor into the complex.

The synthesis of heteroleptic **[Ru(Br-ph-tpy)(1)]**$^{2+}$ complex (**3**)(Figure 12) proved to be more difficult than expected, due to the strong nature of the Ru-carbene bond.

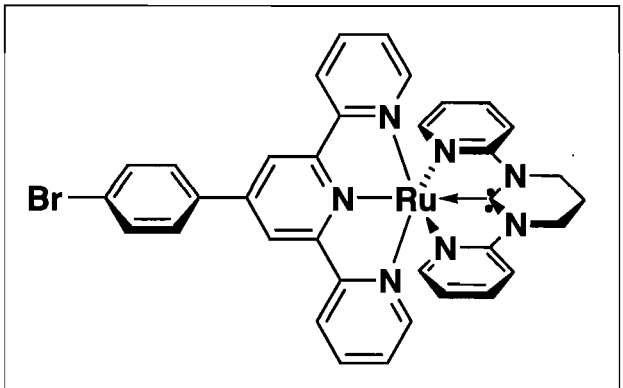

Figure 12. Heteroleptic carbene complex **3** (counter-ions are omitted).

The synthesis in the microwave with or without base always gave an inseparable mixture of **2**, **3** and the terpyridine homoleptic complex, together with several unidentified side products. Complex **3** was finally obtained in a mixture of **2**, **3**

and the terpyridine homoleptic complex by refluxing 1eq. $Ru(Br\text{-}ph\text{-}tpy)Cl_3$ with 1 eq. $[\mathbf{1H^+}][\mathbf{PF_6^-}]$ in ethylene glycol in the presence of 0.9 eq. of Et_3N. The mixture of the obtained complexes was precipitated as their PF_6^- salts from an aqueous NH_4PF_6 solution. The compounds in this mixture were then separated by column chromatography to give complex **3** (Scheme 5).

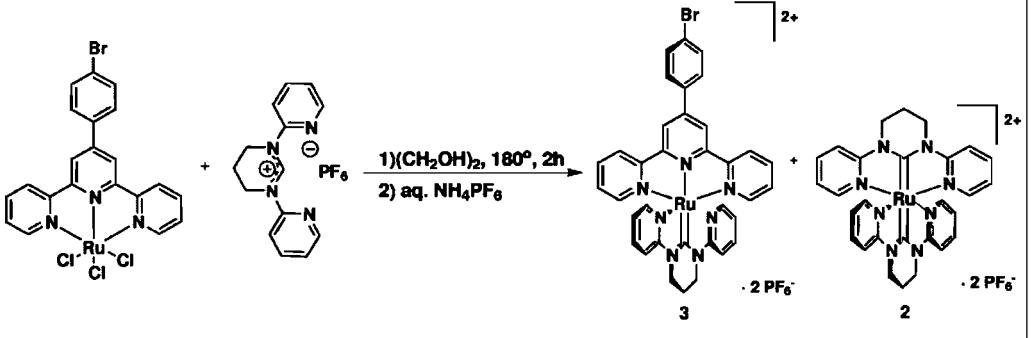

Scheme 5. Preparation of complex **3**.

The temperature during synthesis needs to be above 120 °C in order to allow for the Ru-carbene bond to form. However, above ~ 110 °C, the Ru-tpy bond starts to scramble, which -together with the high stability of the Ru-carbene bond- leads to an increased amount of the homoleptic $Ru(carbene)_2$ complex. Optimizing experimental conditions lead to the maximum yield of 52 % for complex **3**, but was always accompanied by at least 16 % of **2**.

2.2.1 Properties

2.2.1.1 Electrochemistry

The strong σ-donating ability of the carbene ligand is expected to raise the metal-centered states relative to the MLCT orbitals in energy [23]. Complex **2** really shows an increase in the energy of the metal centered orbitals and becomes easier to oxidize as compared to the parent compound $[Ru(tpy)_2]^{2+}$ (Table I). However, as electrochemical results indicate, there is rather an increase in the energy of the metal-centered states for complex **3**, shifting $E_{1/2}$ from 1.25 V for $Ru(tpy)_2^{2+}$ to 1.334 V for **3**. This is probably due to the electron deficient terpyridine ligand that can oppose a certain amount of the σ-donation from the carbene ligand and decrease the electron density at the metal.

Table I. Half-wave potentials for ligand **[1H$^+$][PF$_6^-$]** and Ru(II) complexes **2** and **3** in a comparison with $[Ru(tpy)_2]^{2+}$ a)

compound	$E_{1/2}$(oxidation)	$E_{1/2}$(reduction)
[1H$^+$][PF$_6^-$]	/	-1.20, (48) -0.14 (irr.)
2	1.17, (52)	-0.97 (irr.)[b]
3	1.33, (44)	-0.73 (irr.)[b]
$Ru(tpy)_2^{2+}$	1.25[c]	-1.36[c]

a) Potentials are in volts vs SCE for acetonitrile solutions, 0.1 M in TBAP, recorded at 25 ± 1 C at a sweep rate of 100 mV/s. The difference between cathodic and anodic peak potentials (millivolts) is given in parentheses. b) Irreversible; potential is given for the cathodic wave. c) Reproduced from Ref. [30]

Interestingly, in the case of complex **3**, an extremely high intensity is observed for the ligand reductions. The Ru(II/III) couple is observed at 1.33 V, which is in the normal range for this redox couple. However, the intensity of the ligand reduction peak is significantly increased (Figure 13).

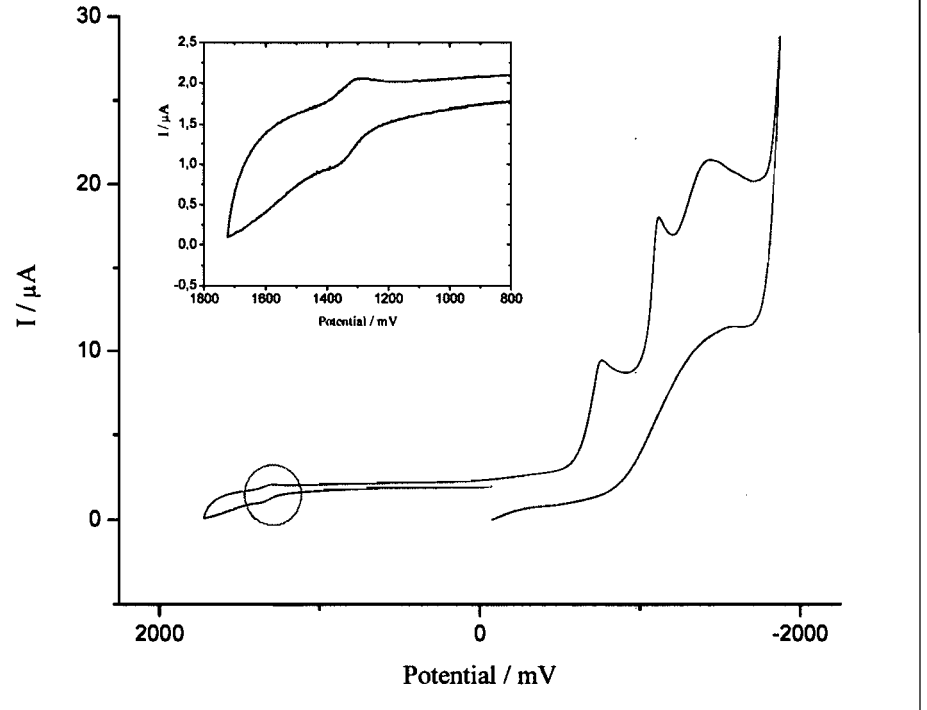

Figure 13. Cyclic voltammogram of **3** in CH_3CN with a platinum electrode at $4 \cdot 10^{-4}$M.

We believe that this is due to an electron transfer from the electron-rich carbene ligand to the rather electron-deficient terpyridine ligand. We suppose that the compound accumulates as shown by Figure 14 [31].

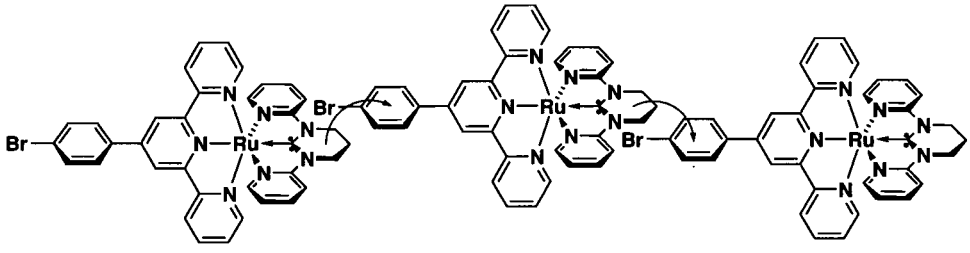

Figure 14. Schematic representation of the possible electron transfer in complex **3** [31].

If this is the case, there could be an electron transfer that induces measurements in not only the first diffusion layer as usually in cyclic voltammetry, but leads to a transfer through several diffusion layers, producing the high intensity seen for the ligand reductions in Figure 11. In this case, the effect should disappear at low concentrations. So additional experiments at different concentrations need to be done to further elucidate this effect.

2.2.1.2 Spectroscopic properties

The absorption spectra of **[1H$^+$][PF$_6^-$]**, **2** and **3** are shown in Figure 15, the absorption data is tabulated in Table II.

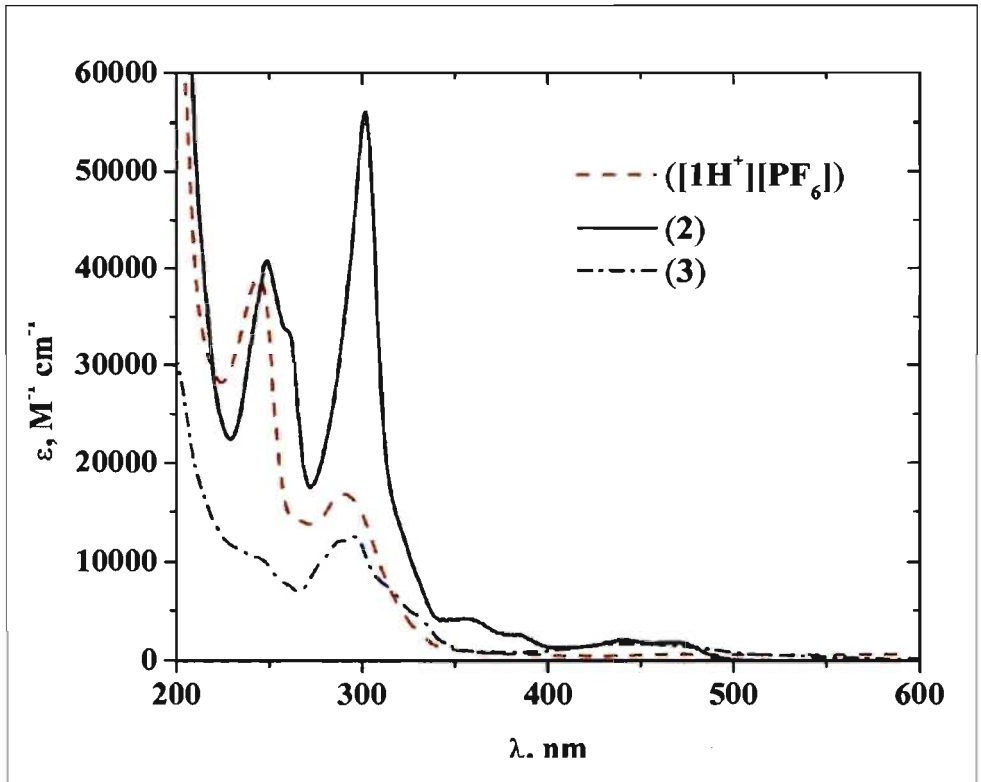

Figure 15. Absorption of **[1H$^+$][PF$_6^-$]**, **2** and **3** in deaerated acetonitrile.

The ligand itself shows a strong π-transition at 244 nm that is probably due to the pyridine rings which are behaving as single pyridines. Even though the two

pyridine rings are joined by a sp^2-center in a planar conformation, the extension of the π-system does not seem to have a strong effect. Complex **2** shows mostly ligand centered absorption, even though the peak at 300 nm is much more intense than for the ligand on its own, while complex **3** is more or less missing one of the ligand centered peaks around 250 nm. The π-transition at 302 nm is largely increased for the homoleptic complex **2**, it is even bigger than twice the peak of the ligand and is shifted to slightly lower energy, which may be expected due to the doubling of the amount of ligand in a homoleptic complex. In the case of the heteroleptic complex, this peak is smaller than for the ligand itself, which may be due to the different ligands bonded to Ru(II). The region of 350-400 nm shows what may be d-d transitions for complex **2**, while they are observed between 320-350 nm for complex **3**. Both complexes **2** and **3** show a low intensity MLCT peak near 450 nm.

The ligand shows a strong emission at 347 nm due to the two pyridine rings, which is much less intense for the complexes **2** and **3** (Figure 16).

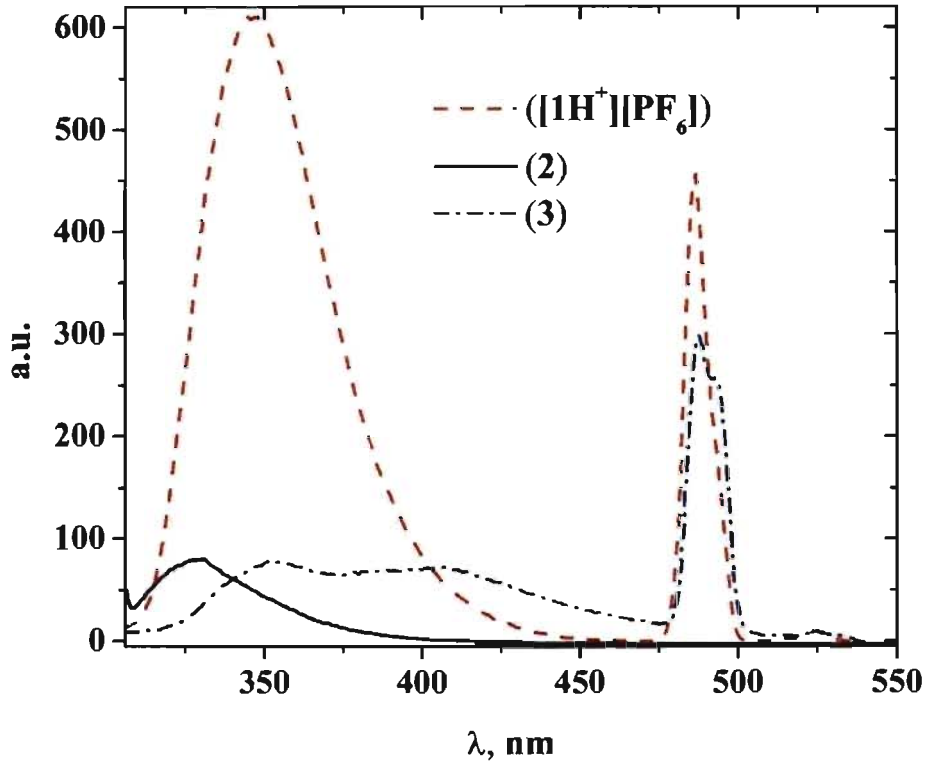

Figure 16. Emission of $[\mathbf{1H^+}][\mathbf{PF_6^-}]$, **2** and **3** at an excitation wavelength of 244 nm in deaerated acetonitrile.

The sharp emission at 488 nm is an artifact due to the excitation wavelength of 244 nm and has been cut-off for complex **2** since it does not have anymore absorptions in this region.

Table II. UV-Vis data for ([**1H**$^+$][PF_6]), (**2**) and (**3**).

compound	absorption λ_{max}, nm (ε, $M^{-1}cm^{-1}$)	emission λ_{max}, nm (I, a. u.)
[**1H**$^+$][PF_6]	244 (39220)	262 (65.48)
	290 (16667)	347 (665.57)
		525 (64.37)
2	245 (40727)	330 (80.62)
	302 (56084)	647 (8.30)
	354 (4189)	
	441 (2037)	
	467 (1808)	
3	244 (10388)	263 (7.07)
	296 (12524)	351 (80.23)
	448 (1658)	405 (74.62)
		525 (10.86)
		688 (1.40)

2.3 Conclusion

A new six membered imidazole ligand has been synthesized together with its homoleptic complex as well as its heteroleptic complex with bromoterpyridine as second ligand. It was expected from literature reports that a carbene ligand should destabilize the metal centered states relative to the ^{3}MLCT state. In the case of the homoleptic complex **2** there is a destabilization for the metal centered states observed in electrochemistry, so that the oxidation of the metal appears at lower values. However, in case of the heteroleptic complex **3** there

seems to be an intra- or intermolecular effect of the electron deficient terpyridine ligand and the electron-rich carbene ligand. The energy of the metal centered states are even closer relative to the ^{3}MLCT than in the $Ru(tpy)_2$ complex.

2.4 Experimental Section

General Procedures. All reactions were performed under an argon atmosphere using standard Schlenk techniques unless otherwise stated. All chemicals were reagent grade and used as received. Solvents were dried by standard methods. 4'-(4-Bromophenyl)-2,2':6'2"-terpyridine and $Ru(Br\text{-}ph\text{-}tpy)Cl_3$ were prepared by literature methods. [32, 33] The syntheses implicating $[\mathbf{1H^+}][\mathbf{PF_6^-}]$ were carried out on small scale only, due to the expensive starting material.

Physical Measurements and Instrumentation. Nuclear magnetic resonance (NMR) spectra were recorded in CD_3CN at room temperature (r.t.) on a Bruker AV400 spectrometer at 400 MHz for ^{1}H NMR and at 101 MHz for ^{13}C NMR. Chemical shifts are reported in parts per million (ppm) relative to residual solvent protons (1.93 ppm for acetonitrile-d_3) and the carbon resonance of the solvent. Absorption spectra were measured in deaerated acetonitrile at r.t. on a

Cary 500i UV-Vis-NIR Spectrophotometer. Experimental uncertainties were ± 2 nm for absorption maxima and 10% for the molar absorption coefficient. Emission spectra were measured in deaerated acetonitrile at r.t. on a Cary Eclipse Fluorescence Spectrophotometer. Experimental uncertainties for emission maxima were approximately ± 5 nm. Electrochemical measurements were carried out in argon-purged acetonitrile at room temperature with a BAS CV50W multipurpose equipment interfaced to a PC. The working electrode was a Pt electrode. The counter electrode was Pt wire, and the pseudo-reference electrode was silver wire. An internal 1 mM ferrocene/ferrocenium sample was used as reference at 395 mV vs SCE in acetonitrile and 432 mV in DMF. The concentration of the compounds was about 1 mM. Tetrabutylammonium hexafluorophosphate (TBAP) was used as supporting electrolyte in concentrations of 0.10 M. Cyclic voltammograms were obtained at scan rates of 50, 100 and 200 mV/s. For irreversible oxidation processes, the cathodic peak was used as E, and the anodic peak was used for irreversible reduction processes. An oxidation/reduction was considered reversible when the the separation between cathodic and anodic peaks was smaller than 60 mV, if the ratio of the intensities of the cathodic and anodic currents was, and if the peak potential remaining constant with changing scan rate. Experimental uncertainty

is ± 10 mV for the redox potentials. Elemental analysis was carried with an Agilent LC-MSD TOF, using ESI as ionization method.

1,3-Di-pyridin-2-yl-3,4,5,6-tetrahydro-pyrimidin-1-ium ([**1H**$^+$][PF_6^-]). A mixture of 1,4,5,6-tetrahydropyrimidine (1.3 ml, 15 mmol) and 2-bromopyridine (7.9 ml, 30 mmol) were heated to 96 °C for 48 h. During this time the clear solution gradually darkened to give a viscous brown liquid. The reaction mixture was cooled to r.t. and added to 75 ml MeOH solution containing a 5-fold excess of NH_4PF_6. The brown solution obtained was kept at 0° C for 2 h during which time the product precipitated. Filtration yielded 1.025 g (18%) of [**1H**$^+$][PF_6^-] as an off-white powder. Anal. calcd. for $C_{14}H_{15}F_6N_4P$: N, 14.58; C, 43.76; H, 3.93. Found: N, 14.40; C, 43.60; H, 3.86. ^{1}H NMR (400 MHz, *CD_3CN*): ppm 10.36 (s, 1H); 8.55 (m, 2H); 8.04 (m, 2H); 7.48 (m, 2H); 4.10 (m, 4H); 2.45 (q, 2H, J=6 Hz). ^{13}C NMR (100 MHz, *CD_3CN*): ppm 18.6; 43.6; 113.3; 124.1; 140.7; 149.2; 149.5. ESI-MS (in CH_3CN): 239 ([**1H**$^+$], 100%)

1,3-Di-pyridin-2-yl-3,4,5,6-tetrahydro-pyrimidin (1)

5 mg (0.013) of **[1H$^+$][PF$_6^-$]** were added to 5 ml anhydrous deuterated benzene containing an excess NaH. The white suspension was stirred at r.t. For 36 h. The solid from the suspension has been left to precipitate and the overstanding solution has been used to obtain an NMR from the unconcentrated solution. ^{1}H NMR (400 MHz, C_6D_6): ppm 8.21 (ddd, J=5,2,1 Hz, 2H), 7.04 (m, 2H), 6.32 (ddd, J=7,5,2, 2H), 5.97 (dt, J=8,1 Hz, 2H), 3.17 (dd, J=6,12 Hz, 4H), 1.48 (dt, J=6,13 Hz, 1H) (1 proton hidden under grease). ^{13}C NMR (100 MHz, C_6D_6): ppm 148.8; 136.9; 125.8; 112.7; 107.1; 39.4; one peak undistinguishable from impurities.

[Ru(1)$_2$][PF$_6$]$_2$, (**2**). $RuCl_3$ (15 mg, 0.07 mol), **[1H$^+$][PF$_6$]** (56 mg, 0.14 mmol) and Et_3N (28 mg, 0.28 mmol) were added to 10 ml ethylene glycol to form a brownish suspension which was heated in a microwave oven at medium heat for 6 min. The brownish-red suspension was cooled to room temperature and added to an aqueous solution containing a 10-fold excess NH_4PF_6. The precipitate was filtered off, redissolved in a minimum amount of CH_3CN and precipitated by addition of Et_2O as yellow microcrystalline powder (18 mg, 86%). Anal. calcd. for $C_{28}H_{28}F_{12}N_8P_2Ru$: N, 12.92; C, 38.76; H, 3.25. Found: N, 14.40; C, 43.59; H, 3.85 . The errors in the elemental analysis are probably due to an incomplete

counter-ion conversion with the NH_4PF_6 salt. ^1H NMR (400 MHz, *CD_3CN*): δ ppm 7.74 (m, 4H), 7.56 (m, 4H), 7.38 (d, *J* = 8 Hz, 4H), 6.79 (m, 4H), 4.26 (m, 8H), 2.81 (q, *J*= 6 Hz, 4H); ^{13}C NMR (100 MHz, *CD_3CN*): δ ppm 157.6, 140.2, 122.1, 111.8, 42.35, 21.75. Even with longer relaxation times and an increase in the number of scans, the carbene center could not be observed. ESI-MS (in CH_3CN): 723.111 $(M\text{-}PF_6)^+$, 289.074 $(M\text{-}2PF_6)^{2+}$.

[Ru(Br-ph-tpy)(1)][PF_6]$_2$, **(3)**. Ru(Br-ph-tpy)Cl_3 (60 mg, 0.1 mmol) and **[1H$^+$][PF_6]** (40 mg, 0.1 mmol) were added to 8 ml ethylene glycol to form a brownish suspension which was heated to 180 °C for 1.5 h, during which it turned wine-red. The reaction mixture was cooled to r.t. and added to an aqueous solution containing a 10-fold excess NH_4PF_6. The precipitate was filtered off, redissolved in a minimum amount of CH_3CN and recrystallized from Et_2O. The obtained solid was purified by column chromatography on silica (eluent 7:2 CH_3CN : sat. KNO_3 aq.). The first band contained the product while the second band contained the homoleptic complex **Ru[1]$_2$**. The complex was then reconverted to its PF_6 salt and recrystallized from Et_2O. Yield: 53 mg, 52% of an orange powder. ESI-MS (in CH_3CN): 872.581 $(M\text{-}PF_6)^+$, 363.811 $(M\text{-}2PF_6)^{2+}$. ^1H NMR (400 MHz, *CD_3CN*) δ ppm 8.95 (s, 2H), 8.59 (d, 2H, J = 8

Hz), 8.08 (d, 2H, J = 8 Hz), 7.93 (m, 6H), 7.74 (d, 2H, J = 7 Hz), 7.43 (d, 2H, J = 8 Hz), 7.20 (s, 2H), 7.04 (d, 2H, J = 4 Hz), 6.75 (m, 2H), 4.35 (t, 4H, J = 6 Hz), 4.24 (m, 2H); ^{13}C NMR (100 MHz, *CD_3CN*): δ ppm 284.4, 163.7, 159.2, 157.6, 156.2, 154.4, 152.4, 149.7, 140.6, 139.2, 134.1, 131.0, 128.5, 125.9, 122.4, 121.9, 113.9, 112.52, 43.3, 30.83

X-ray crystallography. The crystallographic data for **[1H$^+$][PF$_6$]**, **[1]$_2$** and **2** ·CH_3CN is summarized in Table III. Suitable crystals for x-ray crystallography of **[1H$^+$][PF$_6$]** and **2** were obtained by slow diffusion of Et_2O into acetonitrile solutions of the respective compound, compound **[1]$_2$**. was crystallized by slow evaporation of a benzene solution in an NMR tube. A Bruker Smart 6000 diffractometer using graphite-monochromatized Cu Kα radiation was used for data collection. Absorption corrections were carried out using Sadabs [34]. Structures were solved using direct methods [35, 36]. All non-hydrogen atoms were refined anisotropic by least-squares procedures based on F^2. [37] Hydrogens were refined on calculated positions with fixed isotropic U, using riding model techniques. Crystallographic data (excluding structure factors) for the structures are shown in appendix A.

Table III. Crystallographic data for $[\mathbf{1H^+}][\mathbf{PF_6}]$, $[\mathbf{1}]_2$ and $\mathbf{2}\cdot CH_3CN$

	$[\mathbf{1H^+}][\mathbf{PF_6}]$	$[\mathbf{1}]_2$	$\mathbf{2}\cdot CH_3CN$
chem. formula	$[C_{14}H_{15}N_4][PF_6]$	$C_{28}H_{28}N_8$	$[C_{28}H_{28}N_8Ru][PF_6]_2\cdot CH_3CN$
M_w, $g\cdot mol^{-1}$	384.27	476.644	908.63
crystal size, mm	0.20 x 0.15 x 0.15	0.24 x 0.14 x 0.08	0.22 x 0.16 x 0.08
crystal system	monoclinic	monoclinic	monoclinic
space group	$P2_1/c$	$P2_1/c$	$P2_1/c$
a, Å	8.8907(1)	10.5459(4)	8.6113(1)
b, Å	11.4813(1)	12.8430(5)	8.9270(1)
c, Å	15.5497(2)	9.2601(3)	46.1772(7)
β, deg	103.465(1)	111.587(2)	93.415(1)
V, $Å^3$	1543.63(3)	1166.2(1)	3543.48(8)
Z; D_c, Mg m^{-3}	4; 1.653	2; 1,3574	4; 1,703
μ, mm^{-1}; F_{000}	2.288; 784	0.672; 504	5.363; 1824
θ, deg	2.92 - 68.99	4.51- 69.18	3.84 - 68.86
temperature, K	150	100	150
indep. reflns. (R_{int})	2847(0.027)	2147 (0.108)	6530 (0.029)
obsd reflns. [I ≥2σ(I)]	2752	1685	5958
no. of variables	227	164	525
GooF	1.036	0.539	1.062
R1 [I>2σ(I)]	0.0307	0.0485	0.0300
wR2 [all data]	0.0802	0.1508	0.0835
res. electron density	0.198	0.270	0.971

3 Structural and Magnetic Properties of Fe(II) Terpyridine Coordination Complexes and Polymers

"Nothing unreal exists"

Kiri-kin-tha's First Law of Metaphysics

3.1 Introduction

Polymers play a substantial role in the modern society due to the vast variety of their physical and chemical properties as well as their widespread commercial applications [38]. Traditional polymer science is concerned with covalently formed polymers, where the monomers are linked by covalent bonds [39]. The so-formed covalently bonded polymers have well-defined (static) molecular weight distributions that define their physical properties. During the last decades, attention has turned to a new class of polymers, supramolecular polymers in general and coordination polymers in particular. Here, self-assembly has been adopted for the synthesis of different polymers (Figure 17).

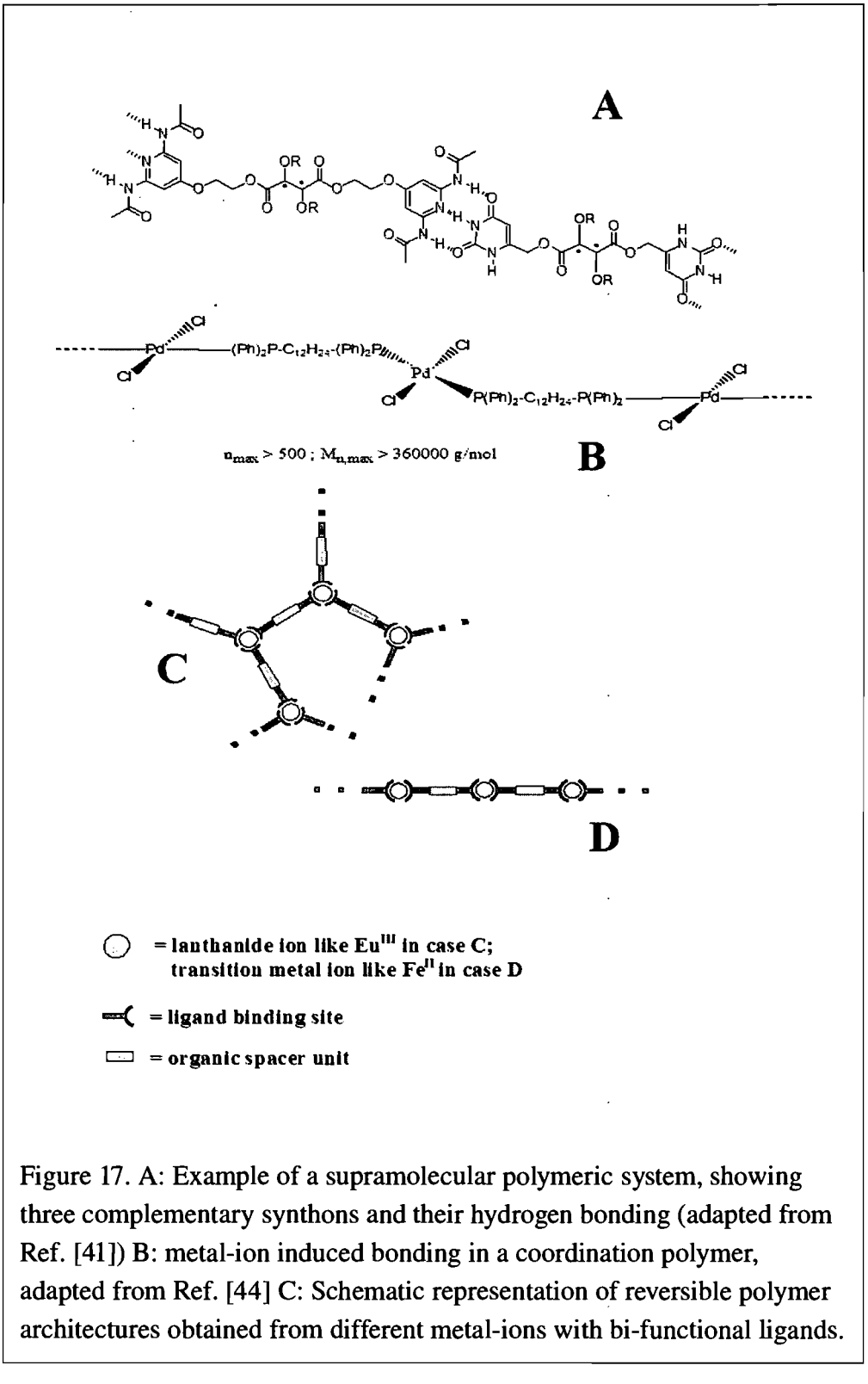

Figure 17. A: Example of a supramolecular polymeric system, showing three complementary synthons and their hydrogen bonding (adapted from Ref. [41]) B: metal-ion induced bonding in a coordination polymer, adapted from Ref. [44] C: Schematic representation of reversible polymer architectures obtained from different metal-ions with bi-functional ligands.

There are different non-covalent interactions available for these types of polymer assemblies. The most utilized example is hydrogen bonding [40], but also π-π-stacking [41], van der Waals interactions [41] and metal ion coordination have been used. It is the latter that we will be concerned with in this chapter. The fusion of traditional polymer chemistry with supramolecular chemistry results in a generation of materials that are designed to use directional interactions and recognition processes on the molecular level [42]. Lehn recognized early on that it was helpful to consider these materials as (virtual) dynamic combinatorial libraries [43]. Most important in this approach is this reversibility of the interactions, that leads to dynamic systems whose properties depend on the extent of this reversibility. It also is a means to control / manipulate features such as chain length and geometry, thus allowing for subsequent rearrangement at the molecular level.

Dynamic coordination polymers (DCPs) can be considered a fusion of traditional organic polymers with inorganic coordination chemistry. These polymers are now intensely studied due to their unusual properties provided by the metal ion, e.g. molecular-magnetism, [45-50] synthetic metallic conduction, [51-54] non-linear optics [55-58] and ferroelectrics, [59-62] and this, in

combination with the outstanding mechanical properties of conventional polymers. The possibility to modify their magnetic, electric and optical properties as well as their morphology by the choice of the involved metal ions and the manipulation of its redox properties in addition to the ligands opens pathways to a completely new class of functional materials. Of special interest here are supramolecular coordination polymers that are formed spontaneously in solution via a metal ion induced self-assembly process [63].

The idea to use single molecules or molecular assemblies as electronic devices is a very tempting one, with probably the most popular example being the molecular switch [64]. In order for a molecular switch to work, a bi-stable system is needed, meaning a molecular system that is able to switch reversibly (and detectably) from one stable state to another in response to external stimuli. In addition to that, the system also needs to be controllable and readable on the molecular level to provide a useful switch. The spin cross-over phenomenon is quite popular in this regard as it is a good example for bi-stability and is observed in solution as well as in the solid state [65]. For first row transition metals having the d^4-d^7 configuration in an octahedral geometry, there are two possible ground state configurations with different multiplicities: the low-spin

(LS) state in which the ligand field splitting parameter Δ between the t_{2g} and e_g sets of the d-orbitals is higher than the spin-pairing energy and the opposite case, that gives rise to the high-spin (HS) state. In cases where the spin-pairing energy is in the same range as Δ, the two states can interconvert into each other, triggered by an external stimulus such as T, p or λ. [9] If the energy separation Δ between the t_{2g} and e_g orbital sets is of the order of kT, there will be a pronounced effect of the temperature on the position of this equilibrium, which renders them switchable. The Fe(II) systems are of particular interest, since the low spin state is diamagnetic and the change in the number of unpaired electrons while going to high spin is four. This also means, that the change in the magnetic moment of the complex will be a relatively pronounced one, thus allowing an easy detection of the cross-over point and the determination of the field splitting parameter Δ. Such a spin transition is accompanied by pronounced changes of the systems' physical properties (e.g. spectroscopic: color change; magnetic: diamagnetic (LS) ↔ paramagnetic (HS)). This implies that the spin transition is detectable and can be followed with spectroscopic methods (e.g., UV-vis spectroscopy, as the spin transition is accompanied by a color change) or magnetic susceptibility measurements. In addition to that, it is also accompanied by a structural change: a spin transition can be regarded as a

$t_{2g} \leftrightarrow e_g$ charge transfer, which implies changes in the population of these orbitals and hence in the metal-ligand bond length [12].

It is known that the 2,2':6',2" terpyridine induces a strong ligand field and as a result, $[Fe^{(II)}(tpy)_2]\ X_2$ complexes are generally low spin [14], but it has recently been suggested that bulky substituents in the 6- and 6"-position of the tpy-ligand influence the spin state. Kurth et al. introduced a new approach to manipulate the spin state by introducing mechanical strain through an amphiphilic phase transition [12]. They investigate a $Fe^{(II)}$ terpyridine coordination polymer whose counterions are replaced by charged amphiphiles (Figure 18).

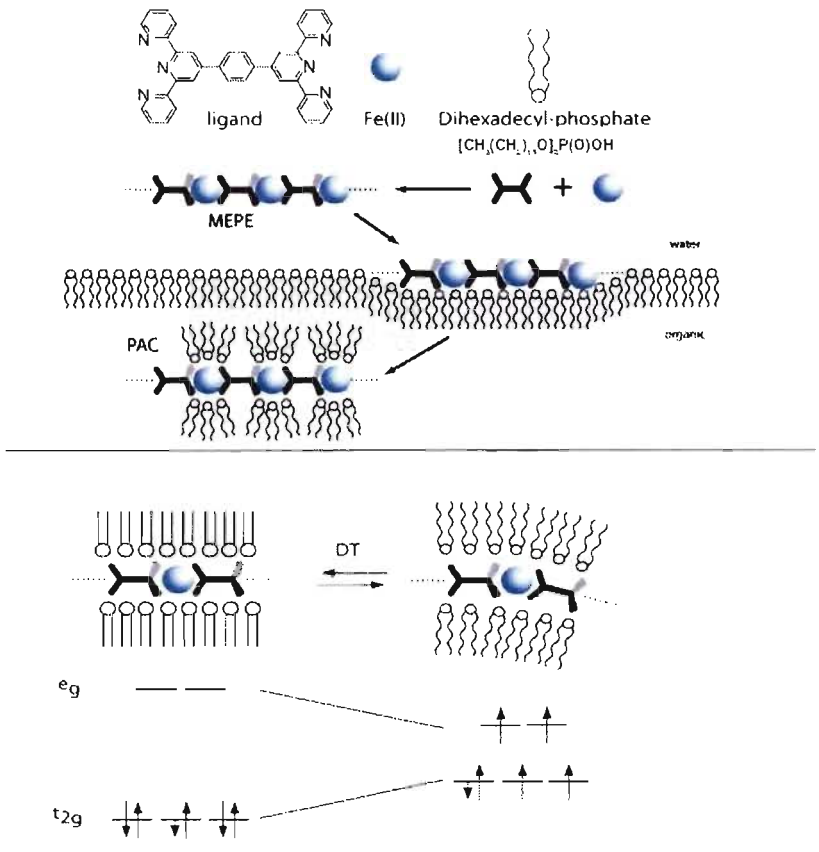

Figure 18. (Top) Self-assembly of ditopic ligand **1** and $Fe(OAc)_2$ results in the formation of the linear, rigid-rod-type metallo-supramolecular polyelectrolyte (MEPE). In a consecutive step, MEPE is assembled with dihexadecyl phosphate, resulting in formation of the corresponding polyelectrolyte amphiphile complex (PAC). The amphiphiles render the MEPEs soluble in organic solvents [66]. Spreading PAC at the air-water interface and subsequent transfer of the Langmuir monolayers on a solid support results in a well-defined multilayer, a section of which is schematically shown in the bottom of the scheme. (Bottom) Upon heating of the multilayer, the alkyl chains of the mesophase melt, resulting in a distortion of the metal ion coordination geometry. The unfavorable coordination of the terpyridines around the Fe(II) cation results in a lowering of the energy gap between the d-orbital subset, giving rise to a reversible transition from a diamagnetic low-spin state to a paramagnetic high-spin state [9, 12].

These Fe(II) complexes in an octahedral ligand field can adopt both, the low spin $^1A_{1g}$ and high spin $^5T_{2g}$ conformations. However, in this case, it is not the spin transition that is accompanied by structural changes, but a forced structural change of the system that induces the spin transition. In this case, the studied coordination polymer is built starting from a rigid ditopic ligand that, combined with an appropriate amount of first row transition metal ion, spontaneously assembles into a linear, rigid-rod type, positively charged polymer (Figure 18). This linear arrangement is due to the octahedral coordination geometry of the metal. The ditopic ligand needs to be rigid enough to prevent ring formation; otherwise lower molecular weight species will be favored due to entropic reasons [67]. The investigated system is water-soluble; such systems are easy to handle and well suited for industrial applications on a large scale as they do not produce large quantities of organic solvent waste, for example. Importantly, the chain length of these polymers varies with the metal-to-ligand ratio, with the maximum chain length being obtained at about equimolar amounts of metal ion and ligand, which makes it inevitable to weigh the samples with high precision.

The magnetic properties of this system are studied in a Langmuir-Blodgett multilayer. These films are applied onto planar solid substrates by means of

electrostatic layer-by-layer self-assembly (ELSA).

It is now interesting to prove if this spin transition is really induced by the structural change of the amphiphiles on the octahedral structure around the metals of the MEPE chain. To obtain more information about this system, the corresponding mononuclear complexes have been synthesized and their structural37behaviour as well as their magnetic properties have been studied with and without amphiphiles in the same manner as the MEPE and PAC chains.

3.2 Results and Discussion

The compounds investigated in this chapter are listed in Table IV together with their denotation.

Table IV. Compounds investigated together with their denotation.

Compounds	**Denotation**
$[Fe(ph\text{-}tpy)_2][OAc]_2$	MNC_OAc
$[Fe(ph\text{-}tpy)_2][SO_4]$	MNC_SO_4
$[Fe(ph\text{-}tpy)_2][DHP]_2$	MAC_2
$[Fe(ph\text{-}tpy)_2][DHP]_4$	MAC_4
$[Fe(tpy\text{-}opropo\text{-}tpy)_n][OAc]_{2n}$	MEPE
$[Fe(tpy\text{-}opropo\text{-}tpy)_n][DHP]_{4n}$	PAC_4
$[Fe(tpy\text{-}opropo\text{-}tpy)_n][DHP]_{6n}$	PAC_6

The mononuclear acetate complex (MNC_OAc) was synthesized by the same procedure as the already known MEPE chains, by adding the necessary amount of terpyridine ligand to an $Fe^{II}(OAc)_2$ in glacial acetic acid and stirring the solution for 24 h at r.t. (Scheme). The Fe(II)acetate is prepared *in situ* as it is difficult to store, because the Fe(II) tends towards its +III oxidation state in the presence of oxygen. Once the terpyridine complex is formed, the oxidation state of the iron is stable. The Fe(II) complex is then added to a solution of dihexadecylphosphate (DHP) to replace the acetate counterions with DHP (Scheme 6) to form the corresponding mononuclear amphiphile complexes (MAC).

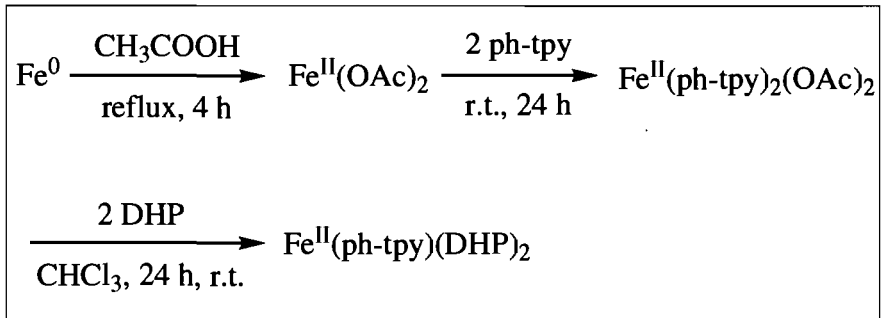

Scheme 6. Example for the assembly of MNC_OAc and MAC_2. The MAC_4 complex was synthesized in the same way, with four instead of two equivalents of DHP.

Presumably, two of the DHP's are deprotonated to replace the acetate counter ions, while the additional DHP's are forming a hydrogen bonded network,

which binds through to the MNC by electrostatic interactions, as it has been seen for the corresponding coordination polymers [68]. In the following, the anionic DHP's will be referred to as $[DHP]^-$ and the neutral ones as DHP-H.

The MNC_SO_4 was synthesized using the method published for the synthesis of $[Fe(tpy)_2]SO_4$ [69] by stirring $FeSO_4 \cdot 7\ H_2O$ with 2 equivalents of ph-tpy in ethanol.

There are two classes of soluble transition metal coordination complexes: a) those that are based on kinetically inert transition metal complexes, which are stable in solution and are thus readily characterized by standard analytical tools and b) those based on kinetically labile transition metal complexes, that form soluble equilibrium compounds under appropriate conditions. In the former case, we usually deal with second and third row metals like Pt, Pd or Ru that provide substitution inertness [70]. Synthesis of these compounds generally does not occur under ambient self-assembly conditions due to the slow ligand-exchange kinetics. The resulting compounds may, therefore, not be dynamic equilibrium systems. The latter usually contain first row metals in their typical +II or +III oxidation state, such as Fe, Co or Ni. In general, these metals exchange their ligands more rapidly so self-assembly occurs under ambient

conditions and the compounds can be considered to be in equilibrium or quasi-equilibrium. The kinetics for metal ligand exchange reactions depend on the metal ion [9]. The assumption that decomposition (disassembly) occurs exclusively via ligand replacement reactions as stated by Rehahn et al. leads to two possible routes to study these dynamic compounds, one of which would be to exclude all coordinating solvents or other molecules that could compete with the ligands for the metal ion [71]. On the other hand, chelating polydentate ligands can be used with binding constants that exceed the ones of other competing molecules, solvent or otherwise. Since the Fe(II) complexes investigated here are labile transition metal complexes, this dynamic behavior will temper with solution dependent analysis. In mass spectrometry, the conditions of the analysis even lead to the decomposition of the complex. Since the MNC_OAc is not soluble in any organic solvents, NMR samples, the samples all need to be analyzed in acetic acid, so that the δ change of the signal in comparison to the counter ion exchange can be analyzed. However, the samples incorporating $[DHP]^-$ counter ions are only partially soluble in acetic acid and these spectra show a doubled signal set, one for the DHP-complex and one from the acetate complex, that occurs due to the back-reaction of the DHP-complex with the acetic acid NMR-solution (Figure 19).

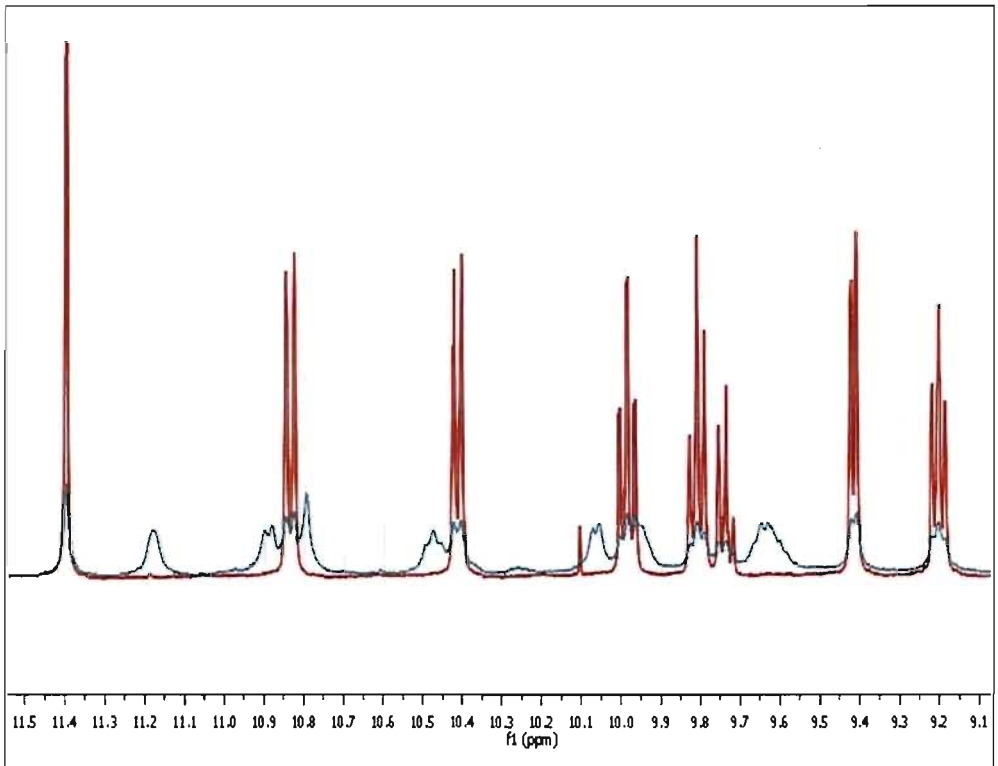

Figure 19: ^{1}H NMR spectra of the iron(II) complex with OAc (red) and DHP (blue) counter ions in acetic acid-d4, showing the back-reaction of the DHP-complex to the OAc-complex.

So only methods that imply the use of solid samples, such as elemental analysis, are reliable for the analysis of the samples composition.

To obtain data about the spin transition in mononuclear complexes, three compounds were analyzed: the mononuclear iron(II) coordination complex with acetate counter ions (MNC_OAc) and the corresponding 1:2 (MAC_2) and 1:4 (MAC_4) amphiphile complexes containing a 1:2 ratio of $[DHP]^-$ and a 1:4 ratio, incorporating 2 $[DHP]^-$ and 2 DHP-H (Figure 20).

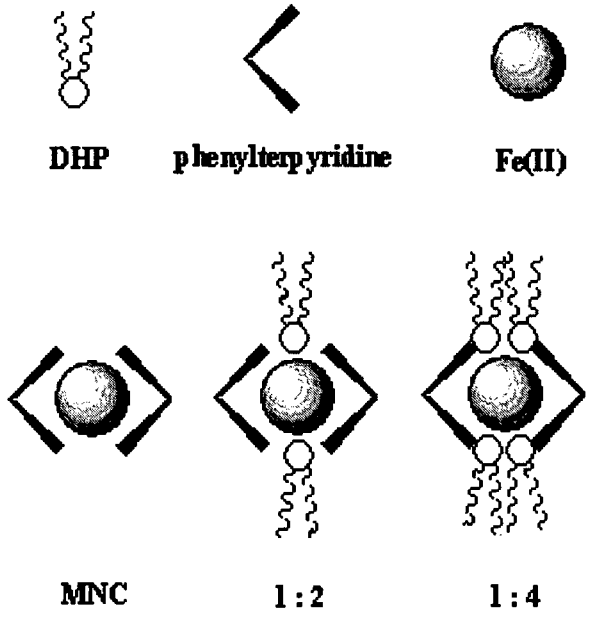

Figure 20. Schematic representation of the kind of investigated compounds. MNC: complex containing acetate counter ions. 1:2: complex containing 2 $[DHP]^-$ counter ions. 1:4: complex containing 2 $[DHP]^-$ as counter ions and 2 DHP-H electro-statically bonded.

3.2.1 Structural Analysis

The obtained compounds have first been analyzed with small angle X-ray scattering to obtain data about its structure. Small angle scattering of X-rays is observed from almost all kinds of matter, and it is widely used in structural studies of non-crystalline materials at relatively low resolution. The term "small

angle" here refers to the angular range within a few degrees, containing structural information on the order of approximately a nanometer to submicrometers. There are a few aspects of synchrotron radiation that have made small angle scattering studies much more effective: very small beam divergence, high beam flux, and energy tunability [72]. It is crucial to have small beam divergence in order to isolate weak scattering at very small angles from the direct beam which is orders of magnitude stronger. The high beam flux allows one to use a smaller beam size, resulting in better isolation of scattering from the direct beam. The flux level at a synchrotron source is usually several orders of magnitude higher than those from conventional X-ray sources, thus studies of weak scatterers have become much more practical. The high flux beam also made it possible to conduct time-resolved measurements of small angle scattering. It is possible to conduct anomalous small angle X-ray scattering only when beam energy tunability of synchrotron radiation is used. A scheme of the experimental set-up of the energy-dispersive reflectometry (EDR) beamline at BESSY II is presented by Figure 21.

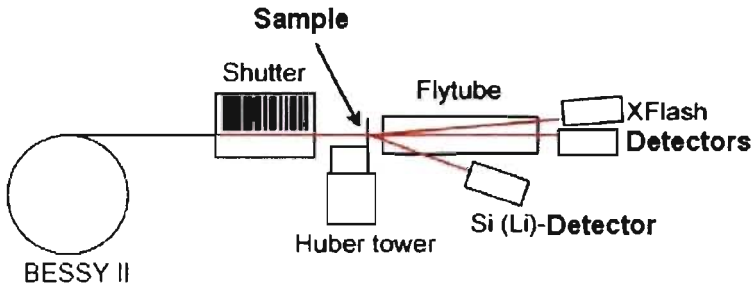

Figure 21. Scheme of the experimental set-up of the energy dispersive refraction (EDR) beamline at Berliner Elektronenspeicherring-Gesellschaft für Synchrotronstrahlung (BESSY II), located in Berlin-Adlershof.

To minimize scattering from the air, a flight tube is needed for the measurements. In this case, we used a liquid waste tube which was covered at the front and back end with a poly(4,4'-oxydiphenylene-pyromellitimide) (Kapton) foil (see Figure 22).

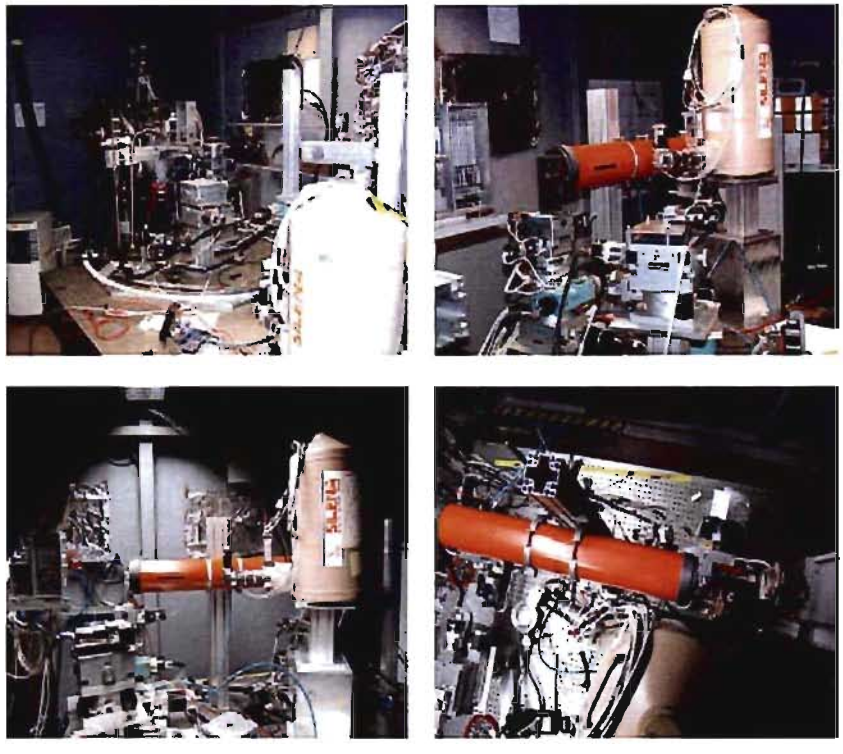

Figure 22. The photos show the experimental set-up at BESSY II. In front of the flight tube, the specimen holder can be seen. The sample is fixed in between two Kapton foils.

In addition to that, the tube had a slot at the side for a Silena detector. In the flight tube, a vacuum of about 5 mBar is induced during the measurements. The additional peak which is induced by the Kapton foil during the measurements, appears at $q = 0.35$ Å^{-1} and needs to be subtracted from the measurements.

The data obtained from the SAXS measurements is shown by Figure 23.

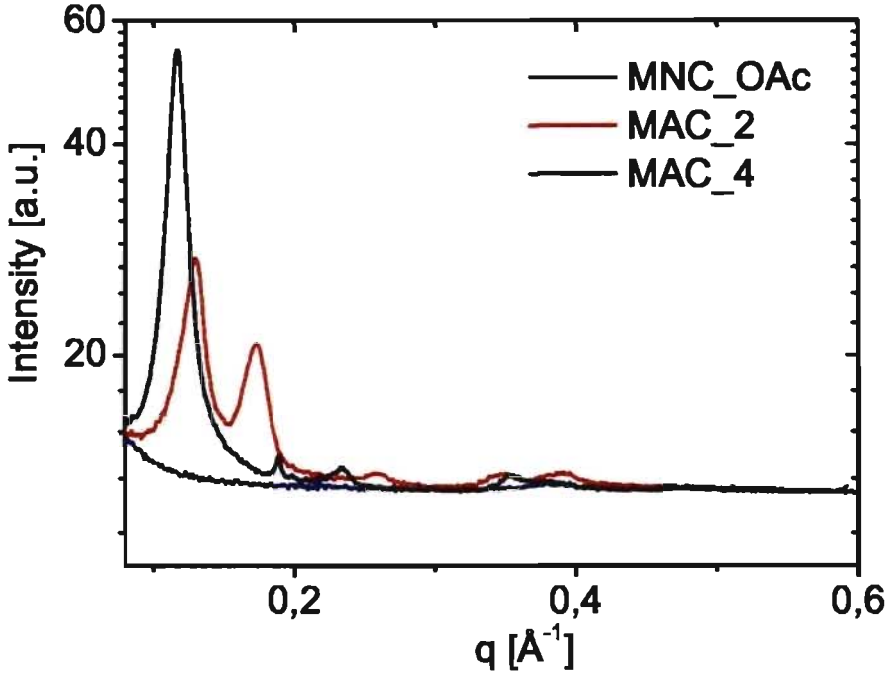

Figure 23. SAXS curves showing the log of the structural intensity against transfer momentum: black, MNC_OAc; blue, MAC_2; red, MAC_4.

The MNC_OAc complex does not show any structural peak, so there is no structural order observed for this compound. The MAC_2 and the MAC_4 show both several order peaks due to a structural order in this compounds. The peak data is shown by Table V.

Table V. SAXS data for compounds MAC_2 and MAC_4, giving the values for the reciprocal space, q , in $Å^{-1}$ and the distance of the layers, d, in Å.

compound	q / $Å^{-1}$ (± 0.002 $Å^{-1}$)	order of the peak	d / Å (± 0.3 Å)
MAC_2	0.129	first order, structure 1	48.5
	0.259	second order, structure 1	
	0.391	third order, structure 1	
	0.173	first order, structure 2	36.3
	0.350	second order, structure 2	
MAC_4	0.117	first order, structure 1	53.7
	0.233	second order, structure 1	
	0.188	first order, structure 2	33.4
	0.353	second order, structure 2	

The MAC_2 structural data reveals as highest intensity peak the first order peak with two equidistant scattering peaks. These peaks correspond to a lamellar structure with a translational period of 48.5 Å. This is in the same range as the peak of the polyelectrolytes studied before, which corresponds to a double layer of the amphiphile packaging with a Bragg distance of 41 Å and is consistent with a hexagonal packing of the alkyl chains.[12, 68] The value found for the MAC_2 is slightly higher than the before published value for the tpy-ph-tpy metallo-supramolecular coordination polyelectrolyte (tpy-ph-tpy MEPE) studied by our group. This probably means, that the alkyl chains are not completely interdigitated as they are in the tpy-ph-tpy MEPE structure, but form a structure were the alkyl chains are only partially interdigitated which leads to a slightly

increased layer of 48.5 Å (Figure 24).

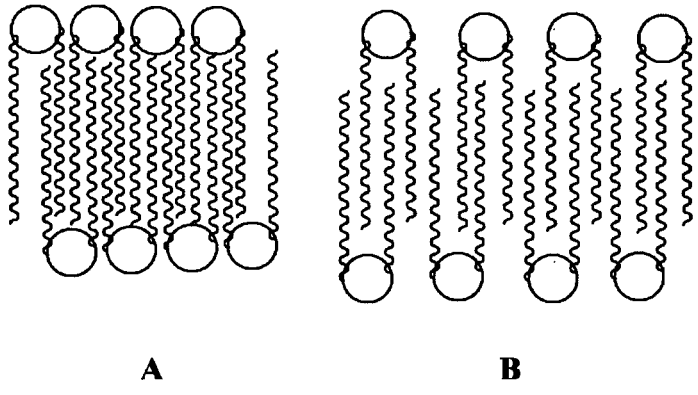

Figure 24. Amphiphile structure. A: completely interdigitated alkyl chains as found for MEPE with the tpy-ph-tpy as bridging ligand.[68] B: with incompletely interdigitated alkyl chains as supposed to be in the MAC_2 complex.

Another first order Bragg peak with almost the same intensity is observed at 0.173 $Å^{-1}$ with two other peaks at equidistant spacing. These peaks suggest a stack-of-layers superstructure with a translational period of 36.3 Å. This distance corresponds well with the values found for tpy-ph-tpy MEPES before and belongs to a monolayer of the amphiphiles.[73] The same two structures are observed for the MAC_4 complex. However, in this case, the first order peak corresponding to the double layer is much more intense than the one belonging to the monolayer. This means that in the structure formed by the complex with a 1:4 amphiphile ratio, MAC_4, most of the domains correspond to a double layer

while there are only very few monolayer domains. In the complex with the smaller amphiphile ratio of 1:2, MAC_2, both kinds of packages, the bilayer and the monolayer, are observed in almost the same intensity. The peak-width analysis (e.g. full width at half maximum, FWHM) reveals a correlation length of coherent scattering for layers of about 422 Å, corresponding to 8-9 bilayers, and 357 Å, corresponding to 10-11 monolayers, in MAC_2. In case of MAC_4, the correlation length of coherent scattering is about 465 Å, corresponding to 8 - 9 bilayers, while the first order peak for the monolayered structure is too small and broad for peak-width analysis.

These results mean, that the amphiphiles seem to be dominant in the structural arrangement and that this arrangement seems to lead to only enough room for the mononuclear complex to arrange in the same way as the tpy-ph-tpy MEPE chains.The space left in between the amphiphile layers needs them to arrange into a similar linear arrangement. It is probable, that the amount of amphiphiles leads to the different structures; if there is only a 1:2 ratio of the complex to amphiphiles, they arrange in more spacing monolayers, while they arrange into an interdigitated structure at an amphiphile ratio of 1:4.

3.2.2 Magnetic Properties

There are several methods to determine the magnetic properties of a compound, two of them are the superconducting quantum interference device (SQUID) and the Faraday balance, which will be shortly described in the following paragraph. Two of the three magnetic susceptibility measurements were carried out with the SQUID. However, for the third measurement there were no more measuring periods available, so this compound was analyzed by a Faraday balance.

3.2.2.1 SQUID

The SQUID is one of the most sensitive devices to measure magnetic dipole moments and it is about 3-4 orders of magnitude more sensitive than the Faraday balance. A photo of the SQUID apparatus used is shown by Figure 25 (measurement threshold for a SQUID: 10^{-14} T) [74].

Figure 25. The picture shows the Quantum Design SQUID that was used for the measurements. With this machine, it is possible to measure in the temperature range of $4K \leq T \leq 400K$ and with magnetic fields up to 7 Tesla.

However, measurements in a SQUID are limited by the upper temperature of 400K, which is the highest temperature obtainable in this instrument. It consists of two superconductors separated by thin insulating layers to form two parallel Josephson junctions. A Josephson junction is made up of two superconductors, separated by an insulating layer so thin that electrons can pass through. A SQUID consists of tiny loops of such superconductors employing Josephson junctions, to achieve superposition: each electron moves simultaneously in both directions (Figure 26).

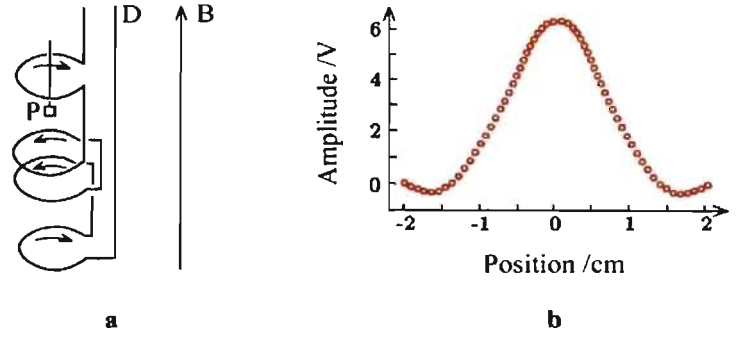

Figure 26. A point shaped sample is routed through the exploring coil of the SQUID (a) and leads to a voltage signal in its oscillating circle (b).

Because a SQUID measures changes in a magnetic field with such sensitivity, it does not have to come into direct contact with the investigated compound. A schematic representation of a SQUID is shown below (Figure 27).

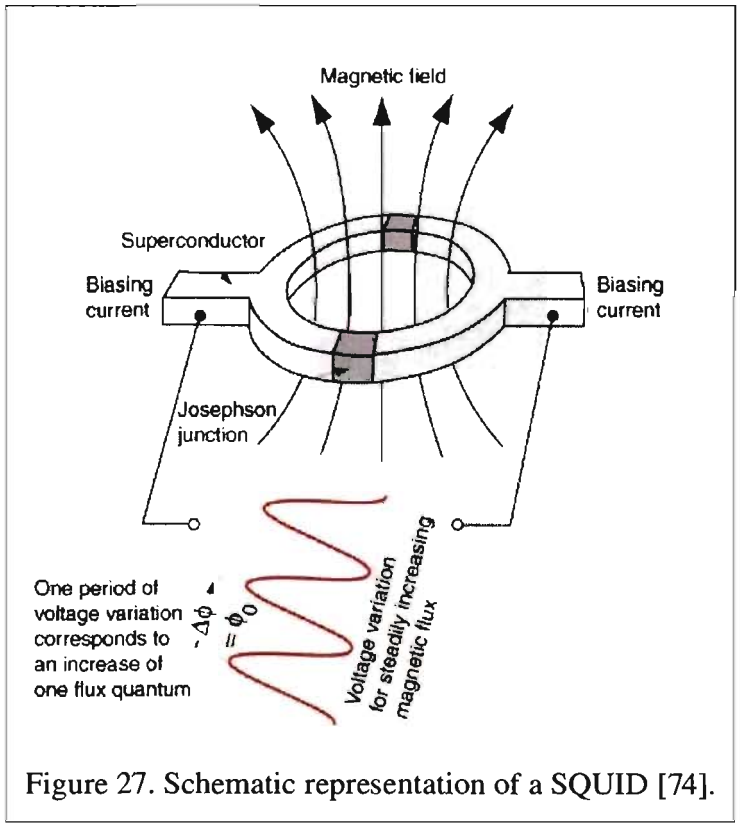

Figure 27. Schematic representation of a SQUID [74].

3.2.2.2 Faraday Balance

A Faraday Balance is an equipment for the detection of magnetic moments by measuring the force on a sample in an inhomogeneous magnetic field, generated by an electromagnet between two dedicated, so-called, Faraday pole caps (Figure 28). During the measurements, a sample is brought into an elevated magnetic field of usually $B \approx 1$ T, while measuring the force F from the difference in apparent sample mass with, respectively, the magnet switched on and off. The force can be measured with an analytical balance (resolution of the order of 10^{-2} milligram) at which the sample is suspended.

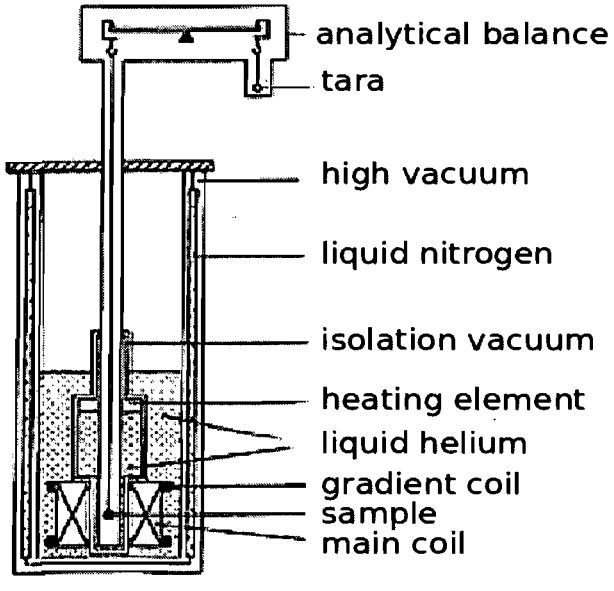

Figure 28. Representation of a Faraday balance [75].

If the sample is at a position where the field gradient is known, the magnetic moment, which is directly proportional to the detected force, can be evaluated from the calibration constants.

The sample is introduced into the balance in a little basket made from ultrapure quartz glass that is not interfering with the magnetic measurements. This little basket is hanging on a fiber made from the same quartz glass. To obtain reproducible results, it is also important to subtract the diamagnetic contribution of the measured susceptibility. These diamagnetic contributions are available in standard literature [72].

Some pictures of the home-made Faraday balance used are shown below (Figure 29).

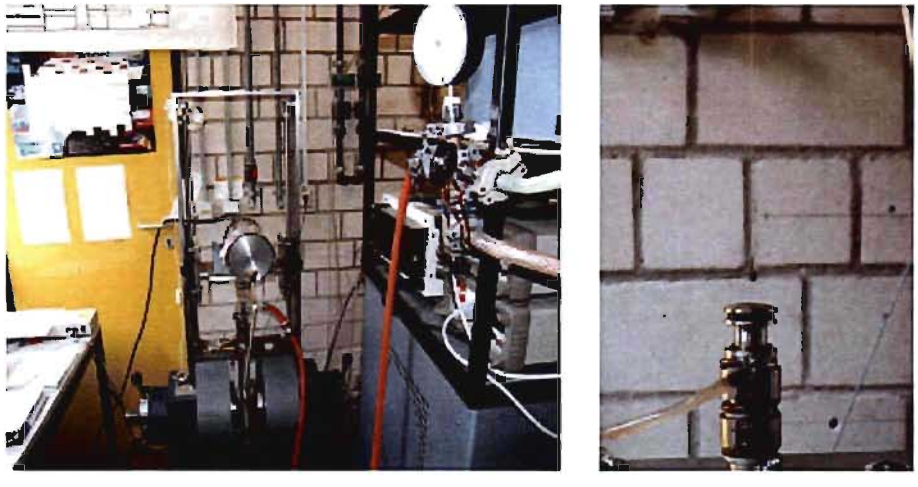

Figure 29. Left: Faraday balance used for high temperature measurements. Right: Zoom of the little quartz glass basket with a MNC sample.

3.2.2.3 Magnetic Measurements

The magnetic measurement curves are shown below (Figure 30). They are diagrammed together with the results from DSC, to investigate if the spin transition is observed in the melting range of the amphiphiles.

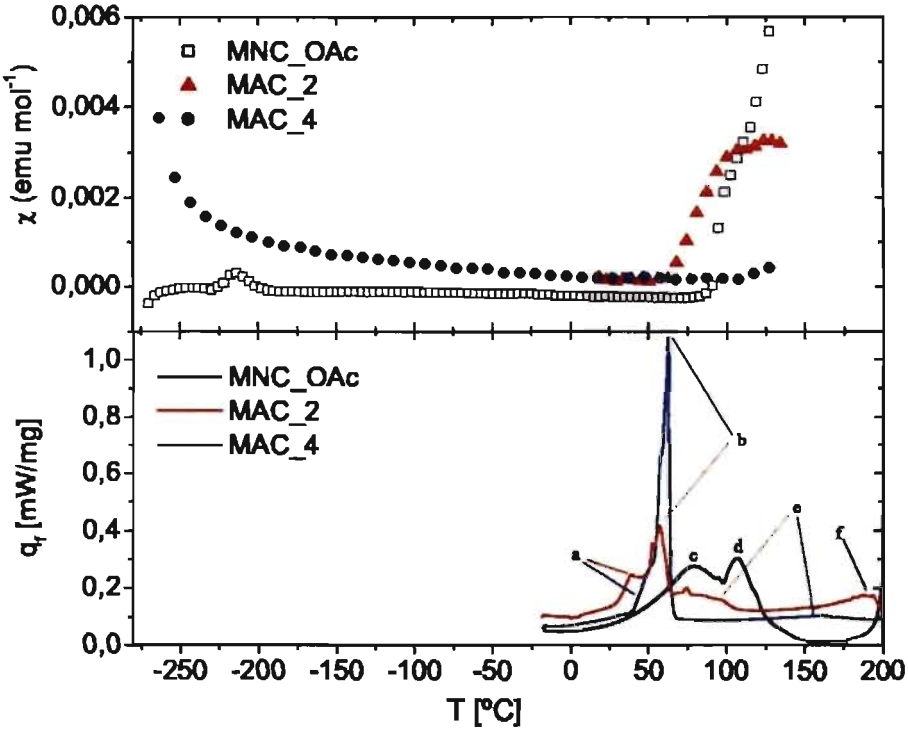

Figure 30. Up: magnetic susceptibility measurements for MNC_OAc and MAC_4 measured with SQUID; for MAC_2 measured with a Faraday balance. Down: DSC measurements for MNC_OAc, MAC_2 and MAC_4.

For the MNC_OAc sample, there is only a temperature-driven spin transition

around 100 °C and there is no net magnetization of this compound below that temperature; χ is negative. There are no structural changes observed from the DSC curves. The processes referred to as *c* and *d* in Figure 30 are the water and acetic acid evaporation, respectively. These values are much lower than for the bulk material, but were always observed by our group in MNC or MEPE samples. As stated in the molecular motion theory, the evaporation of a liquid into a gaseous state can only occur when the kinetic energy of the liquid is high enough to overcome the intermolecular interaction potential energy. If this energy is weaker than in the pure compound, this will lead to a lower boiling point of the mixture. In addition to that, if there is an association between the components of the pure compound which is broken by the addition of another component that disturbs this contact, the boiling point will also go down. Both, water and acetic acid, have a random continuous hydrogen bonding network, which seems to be disturbed by the presence of the charged metal complexes and leads to the lower temperature of evaporation seen in the DSC curves. [76]

The DSC curves for MAC_2 and MAC_4 show the same transitions: the peak observed at *a* is characteristic for the loss of the hexagonal structure in the amphiphiles; this effect has been seen for the tpy-ph-tpy MEPE chains as well

and is supposed to be a loss of positional correlation within the plane of the alkyl chains.[77] The transition *b* is the melting of the amphiphiles, followed by another structural change, *e*. It is this change in the amphiphile structure that induces the spin transition and not the melting of the amphiphiles. In comparing the temperature of the spin transition with the melting point of the amphiphiles, it can be seen that the spin transition occurs after the melting process. Shortly after the melting of the amphiphiles, another structural change takes place, which seems to trigger the spin transition. At the temperature where the spin transition occurs [77]. Interesting here is also the fact that MAC_2 and MAC_4 have a net paramagnetic moment at room temperature. So, the structure induced by the amphiphiles already induces a magnetic moment. The transition *f* finally shows the destruction of the complexes MNC_OAc and MAC_2. In case of the complex MAC_4 there is no destruction of the complex observed up to 200°C. It seems that the higher amount of amphiphiles in this complex leads to a structure that is protecting the metal complex, so that its destruction occurs at higher temperatures.

Furthermore, we wanted to study if the counter ion of the complex does have an effect on the magnetic moment. To obtain another water soluble $Fe(ph\text{-}tpy)_2$

complex, we synthesized the $Fe(ph\text{-}tpy)_2$ compound with SO_4^{2-} as counter ion. This complex as well as the corresponding acetate complex were measured in a high temperature Faraday balance to observe their temperature dependent magnetization (Figure 31).

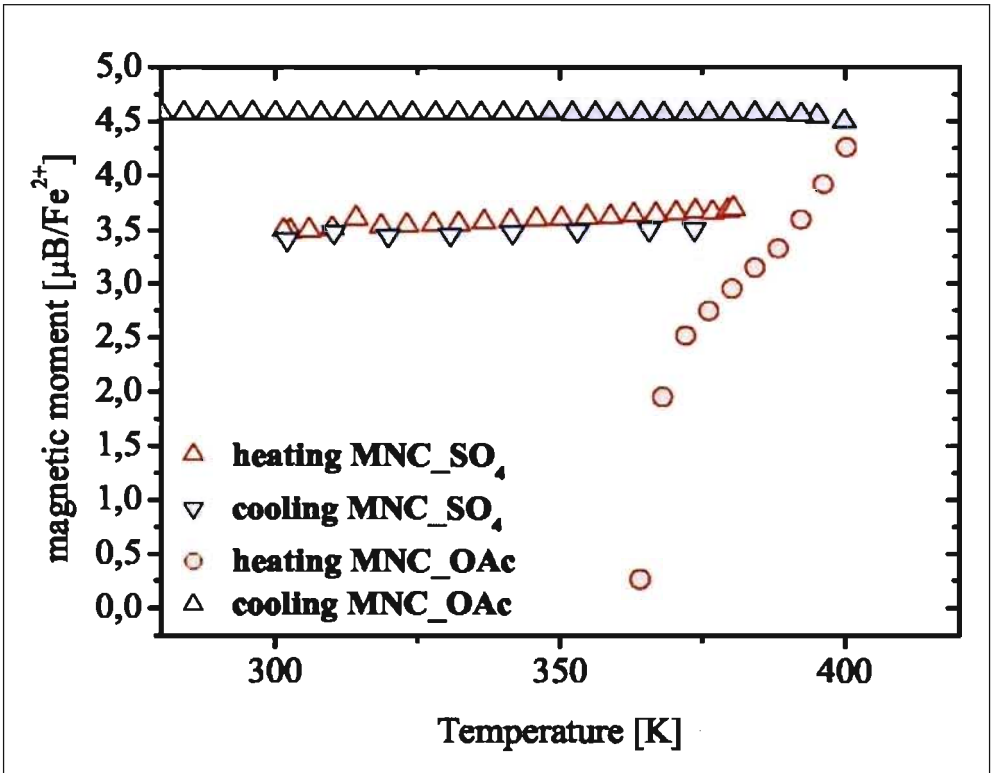

Figure 31. Magnetic susceptibility measurements for $Fe(ph\text{-}tpy)_2$ as acetate and as sulfate complex, carried out with a high temperature Faraday balance.

In the MNC_OAc, the spin transition is irreversible. That means, that the temperature driven deformation of the octahedral coordination geometry around

the metal, which leads to the spin transition, is not reversible and that the complex stays in a structure which is favoring the high-spin state. In the MNC_SO_4 complex, a ground magnetization is found and the magnetic moment shows that ¾ of the Fe(II) ions are already in the high-spin state. The measured magnetic moment is found to be around 3.5 μB/Fe(II). The highest spin-only contribution from Fe(II) is 4.9 μB/Fe(II) [72], spin coupling sometimes raises this value up to 5.3 μB/Fe(II) [72]. However, in the monometallic complexes there is no spin coupling expected, which leads to the assumption that about 74% of the Fe(II) ions exist in the high spin state. In this case, the measurement was not expanded to the DHP-complexes, because it was not expected to raise the last 20% of Fe(II) into the high spin state. In addition to that, it was already shown that the counter ion does have a strong effect on the spin state. The high-spin state leads to the assumption that the octahedral environment of the Fe(II) is already distorted by the SO_4^{2-} counter ions, which favors the high spin state. It seems that the SO_4^{2-} counter ions lead to a distorted octahedral coordination environment and therefore the high-spin state of the metal, so that we do not observe an irreversible spin-change as seen for the MNC_OAc complex. The same complex was also synthesized with PF_6 counter ions. Unfortunately, the measurement of this complex was disturbed by a malfunction of the Faraday

balance. However, a ground magnetization was found for this complex, commuting in between 1.5 – 2.0 μB.

3.3 MEPE with Flexible Spacer

In addition to the effect of the counter ion onto the monometallic complexes, we also wanted to evaluate the effect of the ligand spacer unit onto the spin transition of the MEPE. We wanted to see how the exchange of the stiff spacer by a flexible one, which leaves more degrees of freedom to the system, is affecting the spin transition. The tpy-opropo-tpy ligand (Figure 32) was synthesized to obtain the corresponding Fe(II) MEPE as well as the PAC's 1:4 and 1:6, where the 1:4 ratio contains 2 $[DHP]^-$ and 2 DHP-H, and the 1:6 ratio contains 2 $[DHP]^-$ and 4 DHP-H per MEPE unit.

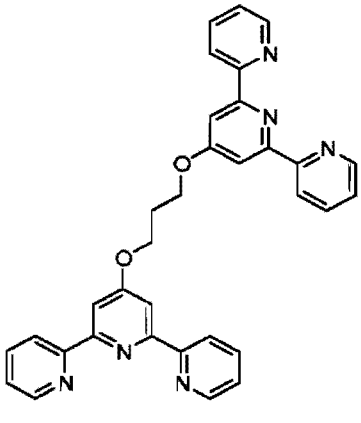

Figure 32. Structure of the propyl-spaced bis-terpyridine ligand (tpy-opropo-tpy).

3.3.1 Structural Analysis

To evaluate the stability of the structures before the magnetic measurements, TGA measurements have been carried out. The TGA curves for the MEPE and its PAC_6 are shown by Figure 33. The curve for PAC_4 is not shown, since its behavior is comparable to that of PAC_6.

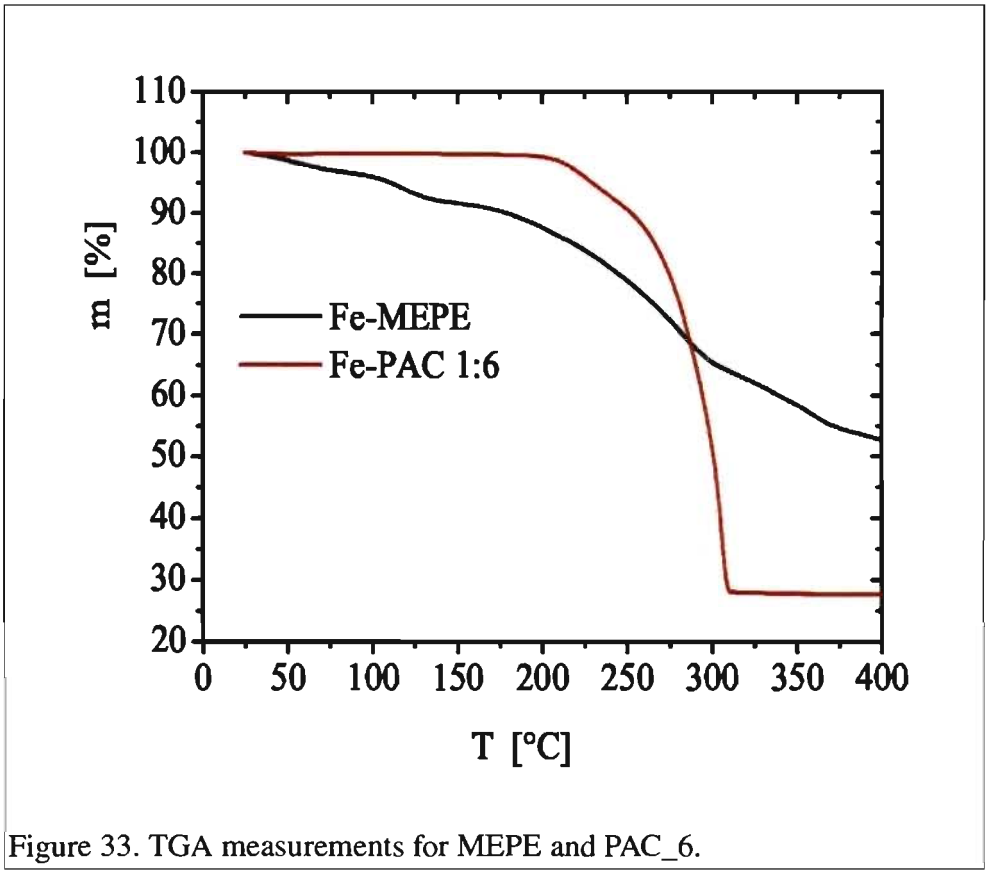

Figure 33. TGA measurements for MEPE and PAC_6.

The TGA measurements reveal that the MEPE itself is not stable; there is an important mass loss seen in the TGA starting already at 40 °C. However, the

PAC_4 and PAC_6 of this compound are stable up to 225 °C and could be analyzed in a high temperature Faraday balance.

Finally, the structures of PAC_4 and PAC_6 were structurally analyzed with SAXS measurements. The SAXS curves are shown by Figure 34.

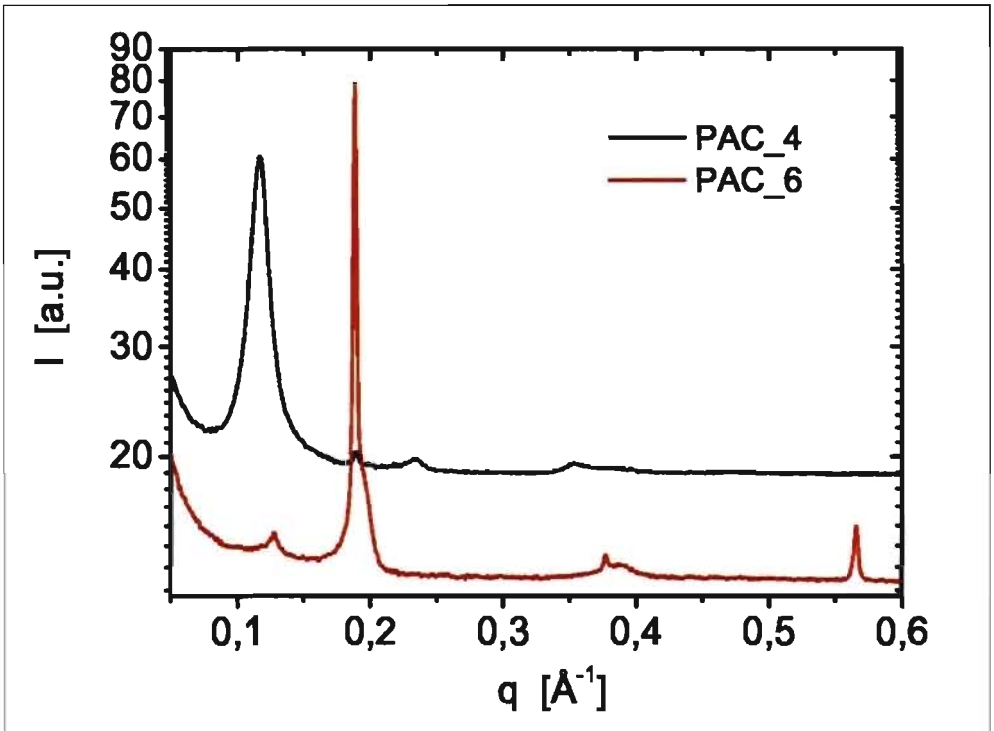

Figure 34. SAXS curves showing the log of the structural intensity against transfer momentum for PAC_4 and PAC_6.

PAC_4 structural data reveals as highest intensity peak the first order peak with two smaller equidistant scattering peaks. These peaks belong to the same lamellar structure which was found for MAC_2 and MAC_4, with a translational period of 53.6 Å, which corresponds to a double layer of the

amphiphile packaging with a hexagonal packing of the alkyl chains.[12, 68] The distance found here is almost identical to the value found for the MAC_4 and indicates the same partially interdigitated structure of the alkyl chains. Another first order peak with very low intensity is found, which corresponds to a mono layer with a translational period of 33.3 Å. No second or third order peaks are observed for this structure.

For the PAC_6, the opposite structural arrangement is observed. The peak data is shown by Table VI. There is a very low intensity first order peak with no equidistant peaks at 0.127 $Å^{-1}$, which belongs to a double layer. The second structure found is the mono layer. There are three equidistant peaks, the first order peak in a high intensity. These peaks correspond to the translational period of 49.3 Å for a mono layer. In opposition to the mononuclear complexes studied before, the higher amount of amphiphiles favors the arrangement of a mono layer instead of a double layer.

Table VI. SAXS data for compounds PAC_4 and PAC_6 giving the values for the reciprocal space, q , in $Å^{-1}$ and the distance of the layers, d, in Å.

compound	q/ $Å^{-1}$ (± 0.002 $Å^{-1}$)	order of the peak	d / Å (± 0.3 Å)
PAC_4	0.117	first order, structure 1	53.6
	0.235	second order, structure 1	
	0.353	third order, structure 1	
	0.188	first order, structure 2	33.3
PAC_6	0.127	first order, structure 1	49.3
	0.188	first order, structure 2	33.3
	0.378	second order, structure 2	
	0.566	third order, structure 2	

The peak-width analysis reveals a correlation length of coherent scattering for the bilayers of about 204 Å, corresponding to 4 bilayers for PAC_4, and 849 Å for the mono layers, corresponding to 25-26 mono layers, in PAC_6. The first order peak for the mono layered structure in PAC_4 and the first order peak for the double layered structure in PAC_6 are too small and broad for peak-width analysis.

3.3.2 Magnetic Properties

Figure 35 shows the magnetic susceptibility curves for the PAC_6. It shows a spin transition starting at 120 °C. However, this spin transition is a reversible

one. This probably means that the flexible propyl-spacer unit leaves more structural degrees of freedom, so that it is possible for the amphiphilic matrix that is embedding the MEPE to regain its former structure during the cooling process, which allows for a reversible spin transition.

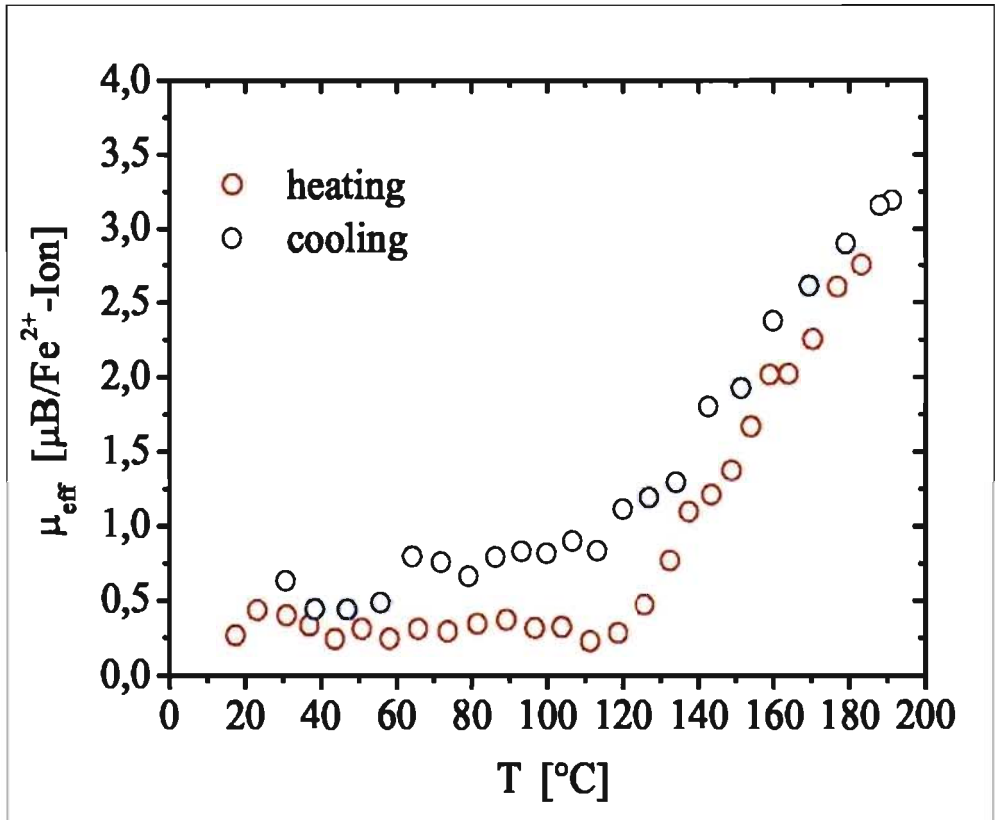

Figure 35. Magnetic susceptibility measurements for PAC_6, carried out with a high temperature Faraday balance.

As mentioned before, the spin transition results in a pronounced thermotropic effect with a change from bright violet to uncolored and could thus be used in potential applications in display or memory devices. [78] The violet color is due

to the $^1A_{1g} \rightarrow {}^1T_{1g}$ d-d transition. The images below show the color change of the PAC_6 from violet to clear upon the temperature dependent structural change to induce the spin transition (Figure 36).

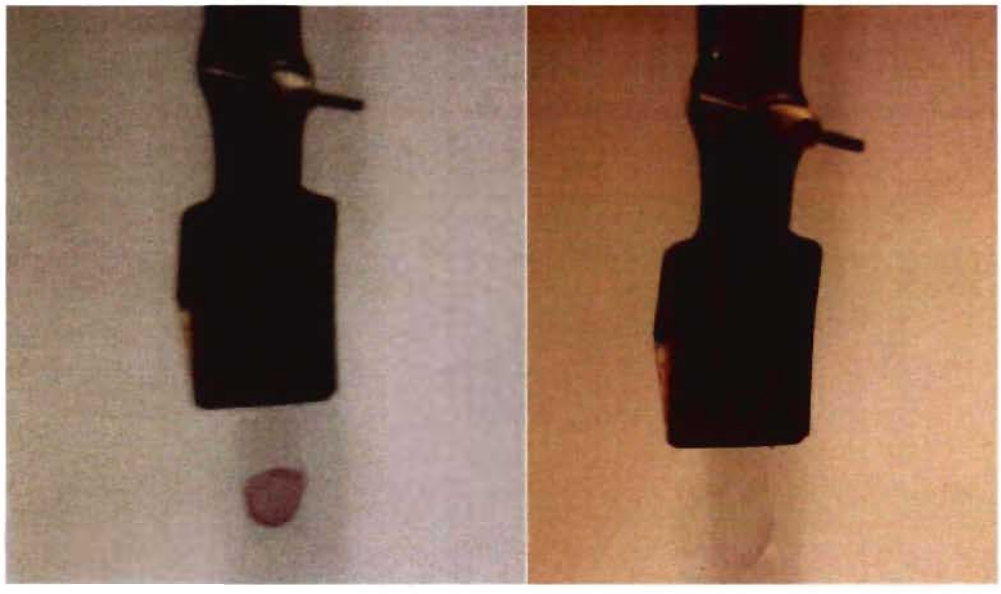

Figure 36. Left: The color of PAC_6 in low spin state. Right: The color of PAC_6 in high spin state.

3.4 Conclusion

The magnetic measurements of the complexes MNC_OAc, MAC_2 and MAC_4 showed, that these complexes adopt the same structure as their corresponding tpy-ph-tpy MEPE compounds. The melting of the amphiphiles induce a structural change in the amphiphilic matrix. The influence of this change on the coordination geometry of the complexes leads to a LS to HS

transfer. Without the structural change in the amphiphilic layers, the spin transition does not take place.

By observing the effect of the counter ion onto the spin transition, it was found that the $Fe(ph\text{-}tpy)_2(PF_6)_2$ and $Fe(ph\text{-}tpy)_2SO_4$ complexes do already have a ground magnetization. Therefor we conclude, that the SO_4^{2-} and PF_6^- counter ions probably lead to a distorted octahedral coordination environment and therefore to the high-spin state of the metal.

By observing the effect of a flexible spacer unit in the MEPE structures, we found that they show a similar behavior compared to the already known tpy-ph-tpy MEPEs. However, the flexible spacer unit leaves more structural degrees of freedom and this seems to allow for a reversible spin transition.

3.5 Experimental Section

Chemicals (reagent grade) were obtained from commercial suppliers and used without further purification. Solvents were used as received or dried over 4 Å molecular sieves. NMR spectra were recorded in CD_3CO_2D, $CDCl_3$ and D_2O at room temperature (r.t.) on a Bruker AV400 spectrometer at 400 MHz or Bruker

AV300 spectrometer at 300 MHz for ^{1}H NMR. Chemical shifts are reported in part per million (ppm) relative to residual solvent protons (CD_3CO_2D at 2.040 , $CDCl_3$ at 7.26, and D_2O at 4.8 ppm). Mass spectrometry was performed with ESI-MS Sciex Targa 600E MS/MS system. 4'-phenyl-2,2':6', 2''-terpyridine, 1,3-bis[4'-oxa (2,2':6',2''-terpyridinyl)]propane and its corresponding MEPE and PAC as well as the $[Fe(ph\text{-}tpy)_2](PF_6)_2$ were synthesized according to literature procedure [32, 79, 80].

Small angle X-ray scattering (SAXS) patterns are collected at the Energy Dispersive Reflectometer (EDR) at the BESSY II synchrotron in Berlin-Adlershof. Here, the hard X-ray decay of a bending magnet is used for scattering providing X rays in an energy range of 5 keV to 25 keV. Two energy-dispersive detectors with an energy resolution of $\Delta E / E = 10^{-2}$ were used; in addition to that a semi-conductor detector (Silena) was used to cover the wide angle area up to $q = 2$ Å^{-1} . The momentum transfer q is given by

$$q = \frac{2\pi E}{h \cdot c}(\sin\alpha_i + \sin\alpha_f) \quad \Rightarrow \quad q \simeq \Theta E \quad \text{when } \sin\alpha_i = \sin\alpha_f$$

$$\text{with } \sin\alpha_i = \text{incident angle}, \ \sin\alpha_f = \text{forwarded angle}$$

where in the latter equation the glancing angle (Θ) is given in radiants and the

energy in keV. To enhance the accessible q range the two energy-dispersive detectors are equipped at two fixed exit angles of $2\Theta = 2.79°$ and $2\Theta = 5.78°$ with respect to the incident beam. This geometry provides good counting statistics in a q range of $0.05\ Å^{-1} \leq q \leq 1.0\ Å^{-1}$. To increase the signal-to-noise ratio, an evacuated flight-tube is placed between the sample and the detectors.

Magnetic measurements for MNC_OAc and MAC_4 were performed with a superconducting quantum interference device (SQUID) from Quantum Design with a sensitivity of 10^{-7} emu and an applied field of 10 kOe. The samples were aligned with the surface parallel to the applied magnetic field.

The magnetic properties for MAC_2 were probed under Ar atmosphere by a home-made Faraday balance providing a sensitivity of 10^{-6} emu in an external field of B = 1.2 T. We used a heating rate of 2 K/min. In order to correct for the diamagnetic contribution, the molar susceptibility of the amphiphiles is measured leading to a value of $M = -6.0\ Å \pm 0.1\ 10^{-4}$ emu / mol while the susceptibility of the ligand is calculated from tabulated values $M = -3.5\ Å \pm 0.1\ 10^{-4}$ emu/mol.

1 (bis-(4'-phenyl-2, 2':6', 2''-terpyridine-N,N',N'')Iron(II), bis[acetate$^-$])

Metallic Fe (10.00 mg, 0.18 mmol) is dried under vacuum for 1 h, than 10 ml degassed glacial acetic acid are added and the mixture degassed again. The suspension is refluxed for 4 h until a clear, colorless solution is obtained. Phenylterpyridine (111 mg, 0.32 mmol) was added, followed by an immediate color change to dark violet. The solution is stirred for another 12 h and the solvent evaporated. The solid is washed with chloroform, redissolved in H_2O and vacuum dried. Yield: 138 mg (96%) ^{1}H NMR (400 MHz,) δ 11.41 (s, 4H), 10.84 (d, 4H, J = 8.0 Hz), 10.42 (d, 4H, J = 7.2 Hz), 9.99 (td, 4H, J = 1.4, 7.9 Hz), 9.82 (t, 4H, J = 7.4 Hz), 9.75 (t, 2H, J = 7.3 Hz), 9.42 (d, 4H, J = 5.0), 9.21 (dd, 4H, J = 3.7, 9.6), 4.69 (s, 6H). Anal. calcd. for $C_{46}H_{38}N_6O_4$: N, 10.58; C, 69.52; H, 4.82. Found: N, 10.50; C,69.49; H, 4.89

2 (bis (4'-phenyl-2, 2':6', 2''-terpyridine-N,N',N'')Iron(II))[DHP]$^-_2$

(Iron(II)-bis (4'-phenyl-2, 2':6', 2''-terpyridine-N,N',N''), bis[acetate$^-$]) (37 mg, 0.048 mmol) were added to a chloroform solution of DHP (52.52 mg, 0.096 mmol) and the suspension stirred for 3 h until a clear violet solution is obtained. The solvent is evaporated, the solid washed with H_20 and air-dried.

Anal. calcd. for $C_{106}H_{162}FeN_6O_4P_2$: N, 4.94; C, 74.79; H, 9.59. Found: N, 4.89; C, 74.82; H, 9.56.

3 (bis (4'-phenyl-2, 2':6', 2''-terpyridine-N,N',N'')Iron(II))[([DHP]$^-$)$_2$ (DHP-H)$_2$]

(Iron(II)-bis (4'-phenyl-2, 2':6', 2''-terpyridine-N,N',N''), bis[acetate$^-$]) (24.28 mg, 0.0306 mmol) was added to a chloroform solution of DHP (67.68 mg, 0.1225 mmol) and the suspension stirred for 3 h until a clear violet solution is obtained. The solution is filtered and the solvent is evaporated, the obtained solid washed with H_20 and air-dried. Anal. calcd. for $C_{170}H_{296}FeN_6O_8P_4$: N, 3.08; C, 74.61; H, 10.92. Found: N, 3.07; C, 74.82; H, 10.89.

4 (bis (4'-phenyl-2,2':6'2''-terpyridine-N,N',N'')Iron(II))[SO_4]

4'-phenyl-2,2':6', 2''-terpyridine (150mg, 0.49 mmol) were added together with $FeSO_4 \cdot 7\ H_2O$ (68.3 mg, 0.246 mmol) to ethanol (30 ml). The suspension was stirred for 4h, the solvent evaporated and the solid washed with chloroform and a minimal amount of cold water. Yield: 176 mg (80%) of a violet solid.

^{1}H NMR (400 MHz, D_2O) δ 9.25 (s, 4H), 8.61 (d, J = 8, 4H), 8.31 (d, J = 7, 4H), 7.88 (dt, J = 8, 15, 8H), 7.79 (d, J = 7, 2H), 7.26 (d, J = 5, 4H), 7.09 (t, J = 6, 4H). Anal. calcd. for $C_{42}H_{30}FeN_6O_4S$: N, 10.91; C, 65.46; H, 3.92. Found: N, 10.97; C, 65.51; H, 3.87.

4 First Steps to new Coordination Polymers

"The needs of the many outweigh the needs of the few, or the one"

John Stuart Mill

4.1 Synthesis of [bis (di-N-oxide-terpyridine)]

While terpyridine ligands are well suited for the formation of transition metal complexes, lanthanide ions have a preference to oxygen as binding atoms. Ln(III) organocomplexes, Eu and Tb especially, are used for fluorescent labels over conventional organic dyes as they have long emission lifetimes in the millisecond range under ambient conditions. Their signal can thus be easily distinguished from light scattering and short-lived (nanosecond range) fluorescence background [81]. Most importantly for us was their excellent solubility in aqueous solvents. We want to use water soluble systems as they do not provide hazardous solvent residues and are thus useful, for example, for industrial applications. The chemistry and applications of *N*-oxides have received much attention, since they are very useful synthetic intermediates [82, 83]. Heterocyclic N-oxides are also very useful oxidants, protecting groups,

auxiliary agents, ligands in metal complexes [84] and catalysts [82, 83].

The N-O moiety of the pyridine *N*-oxides can act effectively as both, an electron donor and an electron acceptor group. The contribution of the resonance forms I and II depends on the nature of other substituents on the pyridine ring (Figure 37) [85-87].

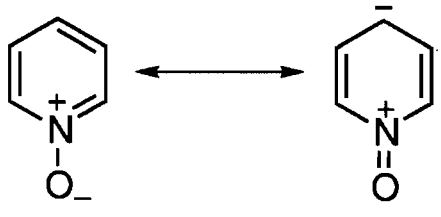

Figure 37. The two resonance forms of an *N*-oxide.

We want to study systems comparable to the terpyridine-based polymeric systems studied by our group, by replacing the transition metal ion by lanthanide ions, which do possess very interesting photo-physical properties.

However, in the case of lanthanide ions the terpyridine based systems do not form linear systems, as the lanthanide ion can bind up to 9 nitrogen atoms which leads to the formation of dendritic systems. Such a system would, for example, be obtained by the complexation of for example lanthanide ions like Eu^{3+} with an *N*-oxide analogue to the tpy-ph-tpy ligand (Figure 38).

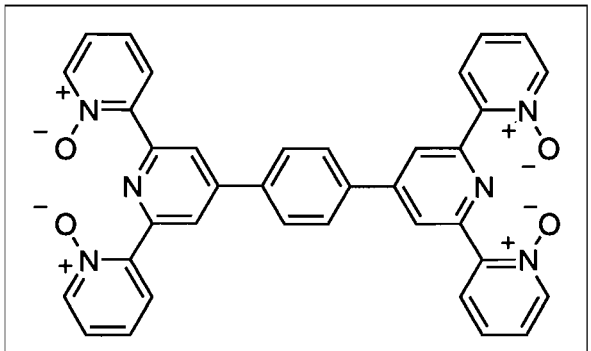

Figure 38. Bis-*N*-oxide ligand.

In case of complexation of 2 equivalents tris-*N*-oxide terpyridines with lanthanide ions, i.e. europium, the tris-*N*-oxide of terpyridine is known to lead to an eight coordinate geometry with one pendant pyridine-*N*-oxide donor, while a nine coordinate geometry is observed when the bis-*N*-oxide is used as ligand [88]. We wanted to use a bis-*N*-oxide ligand with only the two peripheral pyridines forming an *N*-oxide. Since the standard reaction procedure of reacting terpyridine with H_2O_2 leads to the formation of the tris-*N*-oxide, the bis-*N*-oxide was prepared by using 3-chloroperoxybenzoic acid, *m*-cpba. [89] The *N*-oxide-tpy-ph-tpy ligand was prepared by stirring 1 equivalent tpy-ph-tpy with 7.5 equivalents of *m*-cpba at room temperature for three days. It was then washed with an aqueous solution of Na_2CO_3 and purified by flash chromatography (Scheme 7).

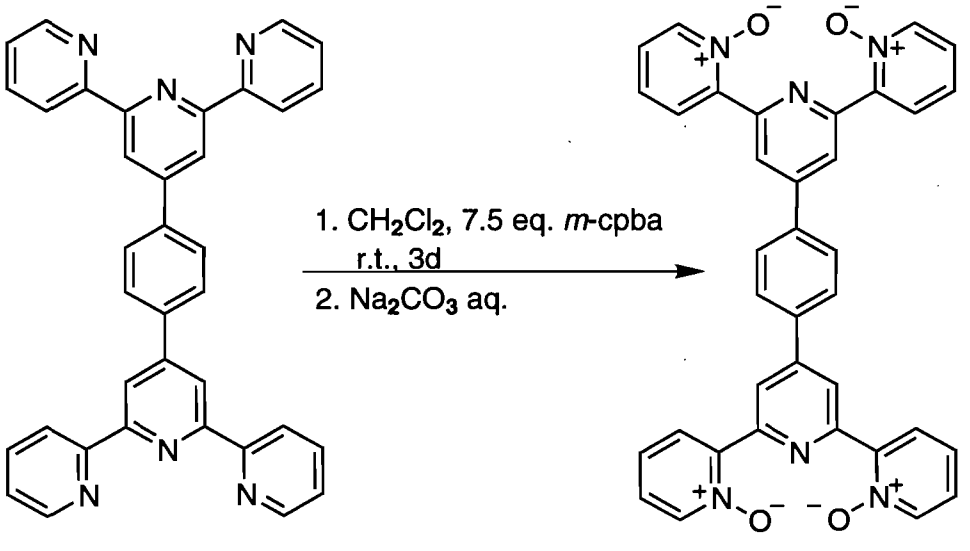

Scheme 7. Synthesis of the N-oxide analogue to the tpy-ph-tpy ligand.

The compound was characterized by ^{1}H NMR, mass spectrometry and elemental analysis. Due to its symmetry, there are only six signals in the ^{1}H NMR spectrum. The NMR assignment is shown by Figure 39.

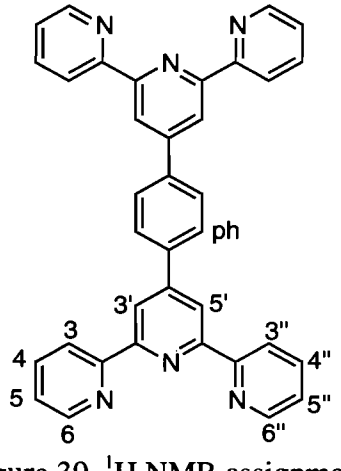

Figure 39. ^{1}H NMR assignment.

Table VII. ^{1}H NMR assignment for the bis-(tri-*N*-oxide) in comparison with the starting material tpy-ph-tpy.

	3, 3''	4, 4''	5, 5''	6, 6''	3', 5''	ph
tpy-ph-tpy	8.74	7.92	7.39	8.79	8.83	8.09
bis (di-*N*-oxide)	8.24	7.42	7.34	8.39	8.76	7.94

In comparison to the starting material, all the protons are shifted to higher field values, a behavior also observed for the bis-*N*-oxide of the terpyridine ligand itself [89].

This ligand can now be used to obtain polymeric systems with lanthanide ions. Usually, this kind of synthesis is successful by stirring the perchlorate salt of the metal ion together with the ligand in dry methanol [88]. It is now to be seen if this lanthanide ions do form polymeric systems with this ligand in the same way as it has already been seen for the different lanthanide ions with terpyridine ligands [90, 91].

4.2 Synthesis of [Pt(py-tpy)Cl]Cl, (2)

Luminescent polypyridine transition metal complexes are intensely studied due to their outstanding photophysical and redox properties [10], which makes them well-suited for the development of supramolecular systems for solar energy conversion [92, 93], information treatment [94, 95], and sensor technology [96-98]. Most of the studies concerning luminescent complexes was focused on d^6 transition metal complexes (e.g., Ru(II) and Os(II) species). Recently, d^8

transition metal complexes, in particular Pt(II)-polypyridine complexes, have attracted increasing attention as their square-planar geometry seems to have some advantages as compared to the octahedral transition metal complexes [99-104]. These square-planar complexes can oligomerize in solution, which leads to supramolecular architectures with increased photophysical properties as for example π-π interactions between the ligands or metal-to-metal electronic coupling interactions.

The ligand synthesis was performed using the standard condensation method shown by Scheme 8, and analytical data was according to literature [32]. The ligand was obtained as white solid in a yield of 38%.

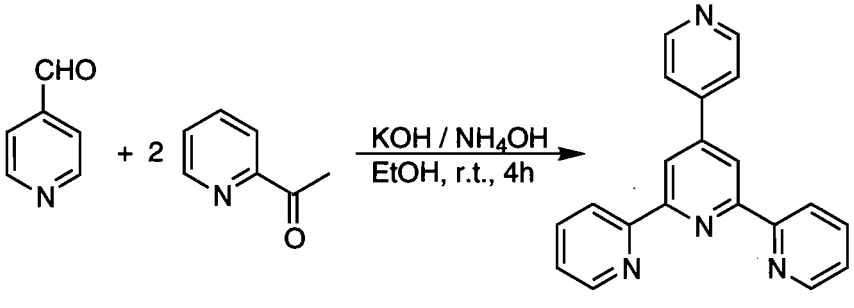

Scheme 8. Synthesis of the 4'-pyridyl-2,2":6',2"-terpyridine ligand.

The ligand was then reacted in an aqueous suspension with $Pt(COD)Cl_2$ to form the [Pt(py-tpy)Cl]Cl shown by Scheme 9.

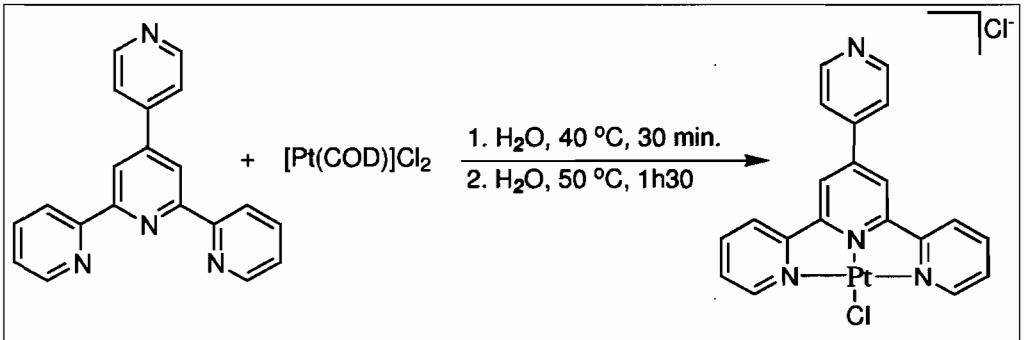

Scheme 9. Synthesis of the [Pt(py-tpy)Cl]Cl complex (**2**).

The formation of the insoluble Magnus salt, ($[Pt(py\text{-}tpy)Cl_2][PtCl_4]$), which is usually a problem occurring with $PtCl_2$ as starting material, was avoided by using the $Pt(COD)Cl_2$ as starting material [105]. The complex was obtained analytically pure as yellow solid and characterized by NMR, IR, elemental analysis and mass spectrometry. The yellow complex astonishingly turns red upon heating at higher temperatures in the solid form. Both forms, the red and the yellow one, retain their color in the solid state and in DMSO solution (Figure 40), but the red form returns to yellow when dissolved in water.

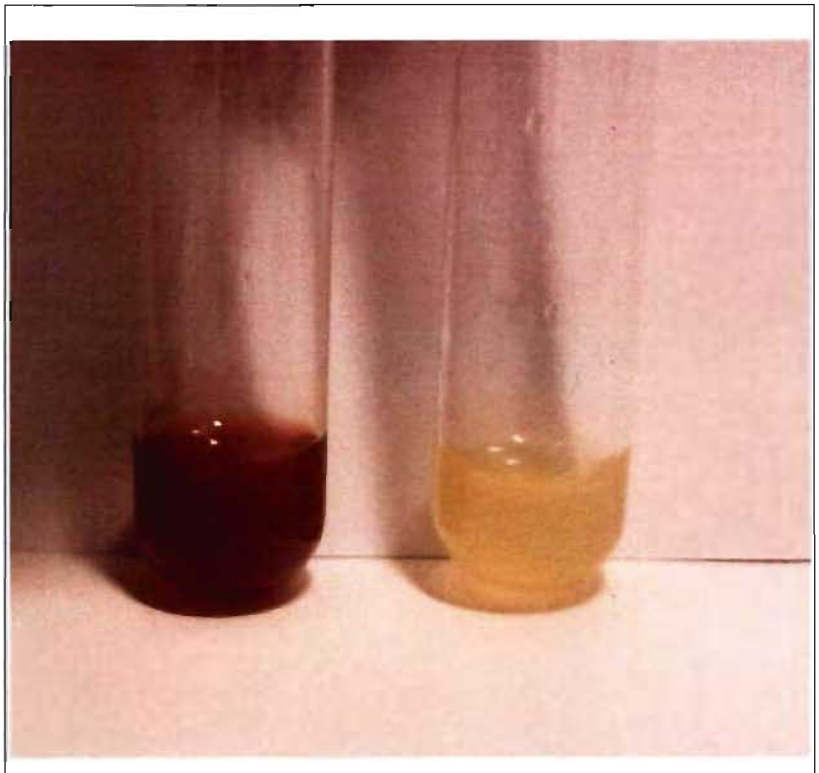

Figure 40. The red and the yellow form of the Pt-complex, at a concentration of 10^{-3} M in DMSO.

SPECTROSCOPIC PROPERTIES

Both forms of (**2**) were analyzed by 1H NMR and UV-vis spectroscopy. Figure 41 shows the UV-vis spectra of the yellow and the red form of the obtained platinum complex. Since the molar absorptivity of the red form is significantly lower than the one for the yellow complex, the spectrum for the red complex has been scaled in order to compare both spectra. Both species show a transition

around 400 nm, probably a d-d transition, and a transition around 300 nm probably due to a ligand transition. The red compound shows a peak in the MLCT region at 580 nm, while the yellow complex shows a transition at 354 nm which is not observed for the red form.

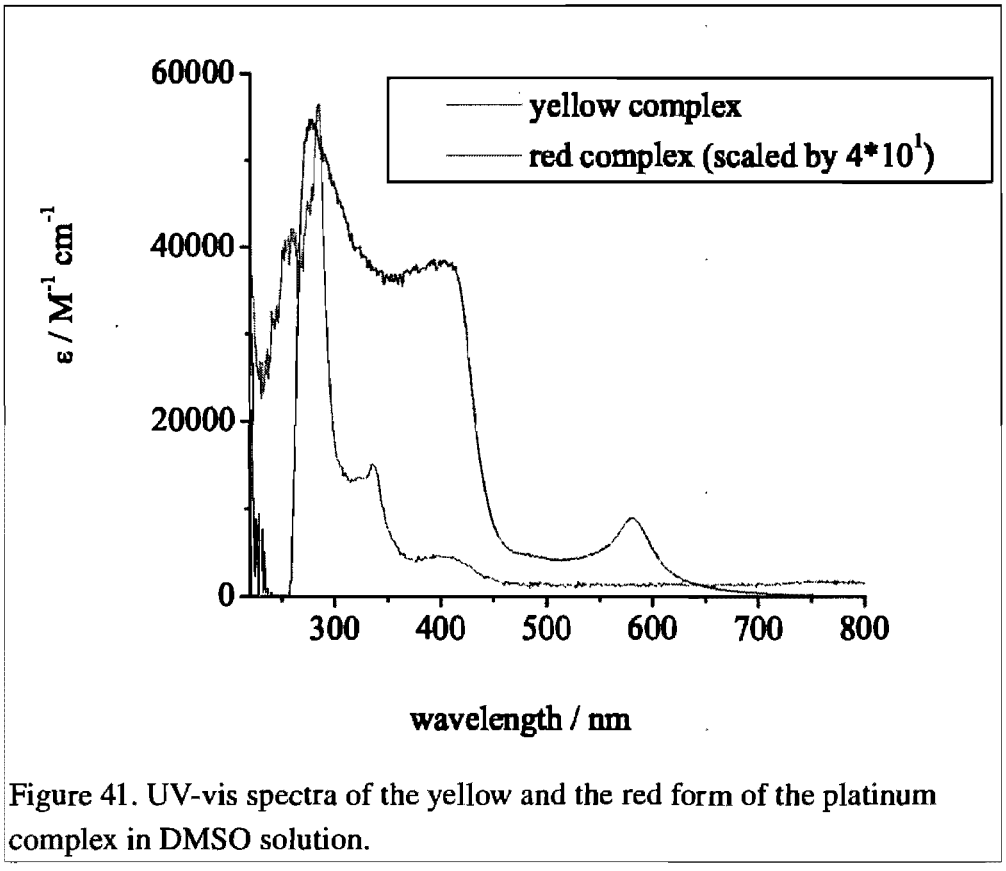

Figure 41. UV-vis spectra of the yellow and the red form of the platinum complex in DMSO solution.

Table VIII. UV-vis data for the yellow and red form of the [Pt(py-tpy)Cl]Cl complex.

compound	absorption λ_{max}, nm (ε, $M^{-1}cm^{-1}$)
yellow Pt-complex	398 (4560) 334 (15052) 284 (56464)
red Pt-complex	582 (220) 404 (952) 278 (1368)

In the beginning, I suspected that the yellow form is containing coordinated water, while the red one does not, which would explain the observed changes on heating and the reformation of the yellow complex in water. However, the elemental analysis data does not show water molecules to be present in the yellow complex. IR spectra were recorded for both compounds, but did not lead to additional information concerning the structural differences between the yellow and the red form of the platinum complex. In addition, it was observed that the yellow form in DMSO solution also turned red over several weeks, indicating that the red form is the thermodynamically more stable in DMSO solution. The 1H NMR spectrum of the red form shows additional aromatic peaks between 7.0 and 7.3 ppm as compared to the yellow one, while the rest of the spectrum is slightly down-field shifted (Figure 42).

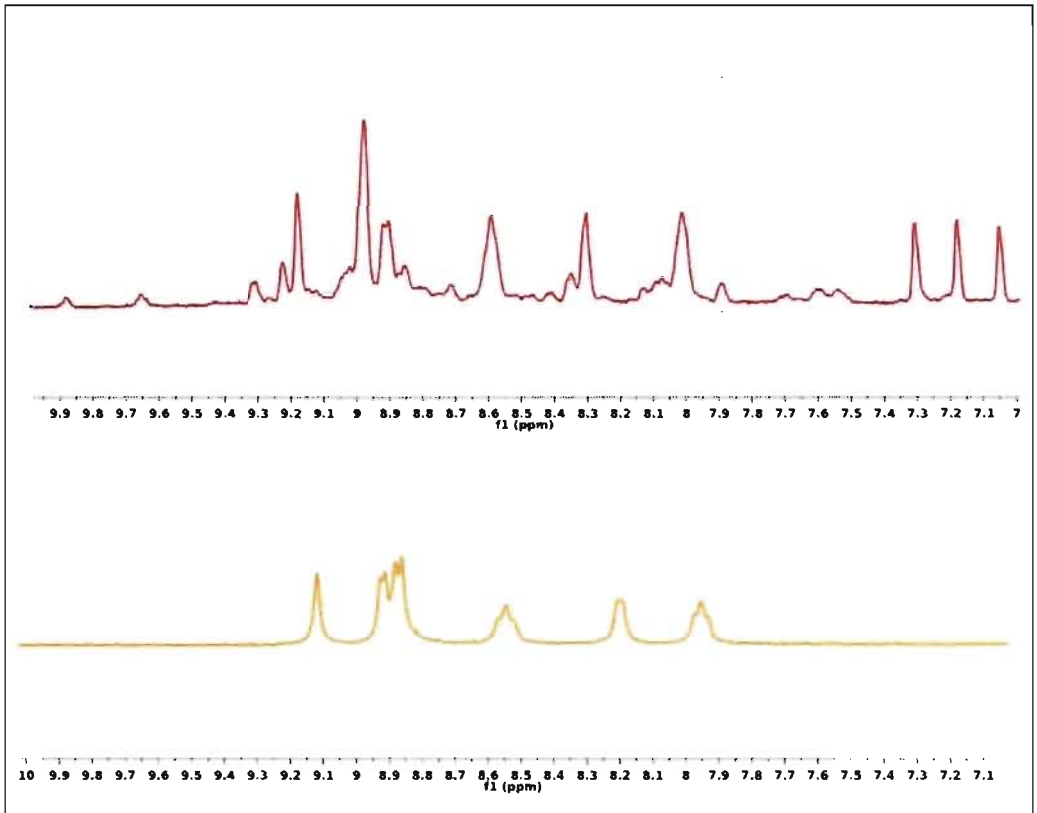

Figure 42. ^{1}H NMR spectra in DMSO-d_6. Top: the red form of (**2**). Bottom: yellow form of (**2**).

Another possible explanation is the de-coordination of one pyridine ring, which would result in an asymmetric coordination of the terpyridine ligand and explain the additional peaks in the NMR spectrum. In this case, the open coordination site might be occupied

- by an agostic H-coordination after 180° rotation of the de-coordinated pyridine

- by the chloride counterion forming a neutral complex.

- by the pyridine substituent of another complex.

The first possibility might explain the strong high-field shift of one proton, since the agostic proton might be more shielded, but this possibility seems overall rather unlikely, particularly in the presence of DMSO as a solvent. Re-coordination of chloride to form a neutral complex would rather lead to a hypsochromic shift in the UV-vis spectrum, while a bathochromic shift is observed (see Figure 2). The last possibility might also explain the high-field shift of one proton, due to the ring current from the bridging pyridine. This kind of coordination would result in oligometric or polymeric species. In order to get more information about the structure of this compound, a solution of the red form was spin coated on a Mica surface. The tapping-mode scanning force microscopy (SFM) picture obtained is shown by Figure 43.

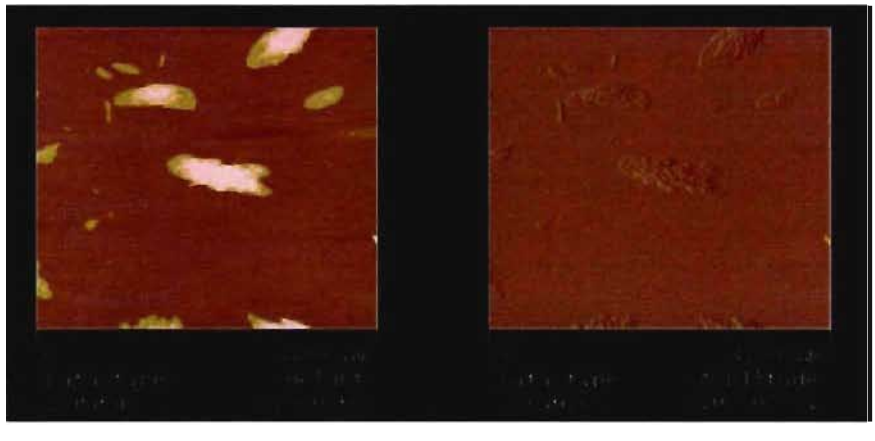

Figure 43. SFM pictures of a spin coated sample of the red form of the platinum complex.

The SFM pictures do show species that are long enough to be of oligomeric structure. However, their height and width are larger than that of a single molecule. This might be an oligomeric structure, but it can not be ruled out that this structures are only aggregates of mono-metallic complexes. Further studies need to be carried out with a purified sample of the red species, as for example analytical ultracentrifuge (AUC) measurements to determine its molecular weight.

Synthesis of $[Pt(py\text{-}tpy)]_n (OAc)_n$, (3)

The yellow form of the obtained Pt-complex can now be dechlorinated to form a coordination polymer with the fourth pyridine ring of the ligand, according to Scheme 10.

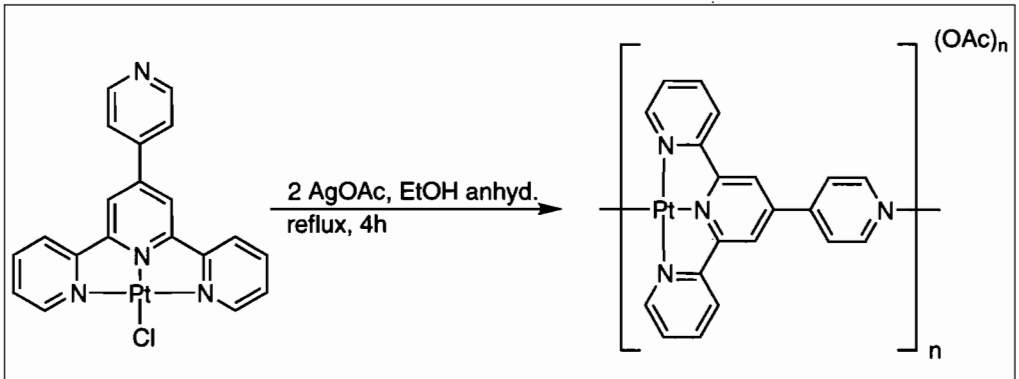

Scheme 10. Synthesis of the Pt coordination polymer.

The compound was obtained as orange solid and is soluble in MeOH, DMSO and H_2O. ^1H NMR spectra of the obtained solid do show what seems to be a mixture of two complexes, probably the acetate mono-metallic complex together with peaks that are broad enough to be obtained from a polymeric species. The color of the obtained species would correspond to a mixture of the red presumably oligomeric form together with the yellow starting material. However, the ^1H NMR peaks are not comparable to the ones encountered for the red species, so that a different species is formed here. In order to verify if there is a polymeric species contained in the mixture, tapping-mode SFM images have been taken from spin-coated samples of the platinum species (Figure 44).

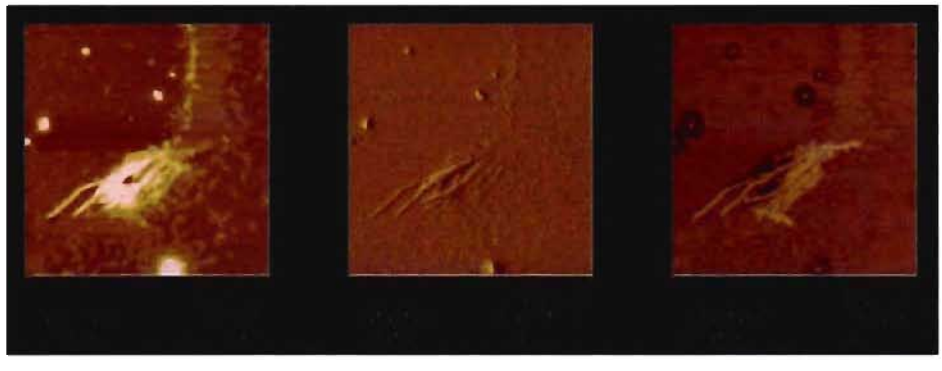

Figure 44. Preliminary SFM images from the polymeric Pt-species.

In these samples, a linear polymeric species is found. The samples were analyzed with the program Nanoscope V. 512b48. The height of the species was

calculated with this program by subtracting the background from the peak data. The amplitude measured from the SFM images is 11.6 Å, which corresponds to the calculated value of 11.2 Å of the molecules. The length of the rods is found to be up to 300 nm. The longer chains seem to accumulate; some of the amplitudes were found to be 24.5Å , which corresponds to two chains, or bigger. However, there are also structures observed that seem to accumulate in a spherical form (Figure 45) with the biggest ones having a radius of up to 160 nm.

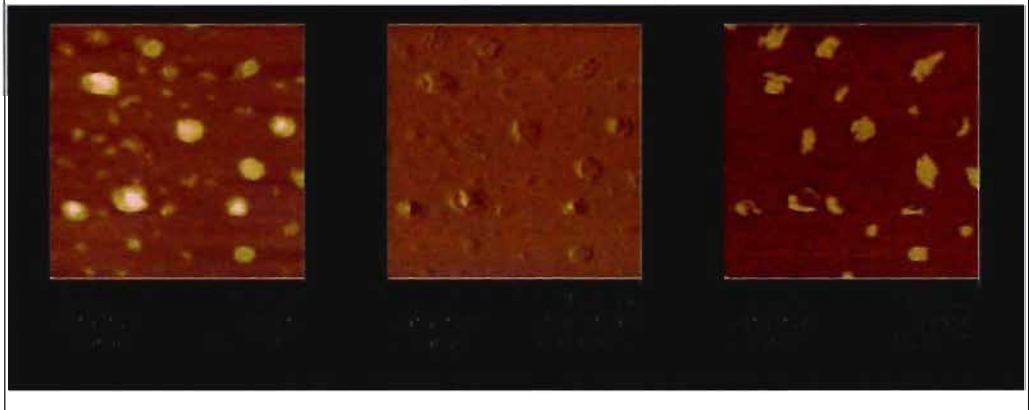

Figure 45. Preliminary SFM images showing spherical objects formed by the polymeric Pt-species.

These are probably corresponding to mononuclear and oligomeric structures, while the longer polymeric chains are forming rod like structures.

Once the polymer is obtained in pure form, further characterization of the

polymeric species, e.g. molecular weight determination, electro-chemistry and SAXS measurements are needed to obtain information about the compounds properties and structural arrangement.

4.3 Conclusion

A new *N*-oxide version of the tpy-ph-tpy ligand was synthesized and analyzed by ^{1}H NMR, mass spectrometry and elemental analysis. Bonding, structure and solubility in polar solvents of complexes with this ligand incorporating lanthanide ions, will be subject of the following work and could not be carried out in this time frame.

With the 4'-pyridylterpyridine ligand, a new platinum complex was obtained. It also was analyzed by the same techniques as the *N*-oxide ligand. This complex shows an unexpected color change when heated, from bright yellow to deep red. Further studies need to be carried out to determine the composition of the red species. With the platinum complex, the synthesis of a new coordination polymer was attempted. Even though the compound could not be obtained pure yet, SFM pictures do show the polymeric species.

4.4 Experimental Section

Chemicals (reagent grade) were obtained from commercial suppliers and used without further purification. Solvents were used as received or dried over 4 Å molecular sieves. 1,4-bis(2,2":6',2"-terpyridine-4'-yl)benzene [106] and 4'-pyridyl-2,2":6',2"-terpyridine [32] were synthesized according to published procedures.

Instrumentation

Nuclear magnetic resonance (NMR) spectra were recorded in $CDCl_3$, D_2O and $(CD_3)_2SO$ at room temperature (r.t.) on a Bruker AV400 spectrometer at 400 MHz or Bruker AV300 spectrometer at 300 MHz for ^1H NMR. Chemical shifts are reported in parts per million (ppm) relative to residual solvent protons (CD_3CO_2D 2.040 , $CDCl_3$ 7.26 and D_2O at 4.8 ppm). Mass spectrometry was performed with ESI-MS Sciex Targa 600E MS/MS system. The SFM samples were dried for 10 min at 40 °C before SFM investigations were carried out with a Nanoscope IIIa (Digital Instruments, Santa Barbara, CA) in tapping mode. An E-scanner over a range of scan lengths from 5 to 0.3 mm, and commercial Si cantilevers (length 125 mm and width 30 mm) with spring constants between 17

and 64 Nm^{-1} were used.

4'-[4-(1,1''-Dioxy-[2,2';6',2'']terpyridin-4'-yl)-phenyl]-1,1''-dioxy-[2,2';6',2'']terpyridine (1)

1,4-Bis(2,2":6',2"-terpyridine-4'-yl)benzene (110mg, 0.2 mmol) were dissolved in 5 ml DCM, than *m*-cpba (370 mg, 1.5 mmol) was added. After overnight stirring, 10 ml of DCM were added and the solution washed with 10% aqueous sodium carbonate. The solvent was evaporated and the obtained yellow solid purified with flash chromatography (silica, chloroform with methanol gradient from 1:1 – 1:2) . Yield: 104 mg (86%) of an off-white solid. ^1H NMR (400 MHz, $CDCl_3$) δ 9.28 (s, 4H), 8.39 (d, 4H, J = 6.1), 8.24 (d, 4H, J = 7.8), 7.98 (s, 4H), 7.42 (t, 4H, J = 7.8), 7.34 (t, 4H, J = 6.1). ESI-MS: *m/z* (%) = 605 (100) [M-H^+]. Anal. calcd. for $C_{36}H_{24}N_6O_4$: N, 13.9; C, 71.51; H, 4.00. Found: N, 13.87; C,71.54; H, 3.98

[Pt(py-tpy)Cl]Cl (2)

[Pt(COD)Cl_2] (150 mg, 0.4 mmol) was added to 5 ml H_2O to form a white suspension. Than 4'-pyridyl-2,2":6',2"-terpyridine (124 mg, 0.4 mmol) was

added and the reaction mix formed a beige suspension. The suspension was heated to 40°C and stirred for 30 min. During this time the reagents went gradually into solution, accompanied by a color change to yellow-greenish. H_2O (15 ml) were added to the suspension, the temperature was raised to 50°C and the reaction mix stirred for another 1h30. During this time the reaction mix gradually changed its color to bright yellow. The suspension was sonicated for 5 min., filtered and the aqueous phase was dried by evaporation. The yellow solid was then washed with chloroform. Yield: 104 mg (86%) of a yellow solid. ^1H NMR (300 MHz, DMSO) δ 9.12 (s, 2H), 8.86 (dd, 6Hz, 9Hz, 6H), 8.54 (dd, 6Hz, 9 Hz, 2H), 8.21 (tr, 6Hz, 2H), 7.94 (m, 2H). ESI-MS: *m/z* (%) = 541(100) [M^+]; Anal. calcd. for $C_{20}H_{14}C_{l2}N_4Pt$: N, 9.72; C, 41.68; H, 2.45. Found: N, 9.69; C, 41.76; H, 2.46. IR: yellow form: 3370, 3039, 1605, 1403, 786 cm^{-1}. Red form: 3442, 3268, 2248, 2121, 1622, 1034, 822, 758, 620 cm^{-1}.

$[Pt(py\text{-}tpy)]_n[OAc]_n$ (3)

[Pt(py-tpy)Cl]Cl (20 mg, 0.03 mol) was added together with AgOAc (10 mg, 0.06 mol) to 10 ml of ethanol. The orange solution was stirred for 1 h, during which time a grey precipitate formed. The reaction mix was filtered and dried under vacuum to give an orange solid.

A References

[1] Gaspar, A. B; Ksenofontov, V; Seredyuk, M; Gutlich, P. *Coord. Chem. Rev.*, **2005**, *249*, pp. 2661-2676.

[2] Lu, Z; Wang, X; Liu, Z; Liao, F; Gao, S; Xiong, R; Ma, H; Zhang, D. *Inorg. Chem.*, **2006**, *45*, pp. 999-1004.

[3] Goeb, S; De Nicola, A; Ziessel, R; Sabatini, C; Barbieri, A; Barigelletti, F. *Inorg. Chem.*, **2006**, *45*, pp. 1173-1183.

[4] Sutoh, K; Sasaki, S; Yoshifuji, M. *Inorg. Chem.*, **2006**, *45*, pp. 992-998.

[5] Yang, L; Zhang, Y; Yang, G; Chen, Q; Ma, J. S. *Dyes Pigments*, **2004**, *62*, pp. 27-33.

[6] Coe, B. J; Harries, J. L; Helliwell, M; Jones, L. A; Asselberghs, I; Clays, K; Brunschwig, B. S; Harris, J. A. *J. Am. Chem. Soc.*, **2006**, *128*, pp. 12192-12204.

[7] Tamayo, A; Casabo, J; Escriche, L; Lodeiro, C; Covelo, B; Brondino, C. D; Kivekas, R; Sillampaa, R. *Inorg. Chem.*, **2006**, *45*, pp. 1140-1149.

[8] Kurth, D. G; Higuchi, M. *Soft Matter*, **2006**, *2*, pp. 915-927.

[9] Friese, V. A; Kurth, D. G. *Coord. Chem. Rev.*, **2008**, *252*, pp. 199-211.

[10] Medlycott, E. A; Hanan, G. S. *Chem. Soc. Rev.*, **2005**, *34*, pp. 133-142.

[11] Schütte, M. Metallosupramolekulare polyelektrolytfilme, Mathematisch-Naturwissenschaftliche Fakultät der Universität Potsdam, **2000**, PhD. Thesis

[12] Bodenthin, Y; Pietsch, U; Mohwald, H; Kurth, D. G. *J. Am. Chem. Soc.*, **2005**, *127*, pp. 3110-3114.

[13] Nicholls, D. *Complexes and first-row transition elements*, ; : London, UK, 1995; .

[14] Constable, E. C; Baum, G; Bill, E; Dyson, R; van Eldik, R; Fenske, D; Kaderli, S; Morris, D. *Chem. Eur. J.*, **1999**, *5*, pp. 498-508.

[15] Rohit, Singh,; P, Nolan, Steven. *Annu. Rep. Prog. Chem., Sect. B: Org. Chem.*, **2006**, *102*, pp. 168-196.

[16] Jahnke, F Ekkehardt Hahn, Mareike C. *Angew. Chem. Int. Ed.*, **2008**, *47*, pp. 3122-3172.

[17] Lee, D; Kim, J; Jun, B; Kang, H; Park, J; Lee, Y. *Org. Lett.*, **2008**, *10*,

pp. 1609-1612.

[18] Gereon Altenhoff, Richard Goddard, Christian W Lehmann, Frank Glorius. *Angew. Chem. Int. Ed.*, **2003**, *42*, pp. 3690-3693.

[19] Son, S. U; Park, K. H; Lee, Y; Kim, B. Y; Choi, C. H; Lah, M. S; Jang, Y. H; Jang, D. *Inorg. Chem.*, **2004**, *43*, pp. 6896-6898.

[20] Maestri, M; Armaroli, N; Balzani, V; Constable, E. C; Thompson, A. M. W. C. *Inorg. Chem.*, **1995**, *34*, pp. 2759-2767.

[21] Polson, M. I. J; Taylor, N. J; Hanan, G. S. *Chem. Comm.*, **2002**, , pp. 1356-1357.

[22] Chen, J. C. C; Lin, I. J. B. *J. Organomet. Chem.* , **2000**, *19*, pp. 5113-5121.

[23] Medlycott, E. A; Schaper, F; Hanan, G. S. *Acta Cryst. Section E*, **2005**, *61*, p. m2311-m2313.

[24] Sauvage, J. P; Collin, J. P; Chambron, J. C; Guillerez, S; Coudret, C; Balzani, V; Barigelletti, F; De Cola, L. *Chem. Rev.*, **1994**, *94*, pp. 993-1019.

[25] Brueckner, R. *Reaktionsmechanismen*, 3rd Ed.; Elsevier, Spektrum, Akad. Verlag: Muenchen, 2004.

[26] Grundemann, S; Kovacevic, A; Albrecht, M; Faller, J. W; Crabtree, R. H. *J. Am. Chem. Soc.*, **2002**, *124*, pp. 10473-10481.

[27] McGuinness, D. S; Gibson, V. C; Steed, J. W. *Organomet.*, **2004**, *23*, pp. 6288-6292.

[28] Alder, R. W; Blake, M. E; Bortolotti, C; Bufali, S; Butts, C. P; Linehan, E; Oliva, J. M; Orpen, A. G. *Chem. Comm*, **1999**, pp. 241-242.

[29] Pyo, S; Perez-Cordero, E; Bott, S. G; Echegoyen, L. *Inorg. Chem.*, **1999**, *38*, p. 3337.

[30] Creutz, C; Chou, M; Netzel, T. L; Okumura, M; Sutin, N. *J. Am. Chem. Soc.*, **1980**, *102*, pp. 1309-1319.

[31] Discussion with Prof. Dr. Moehwald **2007**.

[32] Wang, J; Hanan, G. S. *Synlett*, **2005**, pp. 1251-1254.

[33] López, R; Moya, S. A; Zúñiga, C; Yáñez, M; Bayón, J. C; Aguirre, P. *Appl. Organomet. Chem.*, **2006**, *20*, pp. 315-321.

[34] Sheldrick, G. M. Program for Crystal Structure solution. University of Goettingen, Germany, 1986.

[35] Sheldrick, G. M. SADABS, Bruker Area Detector Absorption Corrections. Bruker AXS Inc., Madison, USA, 1996.

[36] Sheldrick, G. M. Program for Crystal Structure solution. University of Goettingen, Germany, SHELXS97 (1997a).

[37] Sheldrick, G. M. Program for crystal structure refinement. University of Goettingen, Germany, 1997.

[38] Heeger, A. J. *Angew. Chem. Int. Ed. Engl.*, **2001**, *40*, pp. 2591-2611.

[39] Marvel, C. S. *J. Chem. Ed.*, **1965**, *42(1)*, pp. 3-4.

[40] Kolomiets, E; Buhler, E; Candau, S. J; Lehn, J. *Macromolecules*, **2006**, *39*, pp. 1173-1181.

[41] Brunsveld, L; Folmer, B. J. B; Meijer, E. W. *MRS Bulletin*, **2000**, *25(4)*, pp. 49-53.

[42] Lehn, J. *Prog. Polym. Sci.*, **2005**, *30*, pp. 814-831.

[43] Lehn, J. *Chem. Eur. J.*, **1999**, *5*, pp. 2455-2463.

[44] Paulusse, J. M. J; Sijbesma, R. P. *Chem. Comm.*, **2003**, *13*, pp. 1494-1495.

[45] Manson, J. L; Kmety, C. R; Huang, Q; Lynn, J. W; Bendele, G. M; Pagola, S; Stephens, P. W; Liable-Sands, L. M. *Chem. Mater.*, **1998**, *10*, pp. 2552-2560.

[46] Lawandy, M. A; Huang, X; Wang, R; Li, J; Lu, J; Yuen, T; Lin, C. L. *Inorg. Chem.*, **1999**, *38*, pp. 5410-5414.

[47] Zhou, Y; Hong, M; Wu, X. *Chem. Comm.*, **2006**, , pp. 135-143.

[48] Duan L.-M.; Ye L.; Liu Y.-B.; Xie F.-T.; Yu J.-H.; Xu J.-Q.. *Pol. J. Chem.*, **2005**, *79(12)*, pp. 1835-2000.

[49] Dawe, L. N; Miglioi, J; Turnbow, L; Taliaferro, M. L; Shum, W. W; Bagnato, J. D; Zakharov, L. N; Rheingold, A. L. *Inorg. Chem.*, **2005**, *44*, pp. 7530-7539.

[50] Masciocchi, N; Galli, S; Sironi, A; Cariati, E; Galindo, M. A; Barea, E; Romero, M. A; Salas, J. M. *Inorg. Chem.*, **2006**, *45*, pp. 7612-7620.

[51] Cassoux, P; Valade, L; Kobayashi, H; Kobayashi, A; Clark, R. A; Underhill, A. E. *Coord. Chem. Rev.*, **1991**, *110*, pp. 115-160.

[52] Robertson, N; Cronin, L. *Coord. Chem. Rev.*, **2002**, *227*, pp. 93-127.

[53] Cerrada, E; Diaz, M. C; Diaz, C; Laguna, M; Sabater, A. *Syn. Met.*, **2001**, *119*, pp. 91-92.

[54] Singh, N; Prasad, A; Sinha, R. K. *Inorg. Chem. Comm.*, **2006**, *9*, pp. 1058-1062.

[55] Bidault, S; Viau, L; Maury, O; Brasselet, S; Zyss, J; Ishow, E; Nakatani,

K; Le Bozec, H. *Adv. Funct. Mat.*, **2006**, *16*, pp. 2252-2262.

[56] Li, S; Wu, J; Tian, Y; Ming, H; Wang, P; Jiang, M; Fun, H. *Eur. J. Inorg. Chem.*, **2006**, *2006*, pp. 2900-2907.

[57] Zhou, G; Lan, Y; Zheng, F; Zhang, X; Lin, M; Guo, G; Huang, J. *Chem. Phys. Lett.*, **2006**, *426*, pp. 341-344.

[58] Zhou, J; Chen, Q; Gu, Y; Mei, G; Yang, H. *Trans. Met. Chem. (Dordrecht, Netherlands)*, **2005**, *30*, pp. 1036-1041.

[59] Okubo, T; Kawajiri, R; Mitani, T; Shimoda, T. *J. Am. Chem. Soc.*, **2005**, *127*, pp. 17598-17599.

[60] Xie, Y; Zhao, H; Wang, X; Qu, Z,-R.; Xiong, R; Xue, X; Xue, Z; You, X. *Eur. J. Inorg. Chem.*, **2003**, *2003*, pp. 3712-3715.

[61] Chen, C; Suslick, K. S. *Coord. Chem. Rev.*, **1993**, *128*, pp. 293-322.

[62] Ye, Q; Wang, X; Zhao, H; Xiong, R. *Chem. Soc. Rev.*, **2005**, *34(3)*, pp. 208-225.

[63] Lehn, J. *Science*, **2002**, *295*, pp. 2400-2403.

[64] Haddon, R. C; Lamola, A. A. *PNAS*, **1985**, *82(7)*, pp. 1874-1878.

[65] Real, J. A; Bistability in iron(ii) spin-crossover systems: a supramolecular function. In *Perspectives In Supramolecular Chemistry - Transition Metals In Supramolecular Chemistry*, John Wiley & Sons Ltd: 1999, pp. 53-91.

[66] Kurth, D. G; Lehmann, P; Schutte, M. *PNAS*, **2000**, *97*, pp. 5704-5707.

[67] Knapp, R; Knapp, R; Kelch, S; Schmelz, O; Rehahn, M. *Macromol. Symp.*, **2003**, *204*, pp. 267-286.

[68] Kurth, D. G; Meister, A; Thünemann, A. F; Förster, G. *Langmuir*, **2003**, *19*, pp. 4055-4057.

[69] Ford-Smith, M. H; Sutin, N. *J. .Am. Chem. Soc.*, **1961**, *83*, pp. 1830-1834.

[70] Lippard, S. J. *Nature*, **2002**, *416*, pp. 587-587.

[71] Velten, U; Rehahn, M. *Chem. Comm. (Cambridge)*, **1996**, *23*, pp. 2639-2640.

[72] Lueken, H. *Magnetochemie. Eine Einfuehrung in Theorie und Anwendung*, Teubner Verlag: Stuttgart, 1999.

[73] Meister, A; Förster, G; Thünemann, A. F; Kurth, D. G. *ChemPhysChem*, **2003**, *4*, pp. 1095-1100.

[74] Hyperphysics: http://hyperphysics.phy-

astr.gsu.edu/hbase/solids/squid.html

[75] Class notes, "Physikalische Chemie", Prof. Motschmann, **2007**.

[76] Wang, R; Wang, Q; Li, L. *Polym. Int.*, **2003**, *52*, pp. 1820-1826.

[77] Bodenthin, Y; Pietsch, U; Grenzer, J; Geue, T; Moehwald, H; Kurth, D. G. *J. Phys. Chem.*, **2005**, *109*, pp. 12795 - 12799.

[78] Garcia, Y; Ksenofontov, V; Gütlich, P. *Hyperf. Interact.*, **2002**, *193-140*, pp. 543-551.

[79] Lehmann, P; Symietz, C; Brezesinski, G; Krass, H; Kurth, D. G. *Langmuir*, **2005**, *21*, pp. 5901-5906.

[80] Constable, E. C; Lewis, J; Liptrot, M. C; Raithby, P. R. *Inorg. Chim. Acta*, **1990**, *178*, pp. 47-54.

[81] Gudgin Dickson, E. F; Pollak, A; Diamandis, E. P. *J .Photochem. Photobiol. B.*, **1995**, *27*, pp. 3-19.

[82] Albini, A. *Synthesis*, **1993**, , pp. 263-277.

[83] Albini, A; Pietra, S. *Heterocyclic n-oxides*, CRC Press: Boca Raton, 1991.

[84] O'Conner, C. J; Sinn, E; Carlin, R. L. *Inorg. Chem.*, **1977**, *16*, pp. 3314-3320.

[85] Brycki, B; Nowak-Wydra, B; Szafran, M. *Mag. Res. Chem.*, **1988**, *26*, pp. 303-306.

[86] Chmurzynski, L; Liwo, A; Tempczyk, A. *Z. Naturforsch. B*, **1989**, *44b*, p. 1263.

[87] Mali, T. N; Hancock, R. D; Boeyens, J. C. A; Oosthuizen, E. L. *J. Chem. Soc., Perk. trans. 1*, **1991**, , pp. 1161 - 1163.

[88] Amoroso, A. J; Burrows, M. W; Haigh, R; Hatcher, M; Jones, M; Kynast, U; Abdul Malik, K. M; Sendor, D. *Dalton Trans.*, **2007**, pp. 1630-1638.

[89] Thummel, R. P; Jahng, Y. *J. Org. Chem.*, **1985**, *50*, pp. 3635-3636.

[90] Vermonden, T; de Vos, W. M; Marcelis, A. T. M; Sudhölter, E. J. R. *Eur. J. Inorg. Chem.*, **2004**, *2004*, pp. 2847-2852.

[91] Vermonden, T; van Steenbergen, M. J; Besseling, N. A. M; Marcelis, A. T. M; Hennink, W. E; Sudholter, E. J. R; Cohen Stuart, M. A. *J. Am. Chem. Soc.*, **2004**, *126*, pp. 15802-15808.

[92] O'Regan, B; Graetzel, M. *Nature*, **1991**, *353*, p. 737.

[93] Amadelli, R; Argazzi, R; Bignozzi, C. A; Scandola, F. *J. Am. Chem.*

Soc., **1990**, *112*.

[94] Goulle, V; Harriman, A; Lehn, J. *J. Chem. Soc., Chem. Commun.*, **1993**, p. 1034.

[95] Belser, P; Baak, M; Dux, R; De Cola, L; Balzani, V. *Angew. Chem., Int. Ed. Engl.*, **1995**, *34*, p. 595.

[96] Fabbrizzi, L; Licchelli, M; Pallavicini, P; Perotti, A; Taglietti, A; Sacchi, D. *Chem. Eur. J.*, **1996**, *67*, p. 3160.

[97] Di Marco, G; Lanza, M; Pieruccini, M; Campagna, S. *Adv. Mater.*, **1996**, *8*, p. 576.

[98] Kimura, E; Bu, X; Shionoya, M; Wada, S; Maruyama, S. *Inorg. Chem.* , **1992**, *31*, p. 4542.

[99] Smith, D. C; Miskowski, V. M; Mason, W. R; Gray, H. B. *J. Am. Chem. Soc.*, **1990**, *112*, p. 3759.

[100] Maestri, M; Balzani, V; Deuschel-Cornioley, C; von Zelewsky, A. *Adv. Photochem.*, **1992**, *17*, p. 1.

[101] Monsù Scolaro, L; Alibrandi, G; Romeo, R; Ricevuto, V; Campagna, S. *Inorg. Chem.*, **1992**, *31*, p. 2074.

[102] Rosace, G; Giuffrida, G; Saitta, M; Guglielmo, G; Campagna, S; Lanza, S. *Inorg. Chem.*, **1996**, *35*, p. 6816.

[103] Lippard, S. J; Bond, P. J; Wu, K. C; Bauer, W. R. *Science*, **1976**, *194*, pp. 726-727.

[104] Liu, H; Cheung, T; Peng, S; Che, C. *J. Chem. Soc., Chem. Commun.*, **1995**, p. 1787.

[105] Souchard, J; Wimmer, F. L; Ha, T. T. B; Johnson, N. P. *J. Chem. Soc. Dalton Trans.*, **1990**, p. 307.

[106] Winter, A; van den Berg, A. M; Hoogenboom, R; Kickelbick, G; Schubert, U. S. *Synthesis*, **2006**, pp. 2873-2878.

B Crystal Data

Table IX. Crystal data and details of the structure determination for $[\mathbf{1H^+}][\mathbf{PF_6}]$, $P2_1/c$, R = 0.03

Crystal Data	
Formula	C14 H15 N4, F6 P
Formula Weight	384.27
Crystal System	Monoclinic
Space group	$P2_1/c$, (No. 14)
a, b, c [Angstrom]	8.8907(1), 11.4813(1), 15.5497(2)
alpha, beta, gamma [deg]	90, 103.465(1), 90
V [Ang**3]	1543.63(3)
Z	4
D(calc) [g/cm**3]	1.653
Mu(CuKα) [/mm]	2.288
F(000)	784
Crystal Size [mm]	0.15 x 0.15 x 0.20
Data Collection	
Temperature (K)	150
Radiation [Angstrom]	CuKα, 1.54178
Theta Min-Max [Deg]	4.8, 69.0
Dataset	-10: 10 ; -13: 13 ; -18: 18
Tot., Uniq. Data, R(int)	20975, 847, 0.027
Observed data [I > 2.0 sigma(I)]	2752
Refinement	
Nref, Npar	2847, 227
R, wR2, S	0.0307, 0.0802, 1.04
w = 1/[\s^2^(Fo^2^)+(0.0463P)^2^+0.5732P], where P=(Fo^2^+2Fc^2^)/3	
Max. and Av. Shift/Error	0.00, 0.00
Min. and Max. Resd. Dens. [e/Ang^3]	-0.34, 0.20

Table X. Final coordinates and equivalent isotropic displacement parameters of the non-hydrogen atoms for **[1H$^+$][PF$_6$]**, $P2_1/c$, R = 0.03. U(eq) = 1/3 of the trace of the orthogonalized U tensor.

Atom	x	y	z	U(eq)[Ang^2]
N1	0.98501(12)	0.34848(10)	0.51872(7)	0.0271(3)
N2	0.85348(12)	0.20802(9)	0.42024(7)	0.0220(3)
N3	0.58994(12)	0.23854(9)	0.36149(7)	0.0212(3)
N4	0.48730(12)	0.41417(10)	0.39813(7)	0.0272(3)
C1	1.11635(16)	0.39117(13)	0.56917(9)	0.0319(4)
C2	1.26001(16)	0.34070(13)	0.57511(9)	0.0350(4)
C3	1.26867(16)	0.24204(13)	0.52580(10)	0.0347(4)
C4	1.13489(15)	0.19653(12)	0.47270(9)	0.0294(4)
C5	0.99671(14)	0.25293(11)	0.47284(8)	0.0232(3)
C6	0.85070(15)	0.08944(11)	0.38297(9)	0.0276(4)
C7	0.68870(15)	0.04110(11)	0.36814(9)	0.0279(4)
C8	0.57226(15)	0.12519(10)	0.31551(9)	0.0258(4)
C9	0.45927(14)	0.31531(11)	0.35319(8)	0.0223(3)
C10	0.31566(15)	0.28497(12)	0.30133(9)	0.0299(4)
C11	0.19457(16)	0.36197(14)	0.29813(10)	0.0355(4)
C12	0.22014(16)	0.46489(13)	0.34507(9)	0.0331(4)
C13	0.36812(16)	0.48721(12)	0.39371(9)	0.0305(4)
C14	0.72658(14)	0.27106(11)	0.40883(8)	0.0212(3)
P1	0.73820(4)	0.12334(3)	0.65300(2)	0.0241(1)
F11	0.66817(10)	0.21529(8)	0.57740(6)	0.0437(3)
F12	0.58774(10)	0.13667(8)	0.69174(6)	0.0419(3)
F13	0.65575(10)	0.02026(8)	0.59024(6)	0.0422(3)
F14	0.88823(9)	0.10967(8)	0.61364(6)	0.0378(3)
F15	0.82038(10)	0.22636(8)	0.71570(6)	0.0451(3)
F16	0.80825(13)	0.03051(10)	0.72796(7)	0.0556(3)

Table XI. Hydrogen atom positions and isotropic displacement parameters for hydrogen atom positions and isotropic displacement parameters for **[1H$^+$][PF$_6$]**, $P2_1/c$, R = 0.03.

Atom	x	y	z	U(iso), [Ang^2]
H1	1.11080	0.45960	0.60260	0.0380
H2	1.35040	0.37320	0.61220	0.0420
H3	1.36560	0.20570	0.52830	0.0420
H4	1.13740	0.12930	0.43750	0.0350
H6A	0.92370	0.03860	0.42430	0.0330
H6B	0.88310	0.09200	0.32620	0.0330
H7A	0.68280	-0.03380	0.33600	0.0330
H7B	0.66370	0.02610	0.42590	0.0330
H8A	0.58990	0.13440	0.25530	0.0310
H8B	0.46620	0.09500	0.31010	0.0310
H10	0.30090	0.21390	0.26910	0.0360
H11	0.09420	0.34400	0.26370	0.0430
H12	0.13850	0.51870	0.34400	0.0400
H13	0.38650	0.55820	0.42580	0.0370
H14	0.73400	0.34520	0.43660	0.0250

==========

The temperature factor has the form of Exp(-T), where
T = 8*(Pi**2)*U*(Sin(Theta)/Lambda)**2 for isotropic atoms.

Table XII. (An)isotropic displacement parameters for **[1H$^+$][PF$_6$]**, $P2_1/c$, R = 0.03.

Atom	U(1,1) or U	U(2,2)	U(3,3)	U(2,3)	U(1,3)	U(1,2)
N1	0.0239(6)	0.0269(6)	0.0293(6)	0.0009(4)	0.0035(4)	-0.0019(4)
N2	0.0206(5)	0.0225(5)	0.0225(5)	0.0008(4)	0.0045(4)	0.0019(4)
N3	0.0204(5)	0.0214(5)	0.0214(5)	0.0003(4)	0.0040(4)	0.0001(4)
N4	0.0247(5)	0.0274(6)	0.0288(6)	-0.0006(4)	0.0048(4)	0.0037(4)

C1	0.0299(7)	0.0325(7)	0.0305(7)	0.0022(5)	0.0012(6)	-0.0071(6)
C2	0.0238(7)	0.0436(8)	0.0335(7)	0.0124(6)	-0.0018(6)	-0.0080(6)
C3	0.0211(6)	0.0419(8)	0.0401(8)	0.0154(6)	0.0052(6)	0.0033(6)
C4	0.0237(6)	0.0320(7)	0.0331(7)	0.0070(6)	0.0076(5)	0.0043(5)
C5	0.0207(6)	0.0254(6)	0.0230(6)	0.0062(5)	0.0038(5)	-0.0002(5)
C6	0.0283(7)	0.0235(6)	0.0305(7)	-0.0023(5)	0.0061(5)	0.0046(5)
C7	0.0303(7)	0.0210(6)	0.0323(7)	-0.0014(5)	0.0070(5)	0.0002(5)
C8	0.0267(7)	0.0224(6)	0.0274(7)	-0.0036(5)	0.0047(5)	-0.0032(5)
C9	0.0208(6)	0.0263(6)	0.0203(6)	0.0042(5)	0.0060(5)	0.0017(5)
C10	0.0251(7)	0.0338(7)	0.0285(7)	0.0007(5)	0.0018(5)	-0.0010(5)
C11	0.0210(7)	0.0478(9)	0.0352(7)	0.0079(6)	0.0014(6)	0.0025(6)
C12	0.0266(7)	0.0413(8)	0.0329(7)	0.0097(6)	0.0102(5)	0.0113(6)
C13	0.0306(7)	0.0307(7)	0.0312(7)	0.0017(5)	0.0091(6)	0.0078(5)
C14	0.0215(6)	0.0217(6)	0.0205(6)	0.0018(4)	0.0049(5)	0.0004(5)
P1	0.0220(2)	0.0264(2)	0.0240(2)	-0.0011(1)	0.0054(1)	-0.0003(1)
F11	0.0374(5)	0.0463(5)	0.0464(5)	0.0151(4)	0.0075(4)	0.0111(4)
F12	0.0329(5)	0.0563(6)	0.0416(5)	-0.0177(4)	0.0192(4)	-0.0114(4)
F13	0.0434(5)	0.0433(5)	0.0431(5)	-0.0177(4)	0.0167(4)	-0.0125(4)
F14	0.0276(4)	0.0407(5)	0.0486(5)	-0.0001(4)	0.0158(4)	0.0043(3)
F15	0.0340(5)	0.0489(6)	0.0515(5)	-0.0211(4)	0.0084(4)	-0.0109(4)
F16	0.0615(6)	0.0567(6)	0.0446(5)	0.0234(5)	0.0045(5)	0.0050(5)

==========

The temperature factor has the form of Exp(-T), where

T = 8*(Pi**2)*U*(Sin(Theta)/Lambda)**2 or isotropic Atoms, where

T = 2*(Pi**2)*Sumij(h(i)*h(j)*U(i,j)*Astar(i)*Astar(j)), for anisotropic atoms.

Astar(i) are reciprocal axial lengths and h(i) are the reflection indices.

Table XIII. Bond distances (Å) for $[\mathbf{1H^+}][\mathbf{PF_6}]$, $P2_1/c$, R = 0.03.

P1	-F14	1.5996(9)	C7	-C8	1.5096(18)
P1	-F15	1.5974(10)	C9	-C10	1.3865(19)
P1	-F16	1.5951(12)	C10	-C11	1.385(2)
P1	-F13	1.5991(10)	C11	-C12	1.380(2)
P1	-F11	1.5948(10)	C12	-C13	1.380(2)
P1	-F12	1.5972(10)	C1	-H1	0.9500
N1	-C1	1.3389(18)	C2	-H2	0.9500
N1	-C5	1.3258(17)	C3	-H3	0.9500
N2	-C6	1.4776(16)	C4	-H4	0.9500
N2	-C5	1.4392(17)	C6	-H6B	0.9900
N2	-C14	1.3172(17)	C6	-H6A	0.9900
N3	-C8	1.4755(16)	C7	-H7B	0.9900
N3	-C9	1.4399(17)	C7	-H7A	0.9900
N3	-C14	1.3193(17)	C8	-H8A	0.9900
N4	-C9	1.3258(17)	C8	-H8B	0.9900
N4	-C13	1.3404(18)	C10	-H10	0.9500
C1	-C2	1.386(2)	C11	-H11	0.9500
C2	-C3	1.380(2)	C12	-H12	0.9500
C3	-C4	1.383(2)	C13	-H13	0.9500
C4	-C5	1.3892(19)	C14	-H14	0.9500
C6	-C7	1.5103(19)			

Table XIV. Bond angles (°) for $[\mathbf{1H^+}][\mathbf{PF_6}]$, $P2_1/c$ R = 0.03.

F11	-P1	-F16	179.49(6)	N1	-C5	-C4	124.52(12)
F12	-P1	-F13	89.77(5)	N2	-C5	-C4	119.86(11)
F12	-P1	-F14	179.64(5)	N2	-C6	-C7	109.07(11)
F12	-P1	-F15	90.18(5)	C6	-C7	-C8	110.91(11)
F12	-P1	-F16	90.41(6)	N3	-C8	-C7	108.61(11)
F13	-P1	-F14	89.91(5)	N3	-C9	-N4	115.35(11)

F13	-P1	-F15	179.94(6)	N3	-C9	-C10	120.85(11)
F13	-P1	-F16	89.83(5)	N4	-C9	-C10	123.80(12)
F14	-P1	-F15	90.15(5)	C9	-C10	-C11	117.61(13)
F14	-P1	-F16	89.75(6)	C10	-C11	-C12	119.79(13)
F15	-P1	-F16	90.20(5)	C11	-C12	-C13	117.87(13)
F11	-P1	-F13	89.73(5)	N4	-C13	-C12	123.58(13)
F11	-P1	-F14	90.01(5)	N2	-C14	-N3	124.62(12)
F11	-P1	-F12	89.83(5)	N1	-C1	-H1	118.00
F11	-P1	-F15	90.25(5)	C2	-C1	-H1	118.00
C1	-N1	-C5	116.82(12)	C1	-C2	-H2	121.00
C5	-N2	-C14	119.77(11)	C3	-C2	-H2	121.00
C5	-N2	-C6	119.00(10)	C2	-C3	-H3	120.00
C6	-N2	-C14	121.19(11)	C4	-C3	-H3	120.00
C8	-N3	-C9	120.25(10)	C5	-C4	-H4	121.00
C8	-N3	-C14	120.02(11)	C3	-C4	-H4	121.00
C9	-N3	-C14	119.71(11)	N2	-C6	-H6A	110.00
C9	-N4	-C13	117.34(11)	C7	-C6	-H6B	110.00
N1	-C1	-C2	123.40(13)	N2	-C6	-H6B	110.00
C1	-C2	-C3	118.42(13)	C7	-C6	-H6A	110.00
C2	-C3	-C4	119.37(13)	H6A	-C6	-H6B	108.00
C3	-C4	-C5	117.45(13)	H7A	-C7	-H7B	108.00
N1	-C5	-N2	115.62(11)	C6	-C7	-H7A	109.00
C6	-C7	-H7B	109.00	C11	-C10	-H10	121.00
C8	-C7	-H7A	109.00	C10	-C11	-H11	120.00
C8	-C7	-H7B	109.00	C12	-C11	-H11	120.00
N3	-C8	-H8A	110.00	C11	-C12	-H12	121.00
N3	-C8	-H8B	110.00	C13	-C12	-H12	121.00
C7	-C8	-H8A	110.00	N4	-C13	-H13	118.00
C7	-C8	-H8B	110.00	C12	-C13	-H13	118.00
H8A	-C8	-H8B	108.00	N2	-C14	-H14	118.00
C9	-C10	-H10	121.00	N3	-C14	-H14	118.00

Table XV. Crystal data and details of the structure determination for **2**, $P2_1/c$ R = 0.03.

Crystal Data	
Formula	C28 H28 N8 Ru, 2(F6 P), C2 H3 N
Formula Weight	908.65
Crystal System	Monoclinic
Space group	$P2_1/c$ (No.14)
a, b, c [Angstrom]	8.6113(1) 8.9270(1) 46.1772(7)
alpha, beta, gamma [deg]	90 93.415(1) 90
V [Ang**3]	3543.48(8)
Z	4
D(calc) [g/cm**3]	1.703
Mu(CuKα) [/mm]	5.363
F(000)	1824
Crystal Size [mm]	0.08 x 0.16 x 0.22
Data Collection	
Temperature (K)	150
Radiation [Angstrom]	CuKα 1.54178
Theta Min-Max [Deg]	1.9, 69.0
Dataset	-10:10; -10:9; -55:55
Tot., Uniq. Data, R(int)	48525, 6530, 0.029
Observed data [I > 2.0 sigma(I)]	5958
Refinement	
6530, 525Nref, Npar	6530, 525Nref, Npar
R, wR2, S	0.0300, 0.0835, 1.06
w = 1/[\s^2^(Fo^2^)+(0.0496P)^2^+2.5054P], where P=(Fo^2^+2Fc^2^)/3	
Max. and Av. Shift/Error	0.00, 0.00
Min. and Max. Resd. Dens. [e/Ang^3]	-0.50, 0.97

Table XVI. Final coordinates and equivalent isotropic displacement parameters of the non-hydrogen atoms for **2**, $P2_1/c$, R = 0.03. U(eq) = 1/3 of the trace of the orthogonalized U tensor starred atom sites have a S.O.F less than 1.0.

Atom	x	y	z	U(eq), [Ang^2]
Ru1	0.69239(2)	0.01526(2)	0.36399(1)	0.0208(1)
N1	0.6076(2)	-0.2020(2)	0.36793(4)	0.0245(6)
N2	0.6376(2)	-0.1411(2)	0.41707(4)	0.0271(6)
N3	0.7446(2)	0.0974(2)	0.42443(4)	0.0278(6)
N4	0.7841(2)	0.2169(2)	0.38059(4)	0.0242(6)
N5	0.9086(2)	-0.0668(2)	0.35300(4)	0.0252(6)
N6	0.8095(3)	0.0005(2)	0.30666(5)	0.0284(7)
N7	0.5589(2)	0.1016(2)	0.30763(4)	0.0298(6)
N8	0.4724(2)	0.1074(2)	0.35447(4)	0.0259(6)
C1	0.5701(3)	-0.2997(3)	0.34637(6)	0.0307(8)
C2	0.5113(3)	-0.4398(3)	0.35149(7)	0.0396(9)
C3	0.4913(3)	-0.4826(3)	0.37988(8)	0.0427(9)
C4	0.5323(3)	-0.3865(3)	0.40230(6)	0.0360(8)
C5	0.5913(3)	-0.2463(3)	0.39584(5)	0.0278(7)
C6	0.6367(3)	-0.1719(3)	0.44847(5)	0.0352(8)
C7	0.6228(4)	-0.0246(3)	0.46428(6)	0.0390(9)
C8	0.7458(3)	0.0873(3)	0.45630(5)	0.0363(8)
C9	0.7999(3)	0.2230(3)	0.41014(5)	0.0275(7)
C10	0.8665(3)	0.3452(3)	0.42466(6)	0.0376(8)
C11	0.9169(3)	0.4651(3)	0.40868(7)	0.0410(9)
C12	0.8991(3)	0.4607(3)	0.37888(7)	0.0379(9)
C13	0.8325(3)	0.3366(3)	0.36552(6)	0.0290(7)
C14	0.6927(3)	-0.0129(3)	0.40636(5)	0.0252(7)
C15	1.0210(3)	-0.1282(3)	0.37080(6)	0.0314(8)
C16	1.1566(3)	-0.1845(3)	0.36090(7)	0.0407(9)
C17	1.1802(3)	-0.1749(3)	0.33162(7)	0.0428(10)
C18	1.0685(3)	-0.1115(3)	0.31300(6)	0.0373(8)
C19	0.9329(3)	-0.0600(3)	0.32412(5)	0.0277(7)

C20	0.8136(4)	0.0167(3)	0.27495(6)	0.0387(9)
C21	0.6483(4)	0.0124(3)	0.26194(6)	0.0449(10)
C22	0.5425(3)	0.1238(3)	0.27591(6)	0.0406(9)
C23	0.4427(3)	0.1428(3)	0.32594(5)	0.0294(7)
C24	0.3056(3)	0.2141(3)	0.31618(7)	0.0389(8)
C25	0.1960(3)	0.2467(3)	0.33594(7)	0.0444(10)
C26	0.2237(3)	0.2071(3)	0.36467(7)	0.0416(9)
C27	0.3619(3)	0.1384(3)	0.37319(6)	0.0327(8)
C28	0.6870(3)	0.0433(3)	0.32164(5)	0.0248(7)
P2	0.82685(9)	0.51235(8)	0.28192(2)	0.0373(2)
F21	0.8681(2)	0.5879(2)	0.31265(4)	0.0545(6)
*F22B	0.6490(6)	0.5138(13)	0.28589(14)	0.073(3)
*F23B	0.8215(17)	0.6699(8)	0.2672(2)	0.106(4)
*F24B	1.0119(6)	0.5081(17)	0.27956(12)	0.092(4)
*F25B	0.8410(14)	0.3532(6)	0.29779(12)	0.070(3)
F26	0.7817(3)	0.4347(2)	0.25134(4)	0.0653(8)
*F22A	0.6713(12)	0.6118(16)	0.28123(14)	0.080(3)
*F23A	0.9019(16)	0.6364(11)	0.2639(2)	0.098(4)
*F24A	0.9743(13)	0.4138(12)	0.28057(16)	0.086(3)
*F25A	0.7396(16)	0.3849(13)	0.29781(13)	0.085(4)
P1	0.16084(9)	0.80461(9)	0.45979(2)	0.0420(3)
F11	0.1276(4)	0.9503(4)	0.47701(6)	0.1136(14)
F12	0.2564(3)	0.8971(4)	0.43754(5)	0.0981(12)
F13	0.3158(2)	0.7785(3)	0.47985(4)	0.0631(7)
F14	0.0681(3)	0.7129(4)	0.48148(7)	0.1232(13)
F15	0.0058(2)	0.8299(3)	0.43967(4)	0.0615(7)
F16	0.2005(3)	0.6620(3)	0.44180(6)	0.1002(11)
N44	0.4303(5)	0.3127(4)	0.44031(9)	0.0930(16)
C43	0.2355(6)	0.3394(6)	0.47988(10)	0.096(2)
C44	0.3470(5)	0.3266(4)	0.45809(9)	0.0658(14)

Table XVII. Hydrogen atom positions and isotropic displacement parameters for **2**, $P2_1/c$, R = 0.03.

Atom	x	y	z	U(iso) [Ang^2]
H1	0.58480	-0.27070	0.32690	0.0370
H2	0.48490	-0.50610	0.33590	0.0480
H3	0.44930	-0.57830	0.38380	0.0510
H4	0.52040	-0.41530	0.42190	0.0430
H6A	0.73400	-0.22350	0.45520	0.0420
H6B	0.54790	-0.23770	0.45240	0.0420
H7A	0.63280	-0.04300	0.48550	0.0470
H7B	0.51850	0.01850	0.45950	0.0470
H8A	0.72340	0.18670	0.46460	0.0440
H8B	0.84950	0.05430	0.46430	0.0440
H10	0.87740	0.34670	0.44530	0.0450
H11	0.96340	0.54970	0.41820	0.0490
H12	0.93250	0.54250	0.36760	0.0450
H13	0.81990	0.33480	0.34490	0.0350
H15	1.00580	-0.13280	0.39100	0.0380
H16	1.23260	-0.22900	0.37390	0.0490
H17	1.27370	-0.21220	0.32440	0.0520
H18	1.08420	-0.10320	0.29290	0.0450
H20A	0.87480	-0.06580	0.26690	0.0460
H20B	0.86320	0.11290	0.27020	0.0460
H21A	0.60600	-0.08980	0.26420	0.0540
H21B	0.64880	0.03420	0.24090	0.0540
H22A	0.57220	0.22740	0.27100	0.0490
H22B	0.43310	0.10720	0.26880	0.0490
H24	0.28770	0.23980	0.29630	0.0470
H25	0.10210	0.29610	0.32980	0.0530
H26	0.14840	0.22710	0.37840	0.0500
H27	0.38040	0.11160	0.39300	0.0390
H43A	0.16270	0.42080	0.47470	0.1430

H43B	0.28970	0.36100	0.49870	0.1430
H43C	0.17800	0.24510	0.48110	0.1430

==========

The temperature factor has the form of Exp(-T), where
T = 8*(Pi**2)*U*(Sin(Theta)/Lambda)**2 for isotropic atoms.

Table XVIII. (An)isotropic displacement parameters for **2**, $P2_1/c$, R = 0.03.

Atom	U(1,1) or U	U(2,2)	U(3,3)	U(2,3)	U(1,3)	U(1,2)
Ru1	0.0206(1)	0.0197(1)	0.0222(1)	-0.0004(1)	0.0013(1)	-0.0010(1)
N1	0.0204(9)	0.0206(10)	0.0326(11)	0.0000(8)	0.0019(8)	0.0004(7)
N2	0.0278(10)	0.0270(10)	0.0268(10)	0.0033(8)	0.0051(8)	0.0001(8)
N3	0.0303(11)	0.0291(11)	0.0241(10)	-0.0032(8)	0.0018(8)	0.0000(8)
N4	0.0222(9)	0.0213(10)	0.0289(10)	-0.0018(8)	0.0004(8)	-0.0005(7)
N5	0.0238(10)	0.0225(10)	0.0293(10)	-0.0015(8)	0.0027(8)	-0.0014(8)
N6	0.0335(12)	0.0272(11)	0.0246(11)	-0.0007(8)	0.0038(9)	-0.0020(8)
N7	0.0325(11)	0.0283(11)	0.0280(10)	0.0021(8)	-0.0034(9)	-0.0019(8)
N8	0.0221(10)	0.0204(10)	0.0348(11)	-0.0022(8)	-0.0010(8)	-0.0018(7)
C1	0.0258(12)	0.0287(13)	0.0375(14)	-0.0059(10)	0.0000(10)	0.0019(10)
C2	0.0358(15)	0.0270(13)	0.0558(18)	-0.0104(12)	0.0000(13)	-0.0018(11)
C3	0.0369(15)	0.0225(13)	0.069(2)	0.0014(12)	0.0063(14)	-0.0049(11)
C4	0.0321(14)	0.0272(13)	0.0494(16)	0.0073(11)	0.0089(12)	0.0004(10)
C5	0.0207(11)	0.0251(12)	0.0380(14)	0.0019(10)	0.0042(10)	0.0020(9)
C6	0.0380(14)	0.0391(15)	0.0291(13)	0.0092(11)	0.0074(11)	0.0029(11)
C7	0.0449(17)	0.0468(17)	0.0262(13)	0.0039(11)	0.0089(12)	0.0036(12)
C8	0.0412(15)	0.0434(16)	0.0245(12)	-0.0041(11)	0.0027(11)	0.0006(12)
C9	0.0263(12)	0.0270(12)	0.0291(12)	-0.0020(10)	0.0012(10)	0.0017(9)
C10	0.0406(15)	0.0341(14)	0.0374(14)	-0.0093(11)	-0.0025(12)	-0.0046(11)
C11	0.0418(16)	0.0288(14)	0.0519(18)	-0.0117(12)	-0.0023(13)	-0.0074(12)
C12	0.0339(14)	0.0263(13)	0.0535(18)	0.0021(12)	0.0033(12)	-0.0047(11)
C13	0.0261(12)	0.0258(12)	0.0350(13)	0.0038(10)	0.0022(10)	-0.0005(9)

C14	0.0217(12)	0.0261(12)	0.0280(13)	0.0008(9)	0.0021(10)	0.0010(9)
C15	0.0274(13)	0.0271(13)	0.0392(14)	0.0007(10)	-0.0028(10)	-0.0002(10)
C16	0.0265(13)	0.0361(15)	0.0589(18)	-0.0013(13)	-0.0027(12)	0.0024(11
C17	0.0268(14)	0.0394(16)	0.063(2)	-0.0110(14)	0.0098(13)	0.0030(11)
C18	0.0342(14)	0.0354(14)	0.0436(15)	-0.0083(12)	0.0132(12)	-0.0047(11)
C19	0.0277(12)	0.0227(12)	0.0330(13)	-0.0026(10)	0.0046(10)	-0.0046(9)
C20	0.0521(18)	0.0398(15)	0.0252(13)	-0.0003(11)	0.0112(12)	-0.0023(12)
C21	0.062(2)	0.0474(18)	0.0244(14)	-0.0006(11)	-0.0036(13)	-0.0034(14)
C22	0.0483(17)	0.0440(16)	0.0282(13)	0.0058(11)	-0.0085(12)	-0.0022(13)
C23	0.0273(12)	0.0229(12)	0.0374(14)	0.0003(10)	-0.0032(10)	-0.0036(9)
C24	0.0348(14)	0.0307(14)	0.0496(16)	0.0056(12)	-0.0105(12)	-0.0014(11)
C25	0.0258(14)	0.0342(15)	0.072(2)	-0.0002(14)	-0.0062(13)	0.0037(11)
C26	0.0267(13)	0.0343(15)	0.064(2)	-0.0062(13)	0.0053(13)	0.0014(11)
C27	0.0269(13)	0.0279(13)	0.0436(15)	-0.0056(11)	0.0054(11)	-0.0026(10)
C28	0.0278(12)	0.0201(11)	0.0264(12)	-0.0002(9)	-0.0003(9)	-0.0044(9)
P2	0.0468(4)	0.0343(4)	0.0312(4)	0.0031(3)	0.0064(3)	0.0008(3)
F21	0.0657(12)	0.0492(11)	0.0476(10)	-0.0075(8)	-0.0053(9)	-0.0123(9)
F22B	0.039(2)	0.117(7)	0.063(3)	-0.041(4)	0.002(2)	0.005(3)
F23B	0.209(12)	0.035(3)	0.067(5)	0.018(3)	-0.046(6)	-0.015(5)
F24B	0.048(3)	0.178(10)	0.053(3)	-0.031(4)	0.021(2)	-0.020(4)
F25B	0.128(7)	0.036(2)	0.043(2)	0.0025(16)	-0.022(4)	0.002(3)
F26	0.1091(17)	0.0586(12)	0.0287(9)	-0.0060(8)	0.0074(10)	0.0047(12)
F22A	0.080(5)	0.117(8)	0.042(3)	-0.030(4)	-0.008(3)	0.051(6)
F23A	0.171(10)	0.050(5)	0.080(5)	0.007(4)	0.073(6)	-0.025(5)
F24A	0.075(6)	0.084(6)	0.095(5)	-0.017(4)	-0.022(4)	0.039(4)
F25A	0.136(9)	0.087(7)	0.031(2)	0.006(3)	-0.004(4)	-0.074(7)
P1	0.0389(4)	0.0525(5)	0.0349(4)	-0.0099(3)	0.0040(3)	-0.0010(3)
F11	0.135(3)	0.110(2)	0.0890(19)	-0.0586(17)	-0.0492(18)	0.0578(19)
F12	0.0697(15)	0.149(3)	0.0740(15)	0.0451(16)	-0.0093(12)	-0.0343(16)
F13	0.0498(11)	0.0962(16)	0.0432(10)	0.0010(8)	0.0010(8)	0.0073(10)
F14	0.0556(15)	0.192(3)	0.124(2)	0.080(2)	0.0219(15)	-0.0137(17)
F15	0.0420(10)	0.0963(16)	0.0459(10)	-0.0136(10)	-0.0005(8)	0.0045(10)

F16	0.0754(16)	0.101(2)	0.122(2)	-0.0667(17)	-0.0112(15)	0.0158(14)
N44	0.119(3)	0.064(2)	0.101(3)	0.024(2)	0.048(3)	0.021(2)
C43	0.104(4)	0.107(4)	0.079(3)	0.043(3)	0.035(3)	0.028(3)
C44	0.080(3)	0.055(2)	0.064(2)	0.0258(18)	0.017(2)	0.0152(19)

==========

The temperature factor has the form of Exp(-T), where
T = 8*(Pi**2)*U*(Sin(Theta)/Lambda)**2 for isotropic atoms.
T = 2*(Pi**2)*Sumij(h(i)*h(j)*U(i,j)*Astar(i)*Astar(j)), for anisotropic atoms.
Astar(i) are reciprocal axial lengths and h(i) are the reflection indices.

Table XIX. Bond distances (Å) for **2**, $P2_1/c$, R = 0.03.

Ru1	-N1	2.0841(18)	N3	-C8	1.474(3)
Ru1	-N4	2.0926(18)	N3	-C9	1.399(3)
Ru1	-N5	2.0913(17)	N4	-C9	1.364(3)
Ru1	-N8	2.0879(17)	N4	-C13	1.354(3)
Ru1	-C14	1.972(2)	N5	-C19	1.364(3)
Ru1	-C28	1.970(2)	N5	-C15	1.348(3)
P2	-F23B	1.562(8)	N6	-C28	1.351(4)
P2	-F24B	1.604(5)	N6	-C19	1.403(3)
P2	-F25B	1.600(5)	N6	-C20	1.474(4)
P2	-F26	1.600(2)	N7	-C28	1.350(3)
P2	-F22A	1.606(12)	N7	-C22	1.477(3)
P2	-F21	1.592(2)	N7	-C23	1.397(3)
P2	-F22B	1.553(5)	N8	-C27	1.352(3)
P2	-F25A	1.570(11)	N8	-C23	1.364(3)
P2	-F23A	1.549(11)	N44	-C44	1.129(6)
P2	-F24A	1.549(11)	C1	-C2	1.375(4)
P1	-F12	1.586(3)	C2	-C3	1.386(5)
P1	-F15	1.5966(19)	C3	-C4	1.374(4)

P1	-F13	1.5955(19)	C4	-C5	1.390(4)
P1	-F14	1.551(3)	C6	-C7	1.512(4)
P1	-F11	1.560(3)	C7	-C8	1.517(4)
P1	-F16	1.569(3)	C9	-C10	1.387(4)
N1	-C1	1.348(3)	C10	-C11	1.384(4)
N1	-C5	1.363(3)	C11	-C12	1.376(5)
N2	-C6	1.476(3)	C12	-C13	1.377(4)
N2	-C14	1.344(3)	C15	-C16	1.374(4)
N2	-C5	1.398(3)	C16	-C17	1.382(5)
N3	-C14	1.350(3)	C17	-C18	1.373(4)
C18	-C19	1.382(4)	C13	-H13	0.9500
C20	-C21	1.512(5)	C15	-H15	0.9500
C21	-C22	1.518(4)	C16	-H16	0.9500
C23	-C24	1.392(4)	C17	-H17	0.9500
C24	-C25	1.382(4)	C18	-H18	0.9500
C25	-C26	1.380(5)	C20	-H20A	0.9900
C26	-C27	1.375(4)	C20	-H20B	0.9900
C1	-H1	0.9500	C21	-H21A	0.9900
C2	-H2	0.9500	C21	-H21B	0.9900
C3	-H3	0.9500	C22	-H22B	0.9900
C4	-H4	0.9500	C22	-H22A	0.9900
C6	-H6A	0.9900	C24	-H24	0.9500
C6	-H6B	0.9900	C25	-H25	0.9500
C7	-H7B	0.9900	C26	-H26	0.9500
C7	-H7A	0.9900	C27	-H27	0.9500
C8	-H8A	0.9900	C43	-C44	1.436(6)
C8	-H8B	0.9900	C43	-H43A	0.9800
C10	-H10	0.9500	C43	-H43B	0.9800
C11	-H11	0.9500	C43	-H43C	0.9800
C12	-H12	0.9500			

Table XX. Bond Angles (°) for **2**, $P2_1/c$ R = 0.03.

N1	-Ru1	-N4	153.52(7)	F23B	-P2	-F25B	177.0(6)
N1	-Ru1	-N5	90.96(7)	F23B	-P2	-F26	90.4(3)
N1	-Ru1	-N8	93.83(7)	F24B	-P2	-F25B	87.8(7)
N1	-Ru1	-C14	76.98(9)	F24B	-P2	-F26	96.9(3)
N1	-Ru1	-C28	102.55(9)	F25B	-P2	-F26	91.6(2)
N4	-Ru1	-N5	93.91(7)	F22A	-P2	-F26	93.6(3)
N4	-Ru1	-N8	93.22(7)	F23A	-P2	-F26	85.6(4)
N4	-Ru1	-C14	76.60(9)	F24A	-P2	-F26	82.8(3)
N4	-Ru1	-C28	103.91(9)	F25A	-P2	-F26	90.0(3)
N5	-Ru1	-N8	153.71(7)	F22A	-P2	-F23A	88.2(6)
N5	-Ru1	-C14	104.33(9)	F22A	-P2	-F24A	176.4(4)
N5	-Ru1	-C28	76.83(9)	F22A	-P2	-F25A	89.3(6)
N8	-Ru1	-C14	101.93(9)	F23A	-P2	-F24A	90.9(6)
N8	-Ru1	-C28	76.90(9)	F23A	-P2	-F25A	174.8(5)
C14	-Ru1	-C28	178.73(11)	F24A	-P2	-F25A	91.3(6)
F21	-P2	-F23B	90.3(3)	F21	-P2	-F22B	93.5(3)
F21	-P2	-F24B	84.3(3)	F11	-P1	-F12	90.82(17)
F21	-P2	-F25B	87.8(2)	F11	-P1	-F14	89.65(18)
F21	-P2	-F26	178.61(12)	F11	-P1	-F15	90.36(15)
F21	-P2	-F22A	85.7(3)	F11	-P1	-F13	89.91(15)
F21	-P2	-F23A	95.6(4)	F12	-P1	-F13	90.22(12)
F21	-P2	-F24A	97.9(3)	F12	-P1	-F14	179.51(18)
F21	-P2	-F25A	88.7(3)	F12	-P1	-F15	89.86(12)
F22B	-P2	-F23B	92.3(7)	F12	-P1	-F16	86.65(16)
F22B	-P2	-F24B	177.0(3)	F13	-P1	-F14	89.60(13)
F22B	-P2	-F25B	90.1(6)	F13	-P1	-F15	179.72(14)
F22B	-P2	-F26	85.3(3)	F13	-P1	-F16	89.31(14)
F23B	-P2	-F24B	89.7(7)	F14	-P1	-F15	90.32(13)
F14	-P1	-F16	92.88(17)	C1	-C2	-C3	118.8(3)
F15	-P1	-F16	90.43(14)	C2	-C3	-C4	120.0(3)
F11	-P1	-F16	177.35(17)	C3	-C4	-C5	118.8(3)

Ru1	-N1	-C5	114.12(15)	N1	-C5	-N2	115.3(2)
C1	-N1	-C5	118.5(2)	N1	-C5	-C4	121.6(2)
Ru1	-N1	-C1	127.40(16)	N2	-C5	-C4	123.2(2)
C6	-N2	-C14	122.85(19)	N2	-C6	-C7	108.5(2)
C5	-N2	-C6	123.06(19)	C6	-C7	-C8	112.3(2)
C5	-N2	-C14	113.95(19)	N3	-C8	-C7	108.6(2)
C9	-N3	-C14	113.75(19)	N4	-C9	-C10	121.9(2)
C8	-N3	-C9	122.53(19)	N3	-C9	-N4	115.1(2)
C8	-N3	-C14	123.72(19)	N3	-C9	-C10	123.0(2)
C9	-N4	-C13	117.8(2)	C9	-C10	-C11	119.0(3)
Ru1	-N4	-C13	127.70(16)	C10	-C11	-C12	119.4(3)
Ru1	-N4	-C9	114.43(15)	C11	-C12	-C13	119.3(3)
Ru1	-N5	-C19	114.37(15)	N4	-C13	-C12	122.5(3)
C15	-N5	-C19	117.9(2)	Ru1	-C14	-N3	120.08(18)
Ru1	-N5	-C15	127.70(16)	Ru1	-C14	-N2	119.59(17)
C20	-N6	-C28	123.1(2)	N2	-C14	-N3	120.3(2)
C19	-N6	-C20	123.1(2)	N5	-C15	-C16	122.6(3)
C19	-N6	-C28	113.7(2)	C15	-C16	-C17	118.7(3)
C22	-N7	-C23	122.37(19)	C16	-C17	-C18	120.0(2)
C22	-N7	-C28	123.68(19)	C17	-C18	-C19	118.7(3)
C23	-N7	-C28	113.94(19)	N5	-C19	-C18	122.1(2)
Ru1	-N8	-C23	114.22(15)	N6	-C19	-C18	122.8(2)
Ru1	-N8	-C27	127.62(16)	N5	-C19	-N6	115.1(2)
C23	-N8	-C27	118.1(2)	N6	-C20	-C21	108.3(3)
N1	-C1	-C2	122.4(3)	C20	-C21	-C22	112.9(2)
N7	-C22	-C21	108.0(2)	H7A	-C7	-H7B	108.00
N7	-C23	-N8	115.1(2)	N3	-C8	-H8B	110.00
N8	-C23	-C24	121.7(2)	C7	-C8	-H8A	110.00
N7	-C23	-C24	123.3(2)	C7	-C8	-H8B	110.00
C23	-C24	-C25	118.8(3)	N3	-C8	-H8A	110.00
C24	-C25	-C26	119.7(3)	H8A	-C8	-H8B	108.00
C25	-C26	-C27	119.1(3)	C9	-C10	-H10	121.00

N8	-C27	-C26	122.6(3)	C11	-C10	-H10	120.00
Ru1	-C28	-N7	119.69(17)	C12	-C11	-H11	120.00
Ru1	-C28	-N6	119.98(18)	C10	-C11	-H11	120.00
N6	-C28	-N7	120.3(2)	C13	-C12	-H12	120.00
C2	-C1	-H1	119.00	C11	-C12	-H12	120.00
N1	-C1	-H1	119.00	N4	-C13	-H13	119.00
C1	-C2	-H2	121.00	C12	-C13	-H13	119.00
C3	-C2	-H2	121.00	C16	-C15	-H15	119.00
C2	-C3	-H3	120.00	N5	-C15	-H15	119.00
C4	-C3	-H3	120.00	C15	-C16	-H16	121.00
C3	-C4	-H4	121.00	C17	-C16	-H16	121.00
C5	-C4	-H4	121.00	C16	-C17	-H17	120.00
C7	-C6	-H6B	110.00	C18	-C17	-H17	120.00
N2	-C6	-H6A	110.00	C17	-C18	-H18	121.00
H6A	-C6	-H6B	108.00	C19	-C18	-H18	121.00
C7	-C6	-H6A	110.00	H20A	-C20	-H20B	108.00
N2	-C6	-H6B	110.00	N6	-C20	-H20A	110.00
C6	-C7	-H7B	109.00	C21	-C20	-H20B	110.00
C6	-C7	-H7A	109.00	C21	-C20	-H20A	110.00
C8	-C7	-H7A	109.00	N6	-C20	-H20B	110.00
C8	-C7	-H7B	109.00	C22	-C21	-H21A	109.00
C20	-C21	-H21B	109.00	C26	-C25	-H25	120.00
C20	-C21	-H21A	109.00	C27	-C26	-H26	120.00
H21A	-C21	-H21B	108.00	C25	-C26	-H26	120.00
C22	-C21	-H21B	109.00	C26	-C27	-H27	119.00
H22A	-C22	-H22B	109.00	N8	-C27	-H27	119.00
C21	-C22	-H22B	110.00	N44	-C44	-C43	177.1(5)
N7	-C22	-H22A	110.00	C44	-C43	-H43A	109.00
N7	-C22	-H22B	110.00	C44	-C43	-H43B	109.00
C21	-C22	-H22A	110.00	C44	-C43	-H43C	109.00
C25	-C24	-H24	121.00	H43A	-C43	-H43B	110.00
C23	-C24	-H24	121.00	H43A	-C43	-H43C	109.00

C24	-C25	-H25	120.00	H43B	-C43	-H43C	109.00

Table XXI. Crystal data and structure refinement for $\mathbf{1}_2$.

Identification code	viva11a
Empirical formula	C28 H28 N8
Formula weight	476.58
Temperature	100(2) K
Wavelength	1.54178 Å
Crystal system	Monoclinic
Space group	$P2_1/c$
Unit cell dimensions	Å
a, b, c [Å]	10.5459(4), 12.8430(5), 9.2601(3)
a, b, g [°]	90, 111.587(2), 90
Volume	1166.23(7) $Å^3$
Z	2
Density (calculated)	1.357 Mg/m^3
Absorption coefficient	0.672 mm^{-1}
F(000)	504
Crystal size	0.24 x 0.14 x 0.08 mm^3
Theta range for data collection	4.51 to 69.18°.
Index ranges	-12<=h<=12, -15<=k<=15, -11<=l<=11
Reflections collected	15347
Independent reflections	2147 [R(int) = 0.1078]
Completeness to theta = 69.18°	98.4 %

Absorption correction	Semi-empirical from equivalents
Max. and min. transmission	0.928718 and 0.653421
Refinement method	Full-matrix least-squares on F^2
Data / restraints / parameters	2147 / 0 / 163
Goodness-of-fit on F^2	1.021
Final R indices [I>2sigma(I)]	R1 = 0.0490, wR2 = 0.1276
R indices (all data)	R1 = 0.0613, wR2 = 0.1373
Largest diff. peak and hole	0.255 and -0.317 e.$Å^{-3}$

Table XXII. Atomic coordinates (x 10^4) and equivalent isotropic displacement parameters ($Å^2$x 10^3) for **1_2**. U(eq) is defined as one third of the trace of the orthogonalized U^{ij} tensor.

	x	y	z	U(eq)
N(1)	3283(1)	8995(1)	3413(2)	22(1)
N(2)	1439(1)	9109(1)	1113(2)	19(1)
N(3)	-703(1)	8701(1)	-825(2)	19(1)
N(4)	-2396(1)	9112(1)	133(2)	21(1)
C(1)	1226(2)	9773(1)	3475(2)	22(1)
C(2)	1843(2)	9928(1)	5057(2)	27(1)
C(3)	3192(2)	9611(1)	5820(2)	29(1)
C(4)	3848(2)	9145(1)	4960(2)	26(1)
C(5)	1983(2)	9313(1)	2688(2)	19(1)
C(6)	2209(2)	8459(1)	423(2)	22(1)
C(7)	1381(2)	8316(1)	-1293(2)	23(1)
C(8)	-62(2)	7960(1)	-1557(2)	25(1)
C(9)	-1978(2)	8505(1)	-779(2)	18(1)
C(10)	-2784(2)	7691(1)	-1677(2)	24(1)
C(11)	-4060(2)	7535(1)	-1631(2)	26(1)
C(12)	-4529(2)	8177(1)	-740(2)	25(1)
C(13)	-3660(2)	8946(1)	113(2)	23(1)
C(14)	160(2)	9491(1)	105(2)	17(1)

Table XXIII. Bond lengths [Å] and angles [°] for $\mathbf{1}_2$.

N(1)-C(4)	1.348(2)
N(1)-C(5)	1.349(2)
N(2)-C(5)	1.382(2)
N(2)-C(14)	1.416(2)
N(2)-C(6)	1.464(2)
N(3)-C(9)	1.383(2)
N(3)-C(14)	1.422(2)
N(3)-C(8)	1.469(2)
N(4)-C(9)	1.338(2)
N(4)-C(13)	1.344(2)
C(1)-C(2)	1.382(2)
C(1)-C(5)	1.395(2)
C(1)-H(1A)	0.9500
C(2)-C(3)	1.397(3)
C(2)-H(2A)	0.9500
C(3)-C(4)	1.369(3)
C(3)-H(3A)	0.9500
C(4)-H(4A)	0.9500
C(6)-C(7)	1.517(2)
C(6)-H(6A)	0.9900
C(6)-H(6B)	0.9900
C(7)-C(8)	1.520(2)
C(7)-H(7A)	0.9900
C(7)-H(7B)	0.9900

C(8)-H(8A)	0.9900
C(8)-H(8B)	0.9900
C(9)-C(10)	1.409(2)
C(10)-C(11)	1.376(2)
C(10)-H(10A)	0.9500
C(11)-C(12)	1.380(2)
C(11)-H(11A)	0.9500
C(12)-C(13)	1.381(2)
C(12)-H(12A)	0.9500
C(13)-H(13A)	0.9500
C(14)-C(14)#1	1.346(3)
C(4)-N(1)-C(5)	117.15(15)
C(5)-N(2)-C(14)	123.72(14)
C(5)-N(2)-C(6)	119.12(13)
C(14)-N(2)-C(6)	117.16(13)
C(9)-N(3)-C(14)	121.59(13)
C(9)-N(3)-C(8)	120.89(13)
C(14)-N(3)-C(8)	116.15(13)
C(9)-N(4)-C(13)	117.07(14)
C(2)-C(1)-C(5)	118.59(16)
C(2)-C(1)-H(1A)	120.7
C(5)-C(1)-H(1A)	120.7
C(1)-C(2)-C(3)	119.25(17)
C(1)-C(2)-H(2A)	120.4
C(3)-C(2)-H(2A)	120.4
C(4)-C(3)-C(2)	118.18(16)

C(4)-C(3)-H(3A)	120.9
C(2)-C(3)-H(3A)	120.9
N(1)-C(4)-C(3)	124.07(16)
N(1)-C(4)-H(4A)	118.0
C(3)-C(4)-H(4A)	118.0
N(1)-C(5)-N(2)	114.79(2)
N(1)-C(5)-C(1)	122.74(2)
N(2)-C(5)-C(1)	122.42(1)
N(2)-C(6)-C(7)	109.18(1)
N(2)-C(6)-H(6A)	109.8
C(7)-C(6)-H(6A)	109.8
N(2)-C(6)-H(6B)	109.8
C(7)-C(6)-H(6B)	109.8
H(6A)-C(6)-H(6B)	108.3
C(6)-C(7)-C(8)	111.17(6)
C(6)-C(7)-H(7A)	109.4
C(8)-C(7)-H(7A)	109.4
C(6)-C(7)-H(7B)	109.4
C(8)-C(7)-H(7B)	109.4
H(7A)-C(7)-H(7B)	108.0
N(3)-C(8)-C(7)	109.54(1)
N(3)-C(8)-H(8A)	109.8
C(7)-C(8)-H(8A)	109.8
N(3)-C(8)-H(8B)	109.8
C(7)-C(8)-H(8B)	109.8
H(8A)-C(8)-H(8B)	108.2

N(4)-C(9)-N(3)	117.57(1)
N(4)-C(9)-C(10)	122.49(2)
N(3)-C(9)-C(10)	119.94(2)
C(11)-C(10)-C(9)	118.32(2)
C(11)-C(10)-H(10A)	120.8
C(9)-C(10)-H(10A)	120.8
C(10)-C(11)-C(12)	120.05(2)
C(10)-C(11)-H(11A)	120.0
C(12)-C(11)-H(11A)	120.0
C(11)-C(12)-C(13)	117.48(2)
C(11)-C(12)-H(12A)	121.3
C(13)-C(12)-H(12A)	121.3
N(4)-C(13)-C(12)	124.53(2)
N(4)-C(13)-H(13A)	117.7
C(12)-C(13)-H(13A)	117.7
C(14)#1-C(14)-N(2)	124.00(2)
C(14)#1-C(14)-N(3)	122.32(2)
N(2)-C(14)-N(3)	113.21(1)

Symmetry transformations used to generate equivalent atoms: #1 -x, -y+2, -z.

Table XXIV. Anisotropic displacement parameters ($Å^2 \times 10^3$) for $\mathbf{1_2}$. The anisotropic displacement factor exponent takes the form: $-2p^2[h^2 a^*2U^{11} + ... + 2 h k a^* b^* U^{12}]$.

	U^{11}	U^{22}	U^{33}	U^{23}	U^{13}	U^{12}
N(1)	24(1)	13(1)	24(1)	2(1)	2(1)	1(1)
N(2)	20(1)	13(1)	18(1)	-1(1)	1(1)	4(1)
N(3)	22(1)	9(1)	23(1)	-5(1)	4(1)	-1(1)
N(4)	25(1)	14(1)	20(1)	1(1)	5(1)	1(1)
C(1)	26(1)	13(1)	24(1)	2(1)	4(1)	2(1)
C(2)	37(1)	19(1)	24(1)	-1(1)	10(1)	2(1)
C(3)	39(1)	21(1)	20(1)	-1(1)	0(1)	-1(1)
C(4)	28(1)	16(1)	25(1)	3(1)	-3(1)	-1(1)
C(5)	23(1)	8(1)	21(1)	1(1)	3(1)	-2(1)
C(6)	26(1)	14(1)	25(1)	1(1)	7(1)	6(1)
C(7)	27(1)	15(1)	24(1)	-3(1)	8(1)	4(1)
C(8)	30(1)	13(1)	29(1)	-5(1)	8(1)	1(1)
C(9)	22(1)	9(1)	18(1)	1(1)	1(1)	1(1)
C(10)	28(1)	15(1)	24(1)	-6(1)	5(1)	-1(1)
C(11)	28(1)	19(1)	25(1)	-2(1)	1(1)	-5(1)
C(12)	23(1)	23(1)	26(1)	4(1)	5(1)	-1(1)
C(13)	28(1)	19(1)	21(1)	1(1)	7(1)	3(1)
C(14)	20(1)	11(1)	17(1)	-1(1)	3(1)	0(1)

C Tables for Diamagnetic Contribution

Table XXV. Background correction values for the diamagnetic susceptibility in 10^{-6} emu/mol [72].

Metallionen	
V^{3+}	-10
Cr^{3+}	-11
Mn^{2+}	-14
Fe^{2+}	-13
Fe^{3+}	-10
Co^{2+}	-12
Co^{3+}	-10
Ni^{2+}	-10
Cu^{2+}	-11
Zn^{2+}	-15

Anionen	
O^{2-}	-12
S^{2-}	-30
F^-	-9,1
Cl^-	-23,4
Br^-	-34,6
I^-	-50,6
OH^-	-12
CN^-	-13
NCS^-	-31
ClO_4^-	-32
CH_3CO	-30

Atome	
H	-2,9
C	-6,0
N (ring)	-4,6
N (chain)	-5,6
N (imid, -CONH)	-2,1
O (ether, etc.)	-4,6
O (carbonyl)	-1,7
P	-26,3
S	-15,0
F	-6,3
Cl	-20,1
Br	-30,6
I	-44,6

Liganden	
H_2O	-13
NH_3	-18
CO	-10
NO	-6,5
CH_3OH	-23,1
en	-46
cp	-65
acac	-52
py	-49
bipy	-105
phen	-128
benzene	-55,1
toluene	-65,6
phenole	-59,3

D Checkcif reports

Table XXVI. Checkcif file designation for crystal structures $\mathbf{1}_2$, **2**, $[\mathbf{1H^+}][\mathbf{PF_6}]$.

Checkcif file designation	Compound
viva11a	$\mathbf{1}_2$
vivan5	**2**
vivan6	$[\mathbf{1H^+}][\mathbf{PF_6}]$

checkCIF/PLATON report

No syntax errors found. CIF dictionary Interpreting this report

Datablock: viva11a

Bond precision: C-C = 0.0025 A Wavelength=1.54178

Cell: a=10.5459(4) b=12.8430(5) c=9.2601(3)
alpha=90 beta=111.587(2) gamma=90
Temperature: 100 K

	Calculated	Reported
Volume	1166.23(8)	1166.23(7)
Space group	P 21/c	P21/c
Hall group	-P 2ybc	-P 2ybc
Moiety formula	C28 H28 N8	C28 H28 N8
Sum formula	C28 H28 N8	C28 H28 N8
Mr	476.58	476.58
Dx,g cm-3	1.357	1.357
Z	2	2
Mu (mm-1)	0.672	0.672
F000	504.0	504.0
F000'	505.38	
h,k,lmax	12,15,11	12,15,11
Nref	2183	2147
Tmin,Tmax	0.893,0.948	0.653,0.929
Tmin'	0.851	

Correction method= AbsCorr=MULTI-SCAN

Data completeness= Ratio = 0.984 Theta(max)= 69.180

R(reflections)= 0.0490(1685) wR2(reflections)= 0.1373(2147)

S = 1.021 Npar= 163

The following ALERTS were generated. Each ALERT has the format
test-name_ALERT_alert-type_alert-level.
Click on the hyperlinks for more details of the test.

Alert level C

ABSTM02_ALERT_3_C The ratio of expected to reported Tmax/Tmin(RR') is < 0.90
Tmin and Tmax reported: 0.653 0.929
Tmin(prime) and Tmax expected: 0.838 0.948
RR(prime) = 0.795
Please check that your absorption correction is appropriate.
RINTA01_ALERT_3_C The value of Rint is greater than 0.10

```
          Rint given   0.108
PLAT020_ALERT_3_C The value of Rint is greater than 0.10 .....      0.11
PLAT061_ALERT_3_C Tmax/Tmin Range Test RR' too Large ..........      0.78
PLAT062_ALERT_4_C Rescale T(min) & T(max) by ..................      1.02
PLAT152_ALERT_1_C Supplied and Calc Volume s.u. Inconsistent ....        ?
PLAT250_ALERT_2_C Large U3/U1 Ratio for Average U(i,j) Tensor ....      2.27
```

```
   0 ALERT level A = In general: serious problem
   0 ALERT level B = Potentially serious problem
   7 ALERT level C = Check and explain
   0 ALERT level G = General alerts; check

   1 ALERT type 1 CIF construction/syntax error, inconsistent or missing data
   1 ALERT type 2 Indicator that the structure model may be wrong or deficient
   4 ALERT type 3 Indicator that the structure quality may be low
   1 ALERT type 4 Improvement, methodology, query or suggestion
   0 ALERT type 5 Informative message, check
```

Publication of your CIF in IUCr journals

A basic structural check has been run on your CIF. These basic checks will be run on all CIFs submitted for publication in IUCr journals (*Acta Crystallographica, Journal of Applied Crystallography, Journal of Synchrotron Radiation*); however, if you intend to submit to *Acta Crystallographica Section C* or *E*, you should make sure that full publication checks are run on the final version of your CIF prior to submission.

Publication of your CIF in other journals

Please refer to the *Notes for Authors* of the relevant journal for any special instructions relating to CIF submission.

PLATON version of 27/11/2007; check.def file version of 27/11/2007

Datablock viva11a - ellipsoid plot

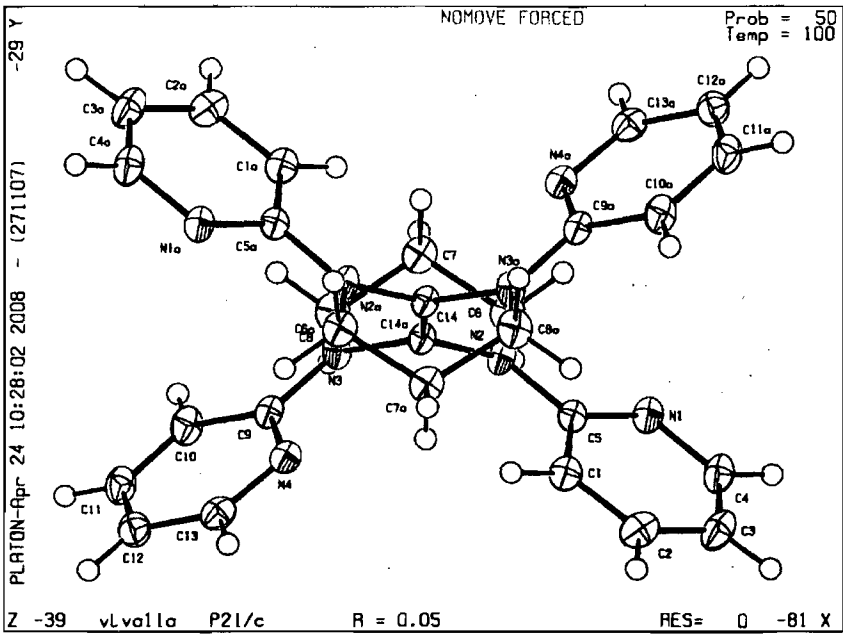

checkCIF/PLATON report

No syntax errors found. CIF dictionary Interpreting this report

Datablock: vivan5

Bond precision: C-C = 0.0043 A Wavelength=1.54178

Cell: a=8.6113(1) b=8.9270(1) c=46.1772(7)
alpha=90 beta=93.415(1) gamma=90
Temperature: 150 K

	Calculated	Reported
Volume	3543.48(8)	3543.48(8)
Space group	P 21/c	P21/c
Hall group	-P 2ybc	-P 2ybc
Moiety formula	C28 H28 N8 Ru, 2(F6 P), C2 H3 N	C28 H28 N8 Ru, 2(F6 P), C2 H3 N
Sum formula	C30 H31 F12 N9 P2 Ru	C30 H31 F12 N9 P2 Ru
Mr	908.65	908.65
Dx,g cm-3	1.703	1.703
Z	4	4
Mu (mm-1)	5.363	5.363
F000	1824.0	1824.0
F000'	1833.13	
h,k,lmax	10,10,55	10,10,55
Nref	6578	6530
Tmin,Tmax	0.411,0.651	0.530,0.740
Tmin'	0.267	

Correction method= AbsCorr=MULTI-SCAN

Data completeness= Ratio = 0.993 Theta(max)= 69.040

R(reflections)= 0.0300(5958) wR2(reflections)= 0.0835(6530)

S = 1.062 Npar= 525

The following ALERTS were generated. Each ALERT has the format
test-name_ALERT_alert-type_alert-level.
Click on the hyperlinks for more details of the test.

Alert level C

ABSTM02_ALERT_3_C The ratio of expected to reported Tmax/Tmin(RR) is > 1.10
Tmin and Tmax reported: 0.530 0.740
Tmin and Tmax expected: 0.401 0.651
RR = 1.162
Please check that your absorption correction is appropriate.

```
PLAT060_ALERT_3_C Ratio Tmax/Tmin (Exp-to-Rep) (too) Large .....      1.14
PLAT062_ALERT_4_C Rescale T(min) & T(max) by .....                    0.88
PLAT180_ALERT_3_C Check Cell Rounding: # of Values Ending with 0 =       3
PLAT231_ALERT_4_C Hirshfeld Test (Solvent)   F22B   -   F25A    ..     5.31 su
PLAT231_ALERT_4_C Hirshfeld Test (Solvent)   F23B   -   F22A    ..     7.98 su
PLAT231_ALERT_4_C Hirshfeld Test (Solvent)   F23B   -   F23A    ..     8.17 su
PLAT231_ALERT_4_C Hirshfeld Test (Solvent)   F25B   -   F25A    ..     7.84 su
PLAT244_ALERT_4_C Low   'Solvent' Ueq as Compared to Neighbors for       P2
PLAT244_ALERT_4_C Low   'Solvent' Ueq as Compared to Neighbors for       P1
PLAT244_ALERT_4_C Low   'Solvent' Ueq as Compared to Neighbors for      C44
PLAT250_ALERT_2_C Large U3/U1 Ratio for Average U(i,j) Tensor ....     2.05
PLAT302_ALERT_4_C Anion/Solvent Disorder .....                       19.00 Perc.
PLAT779_ALERT_2_C Suspect or Irrelevant (Bond) Angle in CIF .....    28.90 Deg.
             F23A -P2   -F23B    1.555   1.555   1.555
PLAT779_ALERT_2_C Suspect or Irrelevant (Bond) Angle in CIF .....    33.60 Deg.
             F25A -P2   -F25B    1.555   1.555   1.555
PLAT779_ALERT_2_C Suspect or Irrelevant (Bond) Angle in CIF .....    33.30 Deg.
             F24A -P2   -F24B    1.555   1.555   1.555
PLAT779_ALERT_2_C Suspect or Irrelevant (Bond) Angle in CIF .....    34.00 Deg.
             F22B -P2   -F22A    1.555   1.555   1.555
```

Alert level G

```
ABSTM02_ALERT_3_G  When printed, the submitted absorption T values will be
           replaced by the scaled T values. Since the ratio of scaled T's
           is identical to the ratio of reported T values, the scaling
           does not imply a change to the absorption corrections used in
           the study.
           Ratio of Tmax expected/reported      0.880
           Tmax scaled      0.651 Tmin scaled      0.466
```

```
  0 ALERT level A = In general: serious problem
  0 ALERT level B = Potentially serious problem
 17 ALERT level C = Check and explain
  1 ALERT level G = General alerts; check

  0 ALERT type 1 CIF construction/syntax error, inconsistent or missing data
  5 ALERT type 2 Indicator that the structure model may be wrong or deficient
  4 ALERT type 3 Indicator that the structure quality may be low
  9 ALERT type 4 Improvement, methodology, query or suggestion
  0 ALERT type 5 Informative message, check
```

Publication of your CIF in IUCr journals

A basic structural check has been run on your CIF. These basic checks will be run on all CIFs submitted for publication in IUCr journals (*Acta Crystallographica*, *Journal of Applied Crystallography*, *Journal of Synchrotron Radiation*); however, if you intend to submit to *Acta Crystallographica Section C* or *E*, you should make sure that full publication checks are run on the final version of your CIF prior to submission.

Publication of your CIF in other journals

Please refer to the *Notes for Authors* of the relevant journal for any special instructions relating to CIF submission.

PLATON version of 27/11/2007; check.def file version of 27/11/2007

Datablock vivan5 - ellipsoid plot

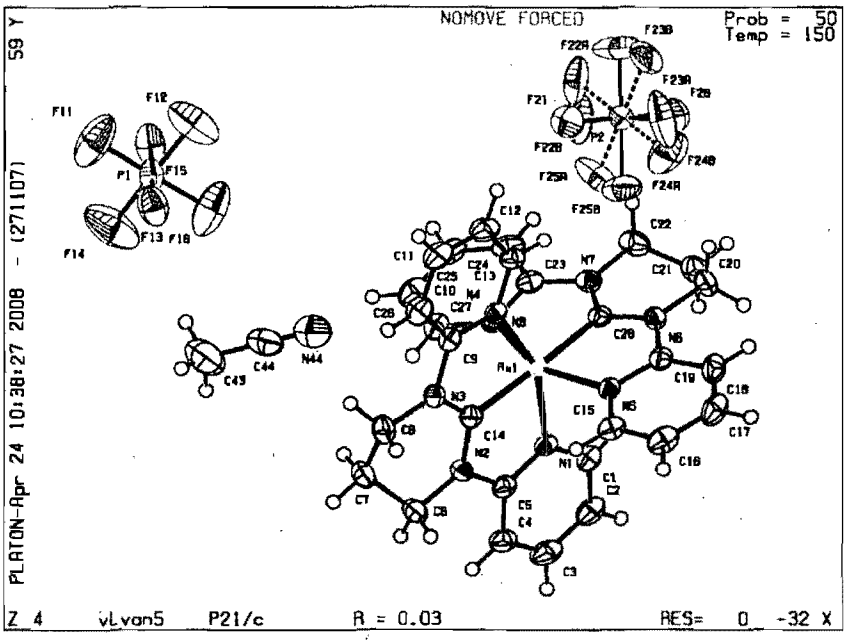

checkCIF/PLATON report

No syntax errors found. CIF dictionary Interpreting this report

Datablock: vivan6

Bond precision: C-C = 0.0020 A Wavelength=1.54178

Cell: a=8.8907(1) b=11.4813(1) c=15.5497(2)
alpha=90 beta=103.465(1) gamma=90
Temperature: 150 K

	Calculated	Reported
Volume	1543.63(3)	1543.63(3)
Space group	P 21/c	P21/c
Hall group	-P 2ybc	-P 2ybc
Moiety formula	C14 H15 N4, F6 P	C14 H15 N4, F6 P
Sum formula	C14 H15 F6 N4 P	C14 H15 F6 N4 P
Mr	384.27	384.27
Dx,g cm-3	1.653	1.653
Z	4	4
Mu (mm-1)	2.288	2.288
F000	784.0	784.0
F000'	788.29	
h,k,lmax	10,13,18	10,13,18
Nref	2873	2847
Tmin,Tmax	0.696,0.709	0.710,0.780
Tmin'	0.603	

Correction method= AbsCorr=MULTI-SCAN

Data completeness= Ratio = 0.991 Theta(max)= 68.980

R(reflections)= 0.0307(2752) wR2(reflections)= 0.0802(2847)

S = 1.036 Npar= 227

The following ALERTS were generated. Each ALERT has the format
test-name_ALERT_alert-type_alert-level.
Click on the hyperlinks for more details of the test.

Alert level B

PLAT432_ALERT_2_B Short Inter X...Y Contact F11 .. C14 .. 2.86 Ang.

Alert level C

PLAT062_ALERT_4_C Rescale T(min) & T(max) by 0.91
PLAT142_ALERT_4_C su on b - Axis Small or Missing (x 100000) ..... 10 Ang.

```
PLAT180_ALERT_3_C Check Cell Rounding: # of Values Ending with 0 =          3
PLAT244_ALERT_4_C Low   'Solvent' Ueq as Compared to Neighbors for         P1
PLAT431_ALERT_2_C Short Inter HL..A Contact  F12     ..  N3       ..      3.00 Ang.
```

Alert level G

```
ABSTM02_ALERT_3_G  When printed, the submitted absorption T values will be
           replaced by the scaled T values. Since the ratio of scaled T's
           is identical to the ratio of reported T values, the scaling
           does not imply a change to the absorption corrections used in
           the study.
           Ratio of Tmax expected/reported      0.910
           Tmax scaled      0.709 Tmin scaled      0.646
```

```
  0 ALERT level A = In general: serious problem
  1 ALERT level B = Potentially serious problem
  5 ALERT level C = Check and explain
  1 ALERT level G = General alerts; check

  0 ALERT type 1 CIF construction/syntax error, inconsistent or missing data
  2 ALERT type 2 Indicator that the structure model may be wrong or deficient
  2 ALERT type 3 Indicator that the structure quality may be low
  3 ALERT type 4 Improvement, methodology, query or suggestion
  0 ALERT type 5 Informative message, check
```

Publication of your CIF in IUCr journals

A basic structural check has been run on your CIF. These basic checks will be run on all CIFs submitted for publication in IUCr journals (*Acta Crystallographica, Journal of Applied Crystallography, Journal of Synchrotron Radiation*); however, if you intend to submit to *Acta Crystallographica Section C* or *E*, you should make sure that full publication checks are run on the final version of your CIF prior to submission.

Publication of your CIF in other journals

Please refer to the *Notes for Authors* of the relevant journal for any special instructions relating to CIF submission.

PLATON version of 27/11/2007; check.def file version of 27/11/2007

Datablock vivan6 - ellipsoid plot